Mechanical Characterizations of Sub-Micron Scale Materials Using MEMS Technology

Oh, Hyun-Jin

Doctoral Dissertation

Mechanical Characterizations of Sub-Micron Scale Materials Using MEMS Technology

(MEMS技術を用いたサブミクロンスケール材料の
力学特性評価に関する研究)

January 2015

Department of Mechanical Engineering,

Graduate School of Engineering, Kobe University

Hyun-Jin OH

ABSTRACT

Mechanical properties of materials used in micro-electronic devices and Micro-Electro-Mechanical Systems (MEMS) should be evaluated for a practical usage because most properties are generally known as depending on the size and the fabrication processes as they define microscopic structures. Several evaluation techniques have so far been proposed to measure mechanical properties of micro-scale materials, such as an acoustic test, nano-indentation test, bending test, tensile test, and so on. Most of test techniques are available to mechanical characterization for micron size materials, whereas there are some difficulties associated with detecting very small material responses for submicron size materials. However, tensile test is excellently superior in accurate measurement of stress-strain relationship of submicron size specimen, if the elongation at the gauge section of a specimen can be measured accurately during the test.

This thesis focuses on the establishment of experimental techniques for mechanical characterization from submicron to several nanometer scale materials based on tensile test method using MEMS technology and the evaluation of their mechanical properties. The background and objective of this research are described at full length in **chapter 1**.

In **chapter 2**, mechanical properties of silicon nitride compounds (SiNx) films, prepared by the plasma-enhanced chemical vapor deposition (PE-CVD) method, were evaluated by the tensile testing technique built into the commercial AFM. The meaning of x in the SiNx is variable values by ratio of silicon to nitride. SiNx films are typically employed as an etching stop layer both for wet and dry etching of silicon in MEMS process due to their chemical inertness. SiNx films also possess excellent characteristics in an electrical isolation and a strong resistance to oxidation, so that they are suitable for a passivation coating materials in micro-electronic devices and MEMS. The deposition condition determine the chemical composition of films that induce wide variations in material characteristics. This chapter investigated the gas flow ratio effects in the preparation of submicron thick SiNx films on their elastic properties. The SiNx films with a thickness ranging from 0.15 to 0.70 μm, which are the design dimensions, were deposited by PE-CVD onto the 10 μm thick single crystal silicon (SCS) specimens by changing the gas flow ratio of NH$_3$ (ammonia) to SiH$_4$ (mono-silane). Young's modulus of the SiNx films

ranged from 102 to 143 **GPa**, which increased with an increase of the gas flow ratio, but was independent of the film thickness. Nano-indentation tests were also carried out to examine Poisson's ratio of SiNx films in addition to the tensile tests. The ratio was found to be 0.20 to 0.26 in average. To analyze the molecular intensity of film surface of SiNx, Auger spectroscopy was conducted. The analyzed data revealed that an increase of the atomic content ratio of N (nitrogen) to Si (silicon) in SiNx films yielded to higher elastic properties of the films and reached to the their values of polycrystalline silicon nitride.

In **chapter 3**, the MEMS-based electrostatically actuated nano-tensile testing device, which is named EANAT, has been developed in our laboratory and it has been applied to the Au thin films with thickness in the sub-100-**nm** regime, which is, for example, used for nano-transfer-printing (**n**-TP) process. For predicting accurate dimensions in the printed pattern of **n**-TP in finite element analyses (FEA), the strain rate dependency on mechanical properties of Au films should be evaluated. Because the pattern dimensions could be changed during the fabricating procedure of Au film. The sub-100-**nm**-thick Au film was prepared in the course of fabrication of the MEMS-based tensile testing device. This device fabrication realized the precise loading direction without preloading before tensile tests. The loads were applied electrostatically by the electrostatically driving actuators. The obtained Young's moduli were 29±3 **GPa** and was insensitive to the strain rate. The 0.2 % yield strength were in the range from 192 to 519 **MPa** with a trend of decrease with decreasing strain rate in the range from 5×10^{-5} s^{-1} to 5×10^{-2} s^{-1}. These results have suggested that the loading condition to the substrate of n-TP process will affect printed pattern dimensions of Au film.

In **chapter 4**, EANAT, and an *in-situ* scanning electron microscopy (SEM) nanomaterial manipulation system were developed to investigate the mechanical characteristics of multi-walled carbon nanotubes (MWCNTs) synthesized by atmospheric pressure-CVD (APCVD). MWCNTs are one of promising ultra-low-resistance interconnect materials for via structures in micro-electronic devices. The EANAT can measure uniaxial tensile displacement of nanomaterial using a capacitive displacement sensor. The resolution of the measurement displacement was 0.28 **nm** at the minimum. The nanomaterial manipulation system allows for an individual MWCNT to be picked up from a substrate and to be attached to an EANAT. The stress-strain relationships for the individual MWCNT were successfully obtained from the nano-tensile tests, and Young's moduli were estimated to be in the range from 338 to 623 **GPa**. The deformation

of individual MWCNT under uniaxial loading was accompanied by repeated stick-slip and hard sticking events like telescopic motion. On the basis of the single-shot extraction model, the shear strength was estimated to be an average of 78 $\mathbf{MPa}$ greater than that for high quality crystalline graphite, which might be caused by the hard sticking between carbon nanotube layers.

This research demonstrated MEMS was effective technology for accurate mechanical characterization for sub-micron scale materials used in micro-electric devices and MEMS. Especially, MEMS-based tensile testing device can measure ultra-small load and displacement in the respective resolutions of $\mathbf{nN}$ and $\mathbf{pm}$ for individually standing nano-materials.

CONTENTS

List of Abbreviations

Nomenclature

Greek Symbols

1. Introduction

2. Influence of Gas Flow Ratio in PE-CVD Process on Mechanical Properties of Silicon Nitride Film

3. Strain Rate Dependence of Mechanical Properties for Sub 100 nm-Thick Au Film Using EANAT

4. Characterization of Interlayer Sliding Deformation for Individual Multi-Walled Carbon Nanotubes Using Electrostatically Actuated Nano Tensile Testing Device

5. Conclusions

Acknowledgements

List of Abbreviation

3-D	**3-D**imensional space
μ-TAS	**Micro T**otal **A**nalysis **S**ystem
AFM	**A**tomic **F**orce **M**icroscope
AM-OLED	**A**ctive-**M**atrix **O**rganic **L**ight-**E**mitting **D**iode
ASTM	**A**merican **S**ociety for **T**esting and **M**aterials
Au	Gold
BOX	**B**uried **OX**ide
CdS	**Ca**dmium **S**ulphide
CdTe	**Ca**dmium **Te**lluride
CIGS	**C**opper **I**ndium **G**allium **S**elenide
CNT	**C**arbon **N**ano**T**ube
DLC	**D**iamond **L**ike **C**arbon
EANAT	**E**lectrostatically **A**ctuated **N**anotensile **T**esting devices
fF	**f**emto **F**arad (10^{-15} Farad)
FE-SEM	**F**ield **E**mission **S**canning **E**lectron **M**icroscopy
FEA	**F**inite **E**lement **A**nalysis
GPa	**G**iga **Pa**scal (10^9 Pa)
H	**H**ydrogen
HF	**H**ydro **F**luoric
IC	**I**ntegrated **C**ircuit
KOH	Potassium hydroxide
LIGA	**LI**thographie, **G**alvanoformung, **A**bformung (German)
	Lithography, Electroplating, and Molding (English)
LP-CVD	**L**ow **P**ressure **C**hemical **V**apor **D**eposition
LVDT	**L**inear **V**ariable **D**isplacement **T**ransducer

MEMS	**M**icro **E**lectro **M**echanical **S**ystems
mm	**m**illi**m**eter (10^{-3} m)
MOEMS	**M**icro **O**pto **E**lectro **M**echanical **S**ystem
MPa	**M**ega **Pa**scal (10^6 Pa)
MST	**M**icro **S**ystem **T**echnology
MWCNT	**M**ulti-**W**alled **C**arbon **N**ano**T**ube
n-TP	**n**ano- **T**ransfer **P**rinting
N	**N**itrogen
NEMS	**N**ano **E**lectro **M**echanical **S**ystems
NH₃	Ammonia gas
N₂	Nitrogen gas
nN	**n**ano **N**ewton (10^{-9} N)
O	**O**xygen
PCB	**P**rinted **C**ircuit **B**oard
PE-CVD	**P**lasma **E**nhanced **C**hemical **V**apor **D**eposition
pm	**p**ico **m**eter (10^{-12} m)
PMMA	**P**oly **M**ethyl **M**eth**a**crylate
PZT	Lead(**P**b) **Z**irconate **T**itanate
RIE	**R**eactive **I**on **E**tching
s⁻¹	$1/s$
SCS	**S**ingle **C**rystal **S**ilicon
SEM	**S**canning **E**lectron **M**icroscopy
Si	**Si**licon
SiH₄	Mono-silane gas
SiN𝑥	**Si**licon **N**itride (x means the existence of various phases)
SiO₂	**Si**licon **dio**xide
SOI	**S**ilicon **O**n **I**nsulator
SWCNT	**S**ingle-**W**alled **C**arbon **N**ano**T**ube

TMAH   **T**etra **M**ethyl **A**mmonium **H**ydroxide

via   **v**ertical **i**nterconnect **a**ccess

ZnO   **Zi**nc **O**xide

Nomenclature

Chapter 1

E Young's modulus

σ_Y yield strength

σ_F fracture strength

Chapter 2

E_{1+2} effective elastic modulus of SiNx/SCS laminated specimens

t_1 thickness of SCS substrate

t_2 thickness of SiNx film

E_1 Young's modulus of SCS substrate

E_2 Young's modulus of SiNx film

S unloading stiffness

C_f compliance of the load frame in the nano-indentation tester

E_r reduced Young's modulus

A contact area between the film and the indenter

v_2 Poisson's ratio of the SiNx film

v_i Poisson's ratio of a diamond indenter used in the test

E_i Young's modulus of a diamond indenter used in the test

E_{1+2}^{LVDT} effective elastic modulus of SiNx/SCS laminated specimens by LVDT

E_{1+2}^{AFM} effective elastic modulus of SiNx/SCS laminated specimens by AFM

Chapter 3

d_s displacement between the specimen part and the actuator part (4 μm)

d_m displacement between the measurement part and the actuator part (3 μm)

Chapter 4

g_1 displacement between the measurement part and the actuator part (3 μm)

g_2 displacement between the specimen part and the actuator part (4 μm)

F force by the comb actuator

K_a total stiffness of the supporting beams of the comb actuator

K_{ds} total stiffness of the sensor structures

K_s total stiffness of the supporting beams of the specimen area

K_{cnt} stiffness of the specimen area

δ_a^{before} displacement before the failure of the sample

P tensile force of the specimen

δ_a^{after} displacement before the failure of the sample

a upper width of trapezoidal cross-section area of the comb

b lower width of trapezoidal cross-section area of the comb

h height of trapezoidal cross-section area of the comb

E Young's modulus

δ_a actuator displacement

F_a force by the comb actuator at the displacement of δ_a

N number of combs

ε_0 dielectric constant in a vacuum

w width of the comb

d_1 gap distance between contiguous comb

d_2 distance from the tip of the comb to the opposite comb electrode

V_a voltage applied to the actuator

Chapter 1

Introduction

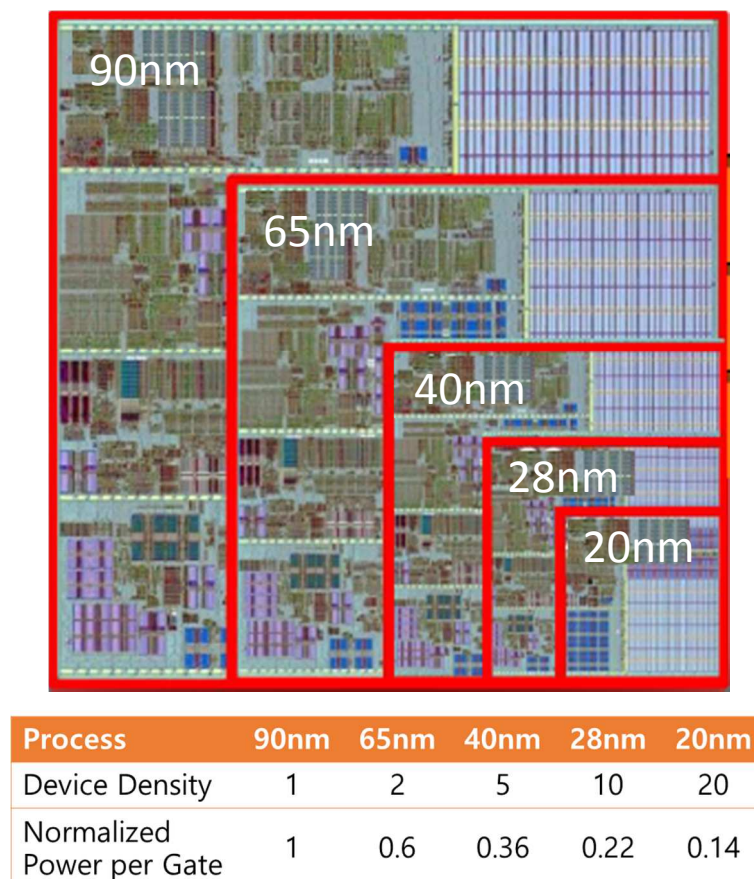### 1.1 Motivation: Why should we evaluate the mechanical properties of micro- and nano- scale materials?

After the invention of electricity in the 19th century, the electronic devices started to make a rapid progress. Especially over the past several decades from now on, electronic devices used semiconductor components have been making accelerated progress in order to realize the high performance, miniaturization, multi-function, and even cost reduction. For example, a representative personal portable electronic devices like laptop computer and smart phone (included mobile phone) have been fast evolved for only 20 years. For example, in the summer of 1995, it was a significant turning point in the history of personal laptop computer. Microsoft^{TM} Software Company released Windows 95^{TM} that is user friendly operation system. It made a great leap forward possibility in the technology. At that time, anyone could carry out the laptop computer wherever he/she wanted to go, and they could do the business work using programs like Word^{TM}, Excel^{TM}, and PowerPoint^{TM}. Comparing the averaging laptop computer selling nowadays, the weight has been reduced more the 3 times from 3.6 kg to under 1.0 kg, however the speed of CPU has been increased more than 100 times from 16 MHz to 1.6 GHz, and even the computational memory more than 4,000 times from 2 MB to 8 GB. Furthermore, it began to touch screen to control the computer and, due to development between the interfaces, USB version 3.0 is now 3,000 times faster than the USB version 1.0. Then various sensors are equipped in the devices to provide convenience to the users. It has been taken only 20 years, from 1994 to 2014, for these remarkable changes, and it was a major innovation in terms of technical progress.

To achieve a technical progress of recent trend, it is required to put as much as electronic components like capacitors, inductors, resistors, diodes, and transistors in the same sized product, also newly developed functions such as accelerometer, gyroscope, pressure sensor, microphone, and others would be combined in the limited space inside the device. It means that the components need to decrease the size of all dimensions, development of new materials (alloys),

and additionally to evaluate the mechanical properties at the actual size. For example, GLOB-ALFOUNDRIES Inc. suggested the relationship of device density and normalized power per gate that depends on the process. When the line width is decreased from 90 **nm** to 20 **nm**, the gross area of device is only 5 % than before, and normalized power per gate, which means consuming power, also dramatically down by 86 percent as shown in **Fig. 1.1 [1]**.

Fuji Chimera Research Institute, Inc. in Japan proposed several kinds of promising products/systems among the recent electronic component industry [2]. These products/systems are CdS/CdTe [3-4], crystallization solar battery cell [5-11] (single- and poly- crystal type), raw materials for lithium-ion battery [12-14], smart meter [15, 16], aluminum electrolytic capacitor [17, 18], AM-OLED [19], Thin-film Projected Capacitive Touch Panel [20]. To describe each item mentioned above in detail: **solar cell** or so called a photovoltaic cell is an electrical device that converts the energy of light into electricity directly by photovoltaic effect. Many researchers

Process	90nm	65nm	40nm	28nm	20nm
Device Density	1	2	5	10	20
Normalized Power per Gate	1	0.6	0.36	0.22	0.14

Fig. 1.1   The relationship of device density and normalized power per gate that depends on the process.

have been pouring more effort into their work to develop the high performance battery cell than ever, just as *Thomas Edison* had done many trials and errors to invent and sell the first commercially light bulb [21]. There are many researchers that suggest way to improve the solar cell performance [22-26]. Also, **lithium-ion battery** is a series of rechargeable batteries, but that is one of the most promising battery because of the no memory effect, only a few loss of accumulated charge when not in use. Hersam *et al.* informed ongoing efforts to utilize SWCNTs as conductive additives in nano-composite lithium ion battery electrodes [27]. **Smart meter**, which sounds unfamiliar to hear, is an electronic device that reports the consumption of electric energy in intervals of certain time or real time and communicates the information to the utility for monitoring and billing purposes [28-33]. Of all smart meter technologies, one of the critical technological issues is an insufficient communication system. To solve this problem, the sending and receiving data should be compressed heavily and decompressed as soon as possible. Of course, sending time also should be reduced rapidly. However, it is not easy to communicate the system because of the technological limitations in the present.

To exceed this critical point of promising products, these products should be reached a lower power consumption states, a lower unit cost of production, and a miniaturization as mentioned above. It should be developed the technology by the miniaturization of materials down to the micro- and nano- scale. To develop such products, it is inevitable that there would be experienced several trials and errors using these materials. Furthermore, to evolve these miniaturized products without any problems, first of all, we should study on the mechanical properties suit for the scale of material preferentially [34]. It is widely known that the characteristics of the material is changed when the size becomes small from bulk to atomic scale [35]. Consequently, it is required to verify that the characteristics of bulk sized mechanical properties established by many researchers remain in the micro-scale, nano-scale in the present, and even molecular scale in the future.

1.2   The history of evaluation method and results of mechanical properties of bulk material to thin film material

Mechanical properties at each material show their own unique characteristics. Some property may be a constant value or a function of independent variables, such as temperature and humidity. As we know, the types of mechanical properties are numerous. For example, compressive strength, ductility, fatigue limit, flexural modulus, flexural strength, fracture toughness, hardness, plasticity, Poisson's ratio, resilience, shear modulus, shear strain, shear strength, specific modulus, specific strength, specific weight, tensile strength, yield strength, Young's modulus, coefficient of friction, coefficient of restitution, roughness, and so on. Some material properties are calculated by simple relevant equations, but most mechanical properties are reliably measured by standardized test methods. Many researchers have been documented by their respective user communities and published through ASTM International. ASTM International, known until 2001 as the American Society for Testing and Materials, is an international standards organization that develops and publishes technical methods and standards for many materials properties. From founded in 1898, the society published the annual book of ASTM standards including measuring methods and results in books, CDs, and online publication. More than 13,000 ASTM standards are widely used today to evaluate the new alloy metals and new composited materials. For example, ASTM suggested many standard testing methods to measure the mechanical properties such as automated testing [36], impact testing [37-41], indentation hardness testing [42-48], micro-indentation hardness testing [49], and uniaxial testing [50-63], etcetera.

Among these methods, tensile testing method [64, 65], also known as tensile test and tension testing, is one of the most fundamental and basic material test method in which a sample is subjected to a controlled (generally uniaxial) tensile force until failure. Properties that are directly measured via the tensile test are ultimate tensile strength, maximum elongation, and reduction in area which depends on the materials. From this measurement, the following properties can be resolved like Young's modulus, Poisson's ratio, yield strength, and strain-hardening which means the strengthening of a metal by plastic deformation. Especially, uniaxial tensile testing method is the most commonly used for calculating the mechanical properties of iso-

tropic material. At the bulk and thin film size scale, sample for tensile specimen is a standardized by ASTM criteria. It has two grip parts and a gauge section in between. The radius of grip parts are larger than specimen part so they can be easily gripped, whereas the gauge has a smaller cross-section, which has various type of cross-section depend on the size, material on the specimen, and their own purpose. In order to perform these tensile tests, it is required to manufacture the tester by oneself at the laboratory or purchase the necessary equipment from manufacturing company.

The tensile test machines have their testing capability like maximum force capacity, minimum resolution capacity, strain rate, and data reliability. Before preparing the tensile test, the alignment of the test specimen in the uniaxial tensile testing machine is more critical than other tests. If the specimen is not aligned correctly, the specimen will be occurred the bending force, and impact on the error bound of data value directly [66]. In the brittle materials, these are especially distinguished from results of no bended specimens, because it will alter the results. These errors can be minimized by using spherical seals or U-joint [67] between the specimens.

The various systems for gripping specimen in bulk in ASTM organization have been established for a long period of time in order to get more precise results. For example, **Table 1.1 [65]** show the typical dimension of the round and flat type test specimen. Especially, to align the specimen correctly with applied loads, gripping systems have been developed by adding a threaded grip, serrated wedges, split collar on the round type test specimen, and serrated wedges and pin on the flat type test specimen, which is shown in **Fig. 1.3 [65]**. Also depending on the kind of materials, the specimens were to be manufactured by the standard roles provided in the ASTM criteria to reduce errors due to material characteristics. The official part names of test specimen and direction of the tensile test are shown as **Fig. 1.4 [65]**. Still now, tensile tests using new alloy metals or new composited materials following the ASTM manual are widely used not only to produce big components used in airplane and vessel, but also to produce H-shape steel materials in the high-rise construction field to improve mechanical properties [68, 69].

Next to the size of material from bulk to thin film, the definition of thin film, explaining in a brief way, is a thin layer of material. In other words, it means much thinner than the lateral dimensions of the substrate. But, depending on the academic fields, the range of size of thin

**Table 1.1** The dimension of the round and flat type test specimen by ASTM.

(a) round test specimen

All values in inches	Standard specimen at nominal diameter		Small specimen at nominal diameter		
	0.5	0.35	0.25	0.16	0.113
Gauge length	2.00±0.005	1.400±0.005	1.000±0.005	0.640±0.005	0.450±0.005
Diameter tolerance	±0.010	±0.007	±0.005	±0.003	±0.002
Fillet radius (min.)	$^3/_8$	0.25	$^5/_{16}$	$^5/_{32}$	$^3/_{32}$
Length of reduced section (min.)	2.5	1.75	1.25	0.75	$^5/_8$

(b) flat test specimen

All values in inches	Plate type (1.5 in. wide)	Sheet type (0.5 in. wide)	Sub-size specimen (0.25 in. wide)
Gauge length	8.00±0.01	2.00±0.005	1.000±0.003
Width	1.5 +0.125 -0.25	0.500±0.010	0.250±0.005
Thickness	$0.25 < T < {}^3/_{16}$	$0.005 \leq T \leq 0.25$	$0.005 \leq T \leq 0.25$
Fillet radius (min.)	1	0.25	0.25
Overall length (min.)	18	8	4
Length of reduced section (min.)	9	8	1.25
Length of grip section (min.)	3	2	1.25
Width of grip section (approx.)	2	0.75	$^3/_8$

film could have a wide difference. In this thesis, the range of thin film is up to 1 mm, and the range lower than 1 mm is classified as micro- or nano-scale material. Among the material of mm-scale, a plating method becomes the best suitable case. The plating method is a surface coating in which a metal is deposited on a conductive surface. Plating is not a new technology, it has been done for hundreds of years. It was used to decorate the items, to coat for corrosion inhibition, to improve solderability and wearability. For example, Jewelry is typically plated by silver or gold in terms of price advantage. Some researchers have been studied about mechanical properties of metal with plating [70]. These results have been impacted the way we live though we rarely recognized the fact.
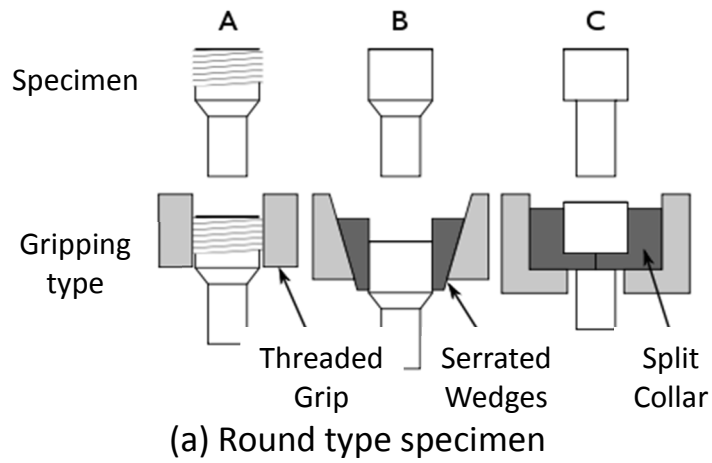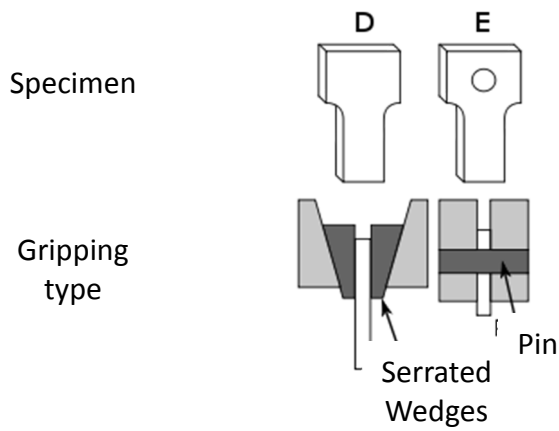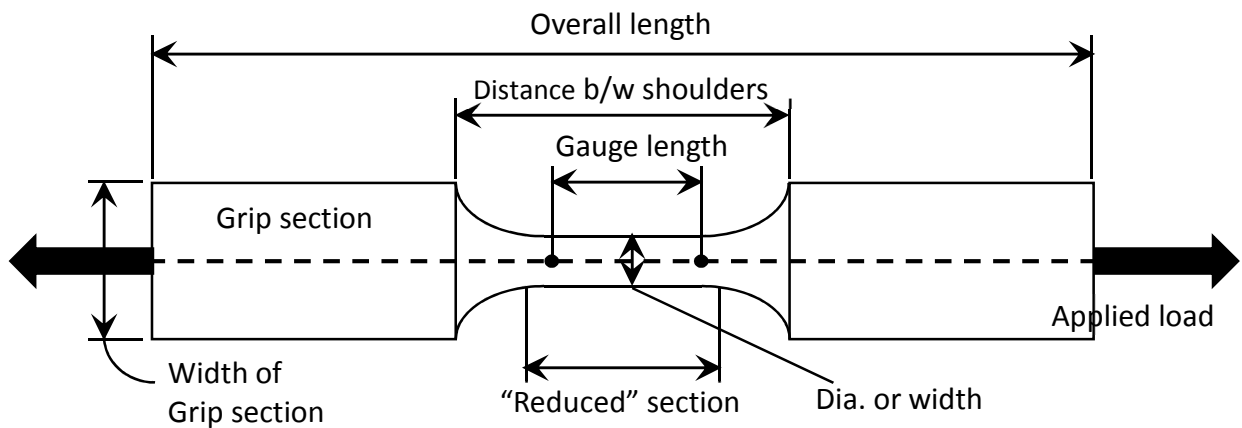
Fig. 1.3 Various kinds of methods for gripping tensile specimen : **A**. a threaded shoulder grips type, **B**. a serrated wedges type, **C**. a spilt collar butt end type, **D**. a serrated grips flat should type, **E**. a pinned grip flat shoulder with hole type.

Fig. 1.4 The schematic of test specimen on bulk size and the direction of applied load to the test specimen.

1.3   MEMS technology from 1990's to present

Since the 1990's, MEMS technology has been rapidly growing by an academic point of view. The reason that the micron scale components which were partially fabricated until then were become to make a single device with electrical and mechanical components through integration.

MEMS is a technology that can be defined as mechanical and electrical components in the same device using semiconductor device fabrication techniques in the similar way. The term "MEMS" is commonly used in USA and South Korea, whereas the system is referred to as MST in Europe, and Micro-machining or Micro-machines in Japan. Materials for MEMS device become boundless. Silicon was mostly used in the fabrication of IC and MEMS because of significant advantages of mechanical properties. In spite of material advantages of silicon, polymer such as PMMA, metals such as chrome (chromium), copper, aluminum, and gold, and ceramics such as silicon nitride became gradually adapted for MEMS material as suitable substitutes. Besides, new emerging materials like CNT and grapheme, which have good conductivity and reliability, are adopted for materials of MEMS.

However, life cycle of the device which was made by MEMS technology was extremely shorter (only a couple of hours to days) than expected, it was not practicable to use conveniently. If once the problem of duration is solved and these products are commercialized, devices from micro- to even nano- scale using semiconductor processing technology would have advantages of miniaturization, weight lightening, and low production cost than bulk scale devices. For that reason, many national research institutions and academically renowned laboratories including Sandia National Laboratory.

Researchers are continue to develop a device with excellent ideas and to try to success in commercialization. At present, application devices using MEMS technology are limited to car airbag sensor, inkjet cartridge, endoscopic microcapsule, pressure sensor, microphone, accelerometer, gyroscope, magnetometer, micro- dispensers and so on. However, these are not enough items than expected. Car airbag sensor is one of the first commercialized device using MEMS technology. It is widely used in the form of a single chip containing an accelerometer. Inkjet cartridge also by MEMS technology consists of IC and inkjet head, which has nozzle, holes, manifolds, and channel structures for high performance. Now, most of sensors used in smart-

phones such as accelerometers, gyroscopes, pressure sensor, and microphone are fabricated by MEMS technology for miniaturization and cost advantages.

Next, MEMS application is classified by type of usage this time and summarized in **Table 1.2**. There are sensor, actuator, Bio-MEMS, and Power-MEMS. To describe briefly, sensor, which is widely used in bulk size sensor, is one of the most designed and developed field among MEMS technology. There are semiconductor pressure sensor, chemical sensor, and inertia sensors (accelerometer sensor, force sensor, gyroscope) to be manufactured using MEMS technology. These sensors are mostly made using the principle of piezo effect, which means transferring mechanical change amount from mechanical elongation to electronic signal, to the materials of semiconductors. Therefore, it is very important to improve elongation sensitivity of sensors to commercialize as soon as possible. These sensors are now used for the tire, fuel, oil, air flow, and absolute air pressure in the car. Actuator is a significant element to miniaturization and high performance for MEMS device. The driving systems of Micro Actuator are electro-static force, electro-magnetic force, photo-effect, piezo-electric effect, shape memory alloy, thermal expansion, and etc. These systems should be chosen considering user conditions. Bio-MEMS is a technology to apply on the medical field using semiconductor processing technology, and it is one of the most promising MEMS applications at this time. Because μ-TAS technology, one of the representative in Bio-MEMS technology, could be a precise dispensing for small amount of liquids found in needleless drug delivery system [71, 72]. Also endoscopic microcapsule is one of the most exciting items on this technology. Power-MEMS means a small combustion facility using semiconductor processing technology. There are micro-scale gas turbine and micro-scale rocket which are fabricated from 6 individually processed silicon wafers from Power-MEMS technology. The both of devices have thermal deformation of materials due to a rapid temperature rise, it is necessary to evaluate the mechanical properties at high temperature.

Table 1.2 Categorization of MEMS application

Categories		MEMS application
MEMS	Sensor	Pressure sensor
		Chemical sensor
		Inertia sensor (accelerometer sensor, force sensor, gyroscope)
	Actuator	Electro-static force
		Electro-magnetic force
		Photo-Effect
		Piezo-electric effect
		Shape memory alloy
		Thermal expansion
	Bio-MEMS	μ-TAS
	Power-MEMS	Micro-scale gas turbine
		Micro-scale rocket

1.4   The evaluation method and the results of mechanical properties of micro- and nano-material using MEMS technology by other researchers

Despite the fact that MEMS devices have been introduced on the market about 40 years ago, the industry has not reached to certain degree of advancement and is still increasing gradually. However, new emerging MEMS devices that could be the killer application for the future trend such as thermopiles [73, 74], micro-display [75, 76], micro-mirrors for mobile phone and tablet embedded pico-projectors [77], Auto focus [78] are continuously introduced in the market. Especially RF MEMS switches are partially developed and commercialized as a prototype version and still under development. Fig. 1.5 [79] shows the period for Research & Development to commercial ramp-up. It took 36 years for pressure sensor, but auto focus only 17 years. Recently, Yole Development Company predicted that MEMS market is expected to reach extra growth in the future shown in Fig. 1.6 [79].

MEMS is produced using similar method used in the fabrication of semiconductor, Silicon is definitely the most widely used substrate material in MEMS. In addition, the alloy metals and pure metals like Au which is related to chapter 3, ceramics like silicon nitride which is related to chapter 2, polymers, and allotropes of carbon like carbon nanotube which is related to chapter 4 are gradually used for special purpose. To manufacture the MEMS devices that have high
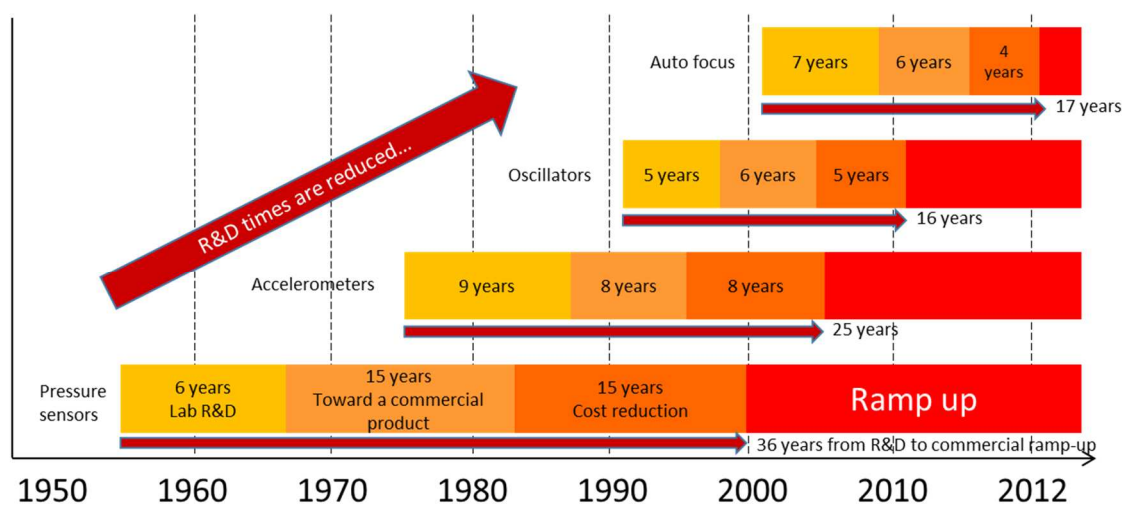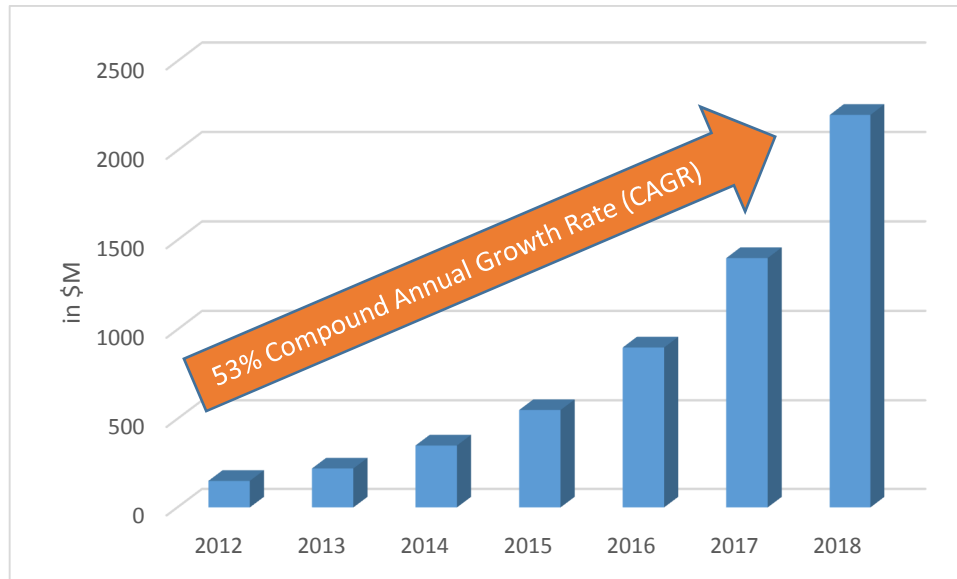

Fig. 1.5 The graph related to development time about each item.

Fig. 1.6 Emerging MEMS market 2012-2018.

performance and reliability, it is necessary to fully understand these mechanical properties until the nano-scale materials. As the scale of the material is reduced to reach the nano-scale regime, it is possible that the same material will show you the totally different properties (Young's modulus, Fracture strength, and so on) **[80]**.

This was a matter at the nano-scale no longer follows Newton physics but rather quantum mechanics. For example, T. Namazu *et al.* **[81]** reported that comparisons of Young's modulus and bending strength, of Si among the nano-, micro-, and mm-scales showed that specimen size produced a large effect on the bending strength. This thesis showed a method to evaluate the mechanical properties of micro- and nano-scale materials by micro- and nano-scale tensile testing systems which were developed in the laboratory.

This was a matter at the nano-scale no longer follows Newton physics but rather quantum mechanics. For example, T. Namazu *et al.* **[81]** reported that comparisons of Young's modulus and bending strength, of Si among the nano-, micro-, and **mm**-scales showed that specimen size produced a large effect on the bending strength. This thesis showed a method to evaluate the mechanical properties of micro- and nano-scale materials by micro- and nano-scale tensile testing systems which were developed in the laboratory.

The methods to measure the mechanical properties of MEMS materials are classified not only tensile test, but also compression test, micro-beam bending test, bulge test, M-test, dynamic (resonant) test, nano-indentation, and etc. In this thesis, as mentioned earlier, tensile

test for evaluating the mechanical properties will be mainly discussed. Tensile test is a uniaxial extension until failure, and can characterize the Young's modulus, yield strength, fracture strength, and so on. A uniaxial, tensile load is applied to a specimen with a gauge section of uniform geometry, and the extension of the gauge is recorded as a function of the applied load. Given the dimensions of the beam, it is straightforward to obtain a stress-strain graph, and to extract E, σ_Y, and σ_f.

The direction of compression test is opposite to tensile test, and mainly used to study plasticity [82]. The first compression test at the micro-scale [83] was performed in micro-pillar. From a technical point of view, it is easy to measure the data than tensile test because the gripping technique could not be need. Micro-beam bending test [81] is easy to set-up the specimen and equipment for testing. But, it allow one to determine a few of mechanical properties such as Young's modulus, Poisson's ratio, and residual stresses. Bulge test was proposed by Vlassax & Nix in 1992 [84]. The specimen is a membrane bonded along the supporting frame. Pressure is applied to one side of membrane, the resulting deflection is recorded. From this test, the biaxial stress-strain curve and the yield strength, and plasticity size effects are resolved [85]. M-test is a micro-beam, loaded by an electrostatic force until the onset of instability. By this test, Young's modulus and the residual stress can be only derived. The principal difficulty associated with this technique is the handling and mounting of the test structures. In the case of brittle materials, fracture induced by gripping presents an additional problem. One solution adopted by many researchers is to fabricate the test structure in a protective frame, and to sever the frame mechanically after mounting, [86, 87] Electrostatic gripping techniques [88, 89] and pull tests inside a scanning electron microscope [89, 90] have also been demonstrated. Materials that have been characterized using the micro tensile test include single-crystal silicon [91], poly-silicon [92], and aluminum [93].

As described in the previous section, mechanical properties can be changed into micro-and nano-scale. Therefore we have to measure the mechanical properties using various test methods for design from 3-dimensional simulation first to finally manufacturing the MEMS devices without any problem. Among the values of the mechanical properties, modulus of elasticity (=Young's modulus), Poisson's ratio, and fracture strength are essentially using the mechanical design. **Table 1.3 [94]** summarizes the general mechanical properties at macro-scale. It is clear that silicon is very attractive material for general use because of high fracture strength than

Table 1.3 Mechanical properties of representative MEMS materials
at macro-scale.

Material	Density, ρ	Modulus, E	Fracture Strength, σ_f
	kg/m^3	GPa	MPa
Silicon	2,330	129-187	4000
Silicon oxide	2,200	73	1000
Silicon nitride	3,300	304	1000
Aluminum	2,710	69	300
Aluminum oxide	3,970	393	2000
Gold	19,320	79	-
Chromium	7,200	279	-

other materials. However, Silicon nitride and aluminum oxide could be suitable for devices in which specific stiffness is needed.

In this thesis, chapter 2 to 4 carried on tensile test of each material:

A. *Selecting the material mainly using MEMS technology.*
B. *Deciding the dimensions of specimen.*
C. *After that, tensile testing system is designed and self-developed.*
D. *Device is fabricated by myself in our laboratory or co-worked.*
E. *Tensile test is carried out at various conditions such as changing the strain rate, pressure, and temperature.*
F. *The result data are calculated and analyzed.*

Until micro-scale tensile test, test system composed of an actuator, load cell, displacement sensor like macro-scale tensile testing system. To decrease the scale of specimen, EANAT, which is designed and self-developed, consisted of an electrostatically driven actuator and a cantilever beam used as a gauge to measure tensile displacement with an optical microscope. This all-in-one fabrication does not require the specimen fixation procedure, and enables the high precision in the specimen alignment direction, which therefore could easily carry out the tensile test. Since fixation procedure of specimen influence the accuracy of result data, the accuracy was increased. In order to measure the MWCNTs which has around 100 **nm** of a diameter, this

research has integrated a circular motion capacitive displacement sensor into an EANAT to realize more precise calibration of the sensor. Also, *In-situ* SEM nano-tensile testing using a nano-manipulation system was carried out for direct observations of the deformation behavior of samples during testing. This thesis reports the design and functions of the newly developed EANAT, as well as details of the mechanical characteristics of individual MWCNTs.

1.5   Objectives and organization of this thesis

This doctoral dissertation is composed of totally five chapters, and the contents of each chapter are organized as follows.

Chapter 1 raised a question on why we should evaluate the mechanical properties of micro- and nano- scale materials, and explained the history of evaluation method and results of mechanical properties of bulk material to thin film material. Next, MEMS technology from 1990's to present was illustrated. Finally, the evaluation method and the results of mechanical properties of micro- and nano-material using MEMS technology by other researchers was described into details.

Chapter 2 investigated the effect of deposition condition on the mechanical properties of submicron thick PE-CVD silicon nitride film (SiNx) on the SCS specimens that is depending on the gas flow ratio of mono-silane to ammonia to nitrogen. This study showed that elastic properties of PE-CVD SiNx films were greatly influenced by the gas flow ratio of NH$_3$ to SiH$_4$.

Chapter 3 developed the tensile testing device for Au thin films in the thickness of sub-100-nm. The obtained mechanical properties showed that apparent differences from those of the bulk Au. Thus, direct tensile test of extremely thin Au films revealed the strong influence of material fabrication process on the mechanical properties.

Chapter 4 showed the stress-strain relations, the interlayer sliding deformation behavior and the breaking mechanism of individual MWCNTs by newly designed EANAT. A tensile testing methodology was established on the *in-situ* SEM nano-manipulation system. Accurate load-displacement curves are successfully obtained in this study. However, for estimating the interlayer shear strength based on quasi-static friction of single-shot extraction of MWCNTs, further investigation of cyclic tensile loading testing with an ultra-low strain rate oscillation and small displacement need to be carried out.

Finally, **chapter 5** shows the summarized conclusion of this thesis.

References

[1]   L. Capodieci: Beyond 28nm: New Frontiers and Innovations in Design For Manufactura-
       bility at the Limits of the Scaling Roadmap, GLOBALFOUNDRIES®, Presentation Data, p.5,
       2012.

[2]   Recent Market Research Reports at Fuji Chimera Research Institute, Inc. Published on
       2012.

[3]   M. Tsuji, T. Aramoto, H. Ohyama, T. Hibino, and K. Omura: Characterization of CdS this
       film in high efficient CdS/CdTe solar cells, *Journal of Crystal Growth*, vol. 214-215, pp.
       1142-1147, 2000.

[4]   S. Ikegami: CdS/CdTe solar cells by the screen-printing-sintering technique: Fabrication,
       photovoltaic properties and applications, *Solar Cells*, vol. 23, issues 1-2, pp. 89-105, 1988.

[5]   A. V. Shah, H. Schade, M. Vanecek, J. Meier, E. Vallat-Sauvain, N. Wyrsch, U. Kroll, C. Droz,
       and J. Bailat: *Thin-film Silicon Solar Cell Technology, Progress in Photovoltaics: Research
       and Applications*, vol. 12, pp. 113-142, 2004.

[6]   E. Garnett and P. Yang: Light Trapping in Silicon Nanowire Solar Cells, *Nano Letters*, vol.
       10, pp. 1082-1087, 2010.

[7]   J. Zhu, C.-M. Hsu, X. Yu, S. Fan, and Y. Cui: Nanodome Solar Cells with Efficient Light Man-
       agements and Self-Cleaning, *Nano Letters*, vol. 10, no. 6, pp. 1979-1984, 2010.

[8]   F. Kessler and D. Rudmann: Technological aspects of flexible CIGS solar cells and modules,
       Solar Energy, vol. 77, issue 6, pp. 685-695, 2004.

[9]   T. Kokusho, E. Emoto, and T. Kato: Sailing Solar-Cell Raft Project and Weather and Marine
       Conditions in Low-Katitude Pacific Ocean, Journal of Energy Engineering, vol. 139, issue
       1, pp. 2-7, 2013.

[10]   C. G. Granqvist: Transparent conductors as solar energy materials: A panoramic review,
       Solar Energy Materials and Solar Cells, vol. 91, issue 17, pp. 1529-1598, 2007.

[11]   B. Parida, S. Iniyan, and R. Goic: A review of solar photovoltaic technologies, *Renewable
       and Sustainable Energy Reviews*, vol. 15, issue 3, pp. 1625-1636, 2011.

[12]   J. Y. Song, Y. Y. Wang, and C. C. Wan: Review of gel-type polymer electrolytes for lithium-
       ion batteries, *Journal of Power Sources*, vol. 77, issue 2, pp. 183-197, 1999.

[13] S. S. Zhang: A review on electrolyte additives for lithium-ion batteries, *Journal of Power Sources*, vol. 162, issue 2, pp. 1379-1394, 2006.

[14] W. H. Meyer: Polymer Electrolytes for Lithium-Ion Batteries, *Advanced Materials*, vol. 10, issue 6, pp. 439-448, 1998.

[15] J. Stromback, C. Dromacque, MH Yassin, and VaasaETT, Global Energy Think Thank: The potential of smart meter enabled programs to increase energy and systems efficiency: a mass pilot comparison Short name: Empower Demand, *project funded by ESMIG*, book, 2011.

[16] S. Darby: Smart metering: what potential for householder engagement?, *Building Research and Information*, vol. 38, issue 5, pp. 442-457, 2010.

[17] A. Nishino: Capacitors: operating principles, current market and technical trends, *Journal of Power Sources*, vol. 60, issue 2, pp. 137-147, 1996.

[18] M. Jayalakshmi and K. Balasubramanian: Simple Capacitors to Supercapacitors – An Overview, *International Journal of Electrochemical Science*, vol. 3, pp. 1196-1217, 2008.

[19] T. Kamiya, K. Nomura, and H. Hosono: Reresent status of amorphous In-Ga-Zn-O thin film transistors, *Science and Technology of Advanced Materials*, vol 11, 044305(23pp), 2010.

[20] Z. Ye, M. Wong, M. Ng, J.K. Luo: High stability fluorinated zinc oxide thin film transistor and its application on high precision active-matrix touch panel, *Electron Devices Meeting (IEDM) 2013 IEEE International*, pp. 27.2.1-4, 2013.

[21] A. B. Hargadon and Y. Douglas: When Innovations Meet Institutions: Edison and the Design of the Electric Light, *Administrative Science Quarterly*, vol. 46, pp. 476-501, 2001.

[22] M. A. Hermandez-Rodriguez, M. H. Imanieh, L. L. Martin, and I. R. Martin: Experimental enhancement of the photocurrent in a solar cell using upconversion process in fluoroindate glasses exciting at 1480nm, *Solar Energy Materials and Solar Cells*, vol. 116, pp. 171-175, 2013.

[23] W. Ma, C. Yang, X. Gong, K. Lee, and A. J. Heeger: Thermally stable, Efficient Polymer Solar Cells with Nanoscale Control of the Interpenetrating Network Morphology, *Advanced Functional Materials*, vol. 15, issue 10, pp. 1617-1622, 2005.

[24] M. Law, L. E. Greene, J. C. Johnson, R. Saykally, and P. Yang: Nanowire dye-sensitized solar cells, *Nature materials*, vol. 4, pp. 455-459, 2005.

[25] E. Klampaftis, D. Ross, K. R. McIntosh, and B. S. Richards: Enhancing the performance of solar cells via luminescent down-shifting of the incident spectrum: A review, *Solar Energy Materials and Solar Cells*, vol. 93, issue 8, pp. 1182-1194, 2009.

[26] A. Hagfeldt, G. Boschloo, L. Sun, L. Kloo, and H. Pettersson: Dye-Sensitized Solar Cells, *Chemical Reviews*, vol. 110, issue 11, pp. 6595-6663, 2010.

[27] J.-A. Laila, H. Iddir, L. A. Curtiss, and M. C. Hersam: Influence of Electronic Type Purity on the Lithiation of Single-Walled Carbon Nanotubes, *ACS Nano*, vol. 8, issue 3, pp. 2399-2409, 2014.

[28] Federal Energy Regulatory Commission: Assessment of Demand Response and Advanced Metering, Staff Report, 2008.

[29] Z. M. Fadlullah, M. M. Fouda, N. Kato, A. Takeuchi, N. Iwasaki, and Y, Nozaki: Toward intelligent machine-to-machine communications in smart grid, *Communications Magazine, IEEE*, vol. 49, issue 4, pp. 60-65, 2011.

[30] S. S. S. R. Depuru, L. Wang, V. Devabhaktuni: Smart meters for power grid: Challenges, issues, advantages and status, *Renewable and Sustainable Energy Reviews*, vol. 15, issue 6, pp. 2736-2742, 2011.

[31] R. H. Khan and J. Y. Khan: A comprehensive review of the application characteristics and traffic requirements of a smart grid communications network, *Computer Networks*, vol. 57, issue 3, pp. 825-845, 2013.

[32] V. C. Gungor, D. Sahin, T. Kocak, S. Ergut, C. Buccella, C. Cecati, and G. P. Hancke: Smart Grid Technologies: Communication Technologies and Standards, *IEEE Transactions on Industrial Informatics*, vol. 7, issue 4, pp. 529-539, 2011.

[33] S. Galli, A. Scaglione, Z. Wang: For the Grid and Through the Grid: The Role of Power Line Communications in the Smart Grid, *Proceedings of the IEEE*, vol. 99, issue 6, pp. 998-1027, 2011.

[34] M. F. Ashby and D. Cebon: Materials selection in mechanical design, Journal De Physique IV, vol. 3, pp. 1-9, 1993.

[35] E. Arzt: Size effects in materials due to microstructural and dimensional constraints: a comparative review, *Acta Materialia*, vol. 46, issue 16, 1998.

[36] Standard Guide for Evaluating Computerized Data Acquisition Systems Used to Acquire Data from Universal Testing Machines, ASTM E1856-13.

[37] Standard Test Methods for Notched Bar Impact Testing of Metallic Materials, ASTM E23-12C.

[38] Standard Test Method for Conducting Drop-Weight Test to Determine Nil-Ductility Transition Temperature of Ferritic Steel, ASTM E208-06(2012).

[39] Standard Test Method for Dynamic Tear Testing of Metallic Materials, ASTM E604-83 (2008).

[40] Standard Test Method for Impact Testing of Miniaturized Charpy V-Notch, ASTM E2248-13.

[41] Standard Test Method for Instrumented Impact Testing of Metallic Materials, ASTM E2298-13a.

[42] Standard Test Method for Brinell Hardness of Metallic Materials, ASTM E10-12.

[43] Standard Test Method for Rockwell Hardness of Metallic Materials, ASTM E18-14.

[44] Standard Practice for Rapid Indentation Hardness Testing of Metallic Materials, ASTM E103-12

[45] Standard Test Method for Indentation Hardness of Metallic Materials by Portable Hardness Testers, ASTM E110-10

[46] Standard Hardness Conversion Tables for Metals Relationship Among Brinell Hardness, Vickers Hardness, Rockwell Hardness, Superficial Hardness, Knop Hardness, Scleroscope Hardness, and Leeb Hardness, ASTM E140-12be1.

[47] Standard Practice for Scleroscope Hardness Testing of Metallic Materials, ASTM E448-82 (2008).

[48] Standard Practice for Instrumented Indentation Testing, ASTM E2546-07.

[49] Standard Test Method for Knop and Vickers Hardness of Materials, ASTM E384-11e1.

[50] Standard Test Methods for Tension Testing of Metallic Materials, ASTM E8/E8m-13a.

[51] Standard Test Methods of Compression Testing of Metallic Materials at Room Temperature, ASTM E9-09.

[52] Standard Test Methods for Elevated Temperature Tension Tests of Metallic Materials, ASTM E21-09.

[53] Standard Test Method for Young's Modulus, Tangent Modulus, and Chord Modulus, ASTM E111-04 (2010).

[54] Standard Test Method for Poisson's Ratio at Room Temperature, ASTM E132-04 (2010).

[55] Standard Test Methods for Conducting Creep, Creep-Rupture, and Stress-Rupture Tests of Metallic Materials, ASTME139-11.

[56] Standard Test Method for Shear Modulus at Room Temperature, ASTM E143-02 (2008).

[57] Standard Practice for Compression Tests of Metallic Materials at Elevated Temperatures with Conventional or Rapid Heating Rates and Strain Rates, ASTM E209-00 (2010).

[58] Standard Test Method for Pin-Type Bearing Test of Metallic Materials, ASTM E238-12.

[59] Standard Test Methods for Conducting Time-for-Rupture Notch Tension Tests of Materials, ASTM E292-09e1.

[60] Standard Test Methods for Stress Relaxation Tests for Materials and Structures, ASTM E328-02 (2008).

[61] Standard Test Methods of Tension Testing of Metallic Foil, ASTM E345-93 (2008).

[62] Standard Guide for Use of Thermocouples in Creep and Stress-Rupture Testing to 1800℉(1000℃) in Air, ASTM E633-13.

[63] Standard Test Method for Tension Testing of Structural Alloys in Liquid Helium, ASTM E1450-09.

[64] H. Czichos, T. Saito, and L. Smith: Springer Handbook of Materials Measurement Method, Berlin: *Springer*, pp.303-304, 2006.

[65] J. R. Davis: Tensile Testing 2nd ed., ASM International, ISBN 978-0-87170-806-9, 2004.

[66] G. I. Taylor and C. F. Elam: Bakerian Lecture. The Distortion of an Aluminium Crystal during a Tensile Test, *Proceedings of The royal society A*, vol. 102, 1923.

[67] P. Clark: Protocol for Fabrication, Inspection, Testing, and Documentation of Beam-Column Connection Tests and Other Experimental Specimens, SAC Steel Project, Background Document, 1997.

[68] G. M. Pharr and W. C. Oliver: Measurement of Thin Film Mechanical Properties Using Nanoindentation, *MRS Bulletin*, vol. 17, issue 7, pp.28-33, 1992.

[69] S. S. Manson: Behavior of materials under conditions of thermal stress, *National Advisory Committee for Aeronautics*, Technical note 2933, 1953.

[70] L. Shi, C. Sun, P. Gao, F. Zhou, and W. Liu: Mechanical properties and wear and corrosion resistance of electrodeposited Ni-Co/SiC nanocomposite coating, *Applied Surface Science*, vol. 252, pp.3591-3599, 2006.

[71] A.C.R. Grayson, R.S. Shawgo, A.M. Johnson, and N.T. Flynn: A BioMEMS review: MEMS technology for physiologically integrated devices, *Proceedings of the IEEE*, vol. 92, issue 1, pp. 6-21, 2004.

[72] P. Cooley, D. Wallace, and B. Antohe: Applications of Ink-Jet Printing Technology to BioMEMS and Microfluidic Systems, *Biochemical Research Method*, vol. 7, no. 5, pp.33-39, 2002.

[73] J. Xie, C. Lee, and H. Feng: Design, Fabrication, and Characterization of CMOS MEMS-Based Thermoelectric Power Generators, *Journal of Microelectromechanical Systems*, vol. 19, no. 2, pp. 317-324, 2010.

[74] L. Sin, T. Pan, C. Tsai, and C. Chou: Multifunction thermopile sensors fabricated with a MEMS-compatible process, *Semiconductor Manufacturing, IEEE Transactions*, vol.26, issue 2, pp. 242-247, 2013.

[75] U. Baran, D. Brown, S. Holmstrom, D. Balma, W. O. Davis, P. Muralt, and H. Urey: Resonant PZT MEMS Scanner for High-Resolution Displays, *Journal of Microelectromechanical Systems*, vol. 21, no. 6, 2012.

[76] K. Hirabayashi, H. Takenaka, O. Konuma, Y. Morimoto, and Y. Takaki: Multi-view display module using MEMS projectors for an ultra-large screen autostereoscopic display, *SPIE Proceedings*, vol. 8648, 2103.

[77] H. Gruger, T. Pugner, J. Knobbe, and H. Schenk: First application close measuprements applying the new hybrid integrated MEMS spectrometer, *MEMS- and MOEMS-Based Spectrometers*, 2013.

[78] H. Hsieh, H. Wei, M. Lin, W. Hsu, Y. Cheng, and G. Su: Thin autofocus camera module by a large-stroke micromachined deformable mirror, Optical Society of America, vol. 18, no. 11, pp. 11097-11104 , 2010.

[79] YOLE, Emerging MEMS 2013.

[80] E. Arzt: Size effects in materials due to microstructural and dimensional constraints: a comparative review, *Acta Materialia*, vol. 46, issue 16, 1998.

[81] T. Namazu, Y. Isono, T. Tanaka: Evaluation of size effect on mechanical properties of single crystal silicon by nanoscale bending test using AFM, *Journal of Microelectromechanical Systems*, vol. 9, issue 4, pp. 450-459, 2000.

[82] M. D. Uchic, D. M. Dimiduk, J. N. Florando, and W. D. Nix: Sample dimensions influence strength and crystal plasticity, *Science*, vol. 305, pp. 986-989, 2004.

[83] M. F. Pantano, H. D. Espinosa, and L. Pagnotta: Mechanical characterization of materials at small length scales, vol. 26, issue 2, pp.545-561, 2012.

[84] J. J. Vlassak and W. D. Nix: A new bulge test technique for the determination of Young's modulus and Poisson's ratio of thin films, *Journal of Materials Research*, vol. 7, issue 12, pp. 3242-3249, 1992.

[85] Y. Xiang and J. J. Vlassak: Bauschinger and size effects in thin-film plasticity, *Acta Materialia*, vol. 54, pp.5449-5460, 2006.

[86] W. A. Brantley: Calculated elastic constants for stress problems associated with semiconductor devices, *Journal of Applied Physics*, vol. 44, no. 1, pp. 534-535, 1973.

[87] S. Lapman: ASM handbook vol.2 (ASM International,cleveland,1990).

[88] W.N. Sharpe, B. Yuan, and R.L. Edwards: A New Technique for Measuring the Mechanical Properties of Thin Film, *Journal of Microelectromechanical Systems*, vol. 6, no. 3, pp. 193-199, 1997.

[89] M. Kiuchi, S. Matsui, Y. Isono: Mechanical Characteristics of FIB Deposited Carbon Nanowires Using an Electrostatic Actuated Nano Tensile Testing Device, *Journal of Microelectromechanical Systems*, vol. 16, no. 2, pp. 191-201, 2007.

[90] M. Kiuchi, S. Matsui, Y. Isono: The piezoresistance effect of FIB-deposited carbon nanowires under severe strain, *Journal of Micromechanics and Microengineering*, vol. 18, 065011, 2008.

[91] W. Suwito, M. L. Dunn, S. J. Cunningham, and D. T. Read: Elastic Moduli, Strength, and Fracture Initiation at Sharp Notches in Etched Single Crystal Silicon Microstructrues, *Journal of Applied Physics*, vol. 85, no. 7, pp. 3519-3534, 1999.

[92] T. Tsuchiya, O. Tabata, J. Sakata, and Y. Taga: Specimen Size Effect on Tensile Strength of Surface-Micromachined Polycrystalline Silicon Thin Films, *Journal of Microelectromechanical Systems*, vol. 7, no. 1, pp. 106-113, 1998.

[93] H. J. Lee, G. Cornella, and J. C. Bravman: Stress Relaxation of Free-Standing Aluminum Beams for Microelectromechanical Systems Applications, *Applied Physics Letters*, vol. 76, no. 23 pp. 3415-3417, 2000.

[94] S.M. Spearing: Materials Issues in Microelectromechanical Systems (MEMS), *Acta Materialia*, vol. 48, pp. I79-196, 2000.

Chapter 2

Influence of Gas Flow Ratio in PE-CVD Process on Mechanical Properties of Silicon Nitride Film

2.1   Introduction

Silicon nitride is a chemical compound of silicon (Si) and nitrogen (N), and the combination of the formula is Si_3N_4. This material has lots of other silicon nitride phases which could be determined by time, temperature, and many conditions. More accurately, the silicon nitride films are found to contain atoms of Si, N, hydrogen (H), oxygen (O), and carbon (C). In this chapter, silicon nitride film varies due to the ratio of Si and N, and it will be referred and represented as SiN_x.

SiN_x films are typically employed as an etching stop layer both for wet and dry etching of Si in MEMS fabrication processes due to their chemical inertness [1, 2]. SiN_x films also possess excellent electrical isolation and strong resistance to oxidation, so that they are suitable for a passivation coating in MEMS [3, 4]. SiN_x films can be deposited on a substrate by the PE-CVD and low-pressure chemical vapor deposition (LP-CVD). Each deposition method and condition determines the composition of films that induce wide variations in material characteristics. Mechanical properties of SiN_x films prepared at each deposition condition should be, then, evaluated before a practical usage of the films as a mechanical component in MEMS component.

Several evaluation techniques have so far been proposed to measure the mechanical properties of thin films, such as nano-indentation test [5], tensile test [6-8], bending test [9], acoustic test [10], bulge test [8, 11], and etc. Each test technique is available to mechanical characterization for submicron films. However, the mechanical characterization for submicron films using bulge and bending methods should be carefully performed because of a geometrical large deformation of sample under loading. The nano-indentation test can evaluate only plane-strain modulus of the films. In the acoustic test, density and Poisson's ratio of the films are required for estimating Young's modulus before the test. On the other hand, tensile test is superior as

an easy and accurate measurement of stress-strain relation of submicron films, if the longitudinal elongation at the gauge section of a specimen can be measured precisely during the test. Our laboratory have, so far, developed the Atomic Force Microscope (AFM) tensile tester for direct measurement of stress-strain curve for the diamond-like carbon (DLC) film on the coated single crystal silicon (SCS) specimens (DLC/SCS specimens) in the previous work [12]. Here, we succeeded in evaluating Young's modulus of the submicron DLC film by measuring longitudinal elongation at the gauge section of the specimen during tensile loading. Nano-indentation test, in addition to the tensile test, was also performed to determine Poisson's ratio of the submicron DLC film.

The objective of this research is to investigate the effect of deposition condition on the mechanical properties of submicron PE-CVD SiNx films, in order to guarantee the performance and life extension of SiNx coated in MEMS. The submicron SiNx films were deposited on the micro-scale SCS specimens by changing the gas flow ratio of mono-silane (SiH$_4$) to ammonia (NH$_3$) to nitrogen gas (N$_2$). The uniaxial tensile tests were carried out to evaluate Young's modulus and fracture strength using the AFM tensile test technique established in the previous work [12]. Poisson's ratio of SiNx films was also evaluated by assistance of nano-indentation tests. Finally, Auger spectroscopic analysis clarifies the influence of the atomic content ratio on elastic properties of SiNx films.

2.2 Specimen Preparation and AFM Based Tensile Testing System

Fig. 2.1 shows the SiNx film coated on the SCS specimen (SiNx/SCS specimen) along with a close-up view of the gauge section, which consists of a gauge section, two square holes (hooking holes), an outside frame for easy handling and three supporting strips to prevent the specimen from fracturing before tensile test. All SiNx/SCS specimens were fabricated by depositing submicron SiNx films on the SCS specimens using two kinds of PE-CVD machines (PE-CVD machine #1 and #2). The PE-CVD machine #1 installed a larger electrode plate of 617 cm^2, whereas the machine #2 had an electrode plate of 205 cm^2. The fabrication process as shown in **Fig. 2.2** started with oxidation of a silicon-on-insulator (SOI) wafer composed of 10 μm SCS device layer with the (001) plane and 1 μm SiO$_2$ buried oxide (BOX) layer on 380 μm SCS carrier wafer. Wet thermal oxidation was employed to form SiO$_2$ layer with a thickness of 0.7 μm used as an etching mask on the entire surface of the wafer. First, the square holes were fabricated from the topside of the specimen by anisotropic wet etching with 20 % tetra-methyl ammonium hydroxide (TMAH) solution at 363 **K**. Simultaneously, the 380 μm SCS substrate beneath the gauge section was etched from the backside. Chromium (Cr) film was deposited on the topside of the wafer by thermal vacuum evaporation, followed by patterning the specimen shape. The reactive ion etching (RIE) process formed the gauge section of the specimen using the Cr film as an etching mask for SF$_6$ gas, and subsequently the Cr film was removed. Here, the gauge section
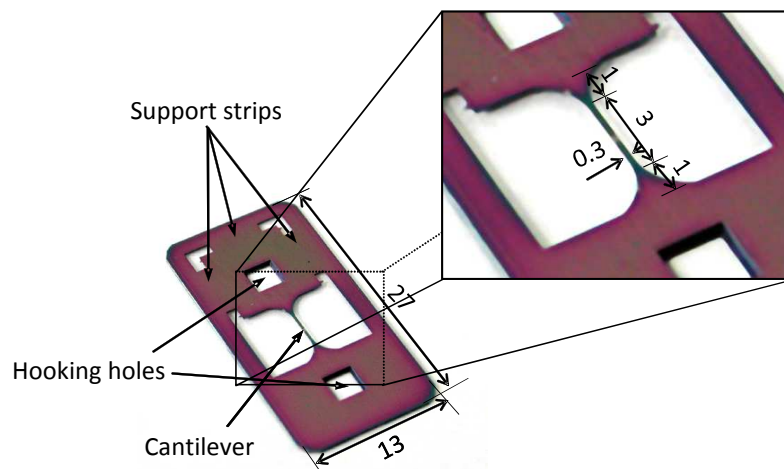
Fig. 2.1 Photograph of SiNx/SCS specimen for tensile test, along with a close-up view of the gauge section. (unit: mm).

#	Process	Figure	Condition	Comment

Process Name: Specimen for silicon nitride film
Name: HYUN-JIN OH   *Isono Lab.*

0) SOI Wafer

A-A' cross-section

Top View   Bottom View

■ Photo Mask
□ Si
■ SiO$_2$
■ Si$_3$N$_4$
■ Dicing Sheet
■ Photoresist
■ Cr

1) Thermal Oxidation

2) Dicing Wafer

① Spin coating of P.R.

Spin coating of P.R.
-P.R. : OFPR800 50cp
-Rotation Speed : 3000rpm
-Time : 25sec

Baking in Oven
-Temperature : 110℃
-Time : 50min

② Pasting of Dicing Sheet

③ Dicing Wafer

④ Striping of Dicing Sheet
And Cleaning

Wet Etching P.R ;
-Etchant : Acetone
-Time : 3min
Rinsing
-Ethanol Rinsing : 3min
-Pure Water Rinsing : 30min

1st Cleaning ;
-H$_2$O$_2$: H$_2$SO$_4$ = 1 : 2
-Time : 10min
-Pure Water Rinsing : 10min

2nd Cleaning ;
-H$_2$O : H$_2$O$_2$: NH$_3$ = 5 : 1 : 1
-Time : 10min
-Temperature : 80℃
-Pure Water Rinsing : 30min

Fig. 2.2 Process chart of SiNx/SCS specimen (continued).

#	Process	Figure	Condition	Comment
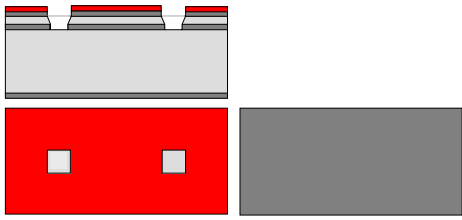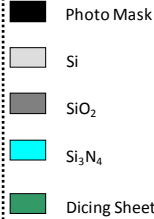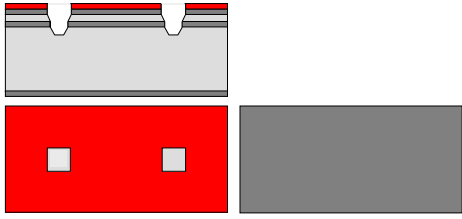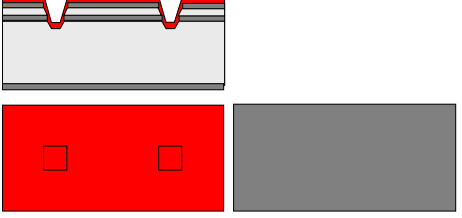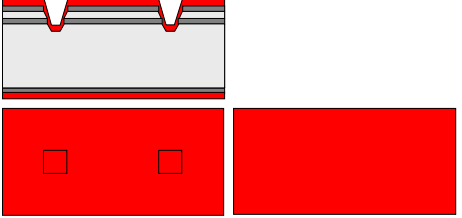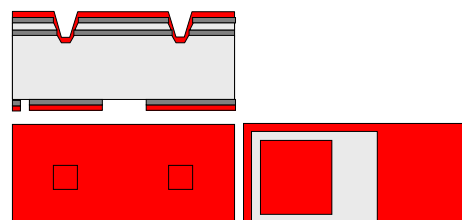
Process Name: Specimen for silicon nitride film
Name: HYUN-JIN OH   *Isono Lab.*

#	Process	Figure	Condition	Comment
3)	Photolithography		(1)Dehydration Bake in Oven -Temperature : 110℃ -Time : 10min (2) Spin coating of P.R. -P. R. : OFPR800 50cp -Rotation speed : 1st 500rpm 　　　　　　　　2nd 2500rpm -Time : 1st 5sec 　　　　2nd 25sec (3) Pre-Baking in Oven -Temperature : 90℃ -Time : 10min (4) Exposure -Alignment Gap : 100μm -Print Gap : 0μm -Time : 4sec (5) Development -TMAH2.38% NMD-3 -Time : 60sec -Pure Water Rinsing : 10min (6) Post-Baking in Oven -Temperature : 110℃ -Time : 50min	■ Photo Mask ▢ Si ▨ SiO₂ ▨ Si₃N₄ ▨ Dicing Sheet ■ Photoresist ■ Cr
4)	RIE for SiO₂ removal		-Etchant : CHF_3 -RF Power : 100 W (519) -Vaccum : 0.05 Torr -Flow Rate : 20 sccm -Etching Time : 20 min	
5)	Wet Etching for Si removal		-TMAH 20% -Temperature : 90℃ -Time : 20 min -Pure Water Rinsing : 30 min	
6)	Photolithography		(1)Dehydration Bake in Oven -Temperature : 110℃ -Time : 10min (2) Spin coating of P.R. -P. R. : OFPR800 50cp -Rotation speed : 1st 500rpm 　　　　　　　　2nd 2500rpm -Time : 1st 5sec 　　　　2nd 25sec (3) Pre-Baking in Oven -Temperature : 90℃ -Time : 10min (4) Exposure -Alignment Gap : 100μm -Print Gap : 0μm -Time : 4sec (5) Development -TMAH2.38% NMD-3 -Time : 60sec -Pure Water Rinsing : 10min (6) Post-Baking in Oven -Temperature : 110℃ -Time : 50min	

Fig. 2.2 Process chart of SiN*x*/SCS specimen (continued).

#	Process	Figure	Condition	Comment
7)	**Wet Etching for SiO₂ removal**		-Etchant : BHF 14% -Etching Time : 30min Pure Water Rinsing : 10min	■ Photo Mask □ Si ▨ SiO₂ ▨ Si₃N₄ ▨ Dicing Sheet ▨ Photoresist ▨ Cr
8)	**Wet Etching for Si removal**		TMAH 20% Temperature : 90℃ Time : 20min Pure Water Rinsing : 20 min	
9)	**Photolithography**		(1)Dehydration Bake in Oven -Temperature : 110℃ -Time : 10min (2) Spin coating of P.R. -P. R. : OFPR800 50cp -Rotation speed : 1st 500rpm 2nd 2500rpm -Time : 1st 5sec 2nd 25sec (3) Pre-Baking in Oven -Temperature : 90℃ -Time : 10min (4) Post-Baking in Oven -Temperature : 110℃ -Time : 50min	
10)	**Photolithography**		(1)Dehydration Bake in Oven -Temperature : 110℃ -Time : 10min (2) Spin coating of P.R. -P. R. : OFPR800 50cp -Rotation speed : 1st 500rpm 2nd 2500rpm -Time : 1st 5sec 2nd 25sec (3) Pre-Baking in Oven -Temperature : 90℃ -Time : 10min (4) Exposure -Alignment Gap : 100μm -Print Gap : 0μm -Time : 4sec (5) Development -TMAH2.38% NMD-3 -Time : 60sec -Pure Water Rinsing : 10min (6) Post-Baking in Oven -Temperature : 110℃ -Time : 50min	
11)	**Wet Etching for SiO₂ removal**		-Etchant : BHF 14% -Etching Time : 30min -Pure Water Rinsing : 30min	

Process Name: Specimen for silicon nitride film
Name: HYUN-JIN OH

Isono Lab.

Fig. 2.2 Process chart of SiNx/SCS specimen (continued).

#	Process	Figure	Condition	Comment
	Process Name: Specimen for silicon nitride film Name: HYUN-JIN OH			*Isono Lab.*
12)	**Wet Etching for Si removal**		-TMAH 20% -Temperature : 90℃ -Time : 11hr 30min -Pure Water Rinsing : 20 min	■ Photo Mask □ Si ■ SiO₂ (SiO_2) ■ Si₃N₄ (Si_3N_4) ■ Dicing Sheet
13)	**Wet Etching for SiO₂ removal**		-Etchant : BHF 14% -Etching Time : 30min -Pure Water Rinsing : 30min	■ Photoresist ■ Cr
14)	**Photolithography**		(1)Dehydration Bake in Oven -Temperature : 110℃ -Time : 10min (2) Spin coating of P.R. -P. R. : OFPR800 50cp -Rotation speed : 1st 500rpm 2nd 2500rpm -Time : 1st 5sec 2nd 25sec (3) Pre-Baking in Oven -Temperature : 90℃ -Time : 10min (4) Exposure -Alignment Gap : 100μm -Print Gap : 0μm -Time : 4sec (5) Development -TMAH2.38% NMD-3 -Time : 60sec -Pure Water Rinsing : 10min (6) Post-Baking in Oven -Temperature : 110℃ -Time : 50min	
15)	**ICP for Si removal**		-Etching Gas : SF₆ 130sccm (SF_6) -Passivation Gas : C₄F₈ 130sccm (C_4F_8) -RF Power : 200 W -RF Pressure : 0.20 torr	
16)	**Deposition of Si₃N₄** (Si_3N_4)			

Fig. 2.2 Process chart of SiN$_x$/SCS specimen.

of the specimen was oriented along the [110] direction in the (001) plane. The top and BOX layers of SiO_2 on the specimen were removed by hydrofluoric (HF) acid, and SiN_x thin film was deposited from the top surface of the specimen using two kinds of PE-CVD machines. Here, NH_3, SiH_4 and N_2 gases went around the backside of SCS layer, so the films were deposited at top and backside surfaces of the gauge section. Finally, a grid pattern made of photoresist was formed on the topside and at the center of the gauge section to measure longitudinal elongation with AFM during tensile loading.

Table 2.1 lists the deposition conditions for the SiN_x films and average dimensions of SiN_x /SCS specimens. Three samples of each kind of film were prepared (a total of 27 samples for S iN_x/SCS specimen). During the deposition, the gas flow ratios of SiH_4 to NH_3 to N_2 were set to be 1 : 1.5 : 281 (case 1) for the PE-CVD machine #1, 1 : 2.2 : 50 (case 2) and 1 : 5.0 : 169 (case 3) for the PE-CVD machine #2. RF powers, deposition temperatures and chamber pressures were 50 **W**, 523 **K** and 93 **Pa** for case 1, 20 **W**, 518 **K** and 90 **Pa** for case 2 and 40 **W**, 573 **K** and 90 **Pa** for case 3, listed in **Table 2.2**.

The film thickness was measured at the cross section of SiN_x/SCS specimens using a field-emission type scanning electron microscope (FE-SEM, HITACHI S-4800), as listed in **Table 2.3.** Here, SiN_x layer on the sidewall was not clearly observed in this research. Even if SiN_x were coated on the sidewall with the same thickness of the topside, the stress calculated from the

Table 2.1 Deposition parameters and nominal dimensions of specimens [unit: μm]

Specimen No.			Thickness		Width w	Length l
			SCS, t_1	SiN_x, t_2		
SiN$_x$ / SCS	CASE 1 (PE-CVD #1) Gas flow ratio NH$_3$/SiH$_4$: 1.5	A	9.52 ±0.1	0.14±0.1	290 ±5	3000 ±10
		B		0.38±0.1		
		C		0.69±0.1		
	CASE 2 (PE-CVD #2) Gas flow ratio NH$_3$/SiH$_4$: 2.2	A		0.14±0.1		
		B		0.38±0.1		
		C		0.69±0.1		
	CASE 3 (PE-CVD #2) Gas flow ratio NH$_3$/SiH$_4$: 5.0	A		0.14±0.1		
		B		0.38±0.1		
		C		0.68±0.1		

Table 2.2 Conditions of each part of specimen.

Specimen No.	CASE 1	CASE 2	CASE 3
Gas flow ratio of SiH$_4$ to NH$_3$ to N$_2$	1:1.5:281	1:2.2:50	1:5:169
RF Power (W)	50	20	40
Deposition temperature (K)	523	518	573
Chamber pressure (Pa)	93	90	90

Table 2.3 FE-SEM photographs of cross section of SiNx/SCS substrate.

cross sectional area would show only 4 to 5 % error. This research, then, neglected the existence of SiNx layer on the sidewall. All the deposition parameters were kept constant until the film thicknesses reached to around 0.15, 0.40 and 0.70 μm in the process. The film thickness on the backside of the specimen was about half of that on the topside because of the lower deposition rate on the backside. Nine kinds of SiNx films were prepared for tensile tests, and only specimens having dimensional tolerances within ±5 % of all dimensions were used in the tests.

Uniaxial tensile tests were performed using a compact tensile tester built into the commer-

cial AFM (Seiko Instruments Inc., NPX100), as shown in **Fig. 2.3 (a-b)**. The tensile tester composed of a piezoelectric actuator, actuator case, load cell, linear variable displacement transducer (LVDT), and specimen holders, as shown in **Fig. 2.3 (c-d)**, is set under the AFM head, and is installed in a shield box on a vibration absorption system. The load cell and LVDT, having resolutions of 0.38 μN and 10 nm, respectively, measure the tensile force and relative displacement between the specimen holders. **Fig. 2.4 (a)** shows the AFM image of the resist grid pattern fabricated on the topside of the gauge section for SiN_x/SCS specimen. AFM can observe the profile of the grid pattern under the tensile loading. The grid pattern consists of four lines with a width of 20 μm and a height of 200 nm, which are parallelized at a pitch of 45 μm shown in **Fig. 2.4 (b)**. The distance between the left side edge of the first line and the right side edge of the fourth line (155 μm in the design) is defined as the gauge length of the SiN_x/SCS specimens and the change of the gauge length is measured by AFM during tensile loading as the longitudinal elongation. By comparing the grid pattern profile measured before tensile loading with that after tensile loading as the left side edge of the first line is set as the origin in the x-axis, the elongation is measured from the difference in the position of the right side edge in the fourth line between before and after tensile loading (See, **Fig. 2.4 (c)**). The AFM image of the pattern has pixels of 512 x 512 at the observation area of 200 μm x 200 μm, so one pixel represents 0.391 μm. The pixel size is very large as a resolution for longitudinal elongation in the 135 μm gauge length. In this research, Boltzmann function has been used to compensate the AFM data to improve the measurement resolution of elongation. After fitting the AFM data by the function, elongation was calculated from the changes of intersections between the grid profile line and the horizontal line of 100 nm in the z-direction, as also shown in **Fig. 2.4 (d)**. This method enabled us to evaluate Young's modulus of the micron scale SCS specimen with very small deviation within 0.1 % from the analytical value based on anisotropic theory in the previous work [12].
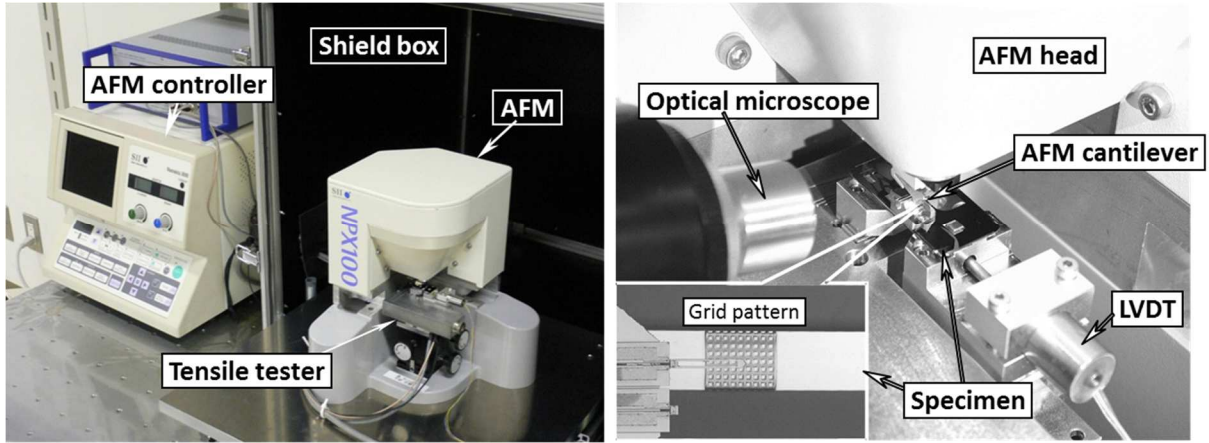
(a) Micro-scale tensile tester built in AFM

(b) Close-up view of tensile tester
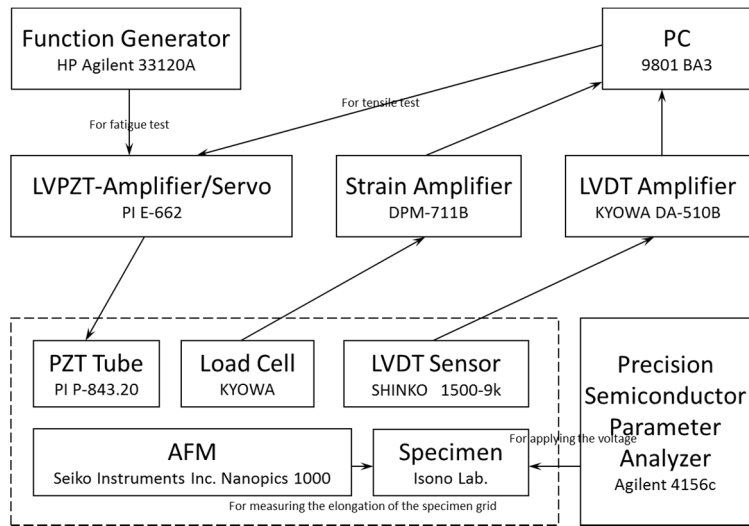
(c) Experimental model of tensile test
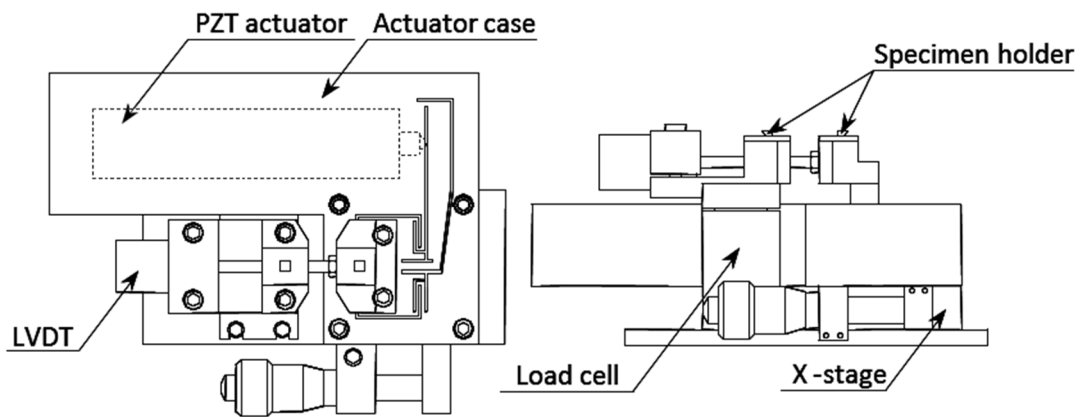
(d) Schematic of AFM tensile tester

Fig. 2.3 Schematic and photographs of the tensile tester operating with AFM.

3 4

(a)

(c)

Grid pattern profile

Position z

Before loading
$e = 0$

After loading
$e \neq 0$

0   Position x

20μm 25μm

200 nm

0   [μm]   167.5862

A view of A-A` section

(b)

250

Boltzmann function fittings

$$z = \frac{A - B}{1 + \exp\left(\dfrac{x - x_0}{dx}\right)} + B$$

200

$e_x = 0.11\ \%$

$e_x = 0.15\ \%$

150

$e_x = 0.19\ \%$

$z = 100\ nm$

$e_x = 0\ \%$

100

$e_x = 0.035\ \%$

50

$e_x = 0.076\ \%$

0

169   169.5   170   170.5   171   171.5

x-position, μm

z-position, nm

(d)
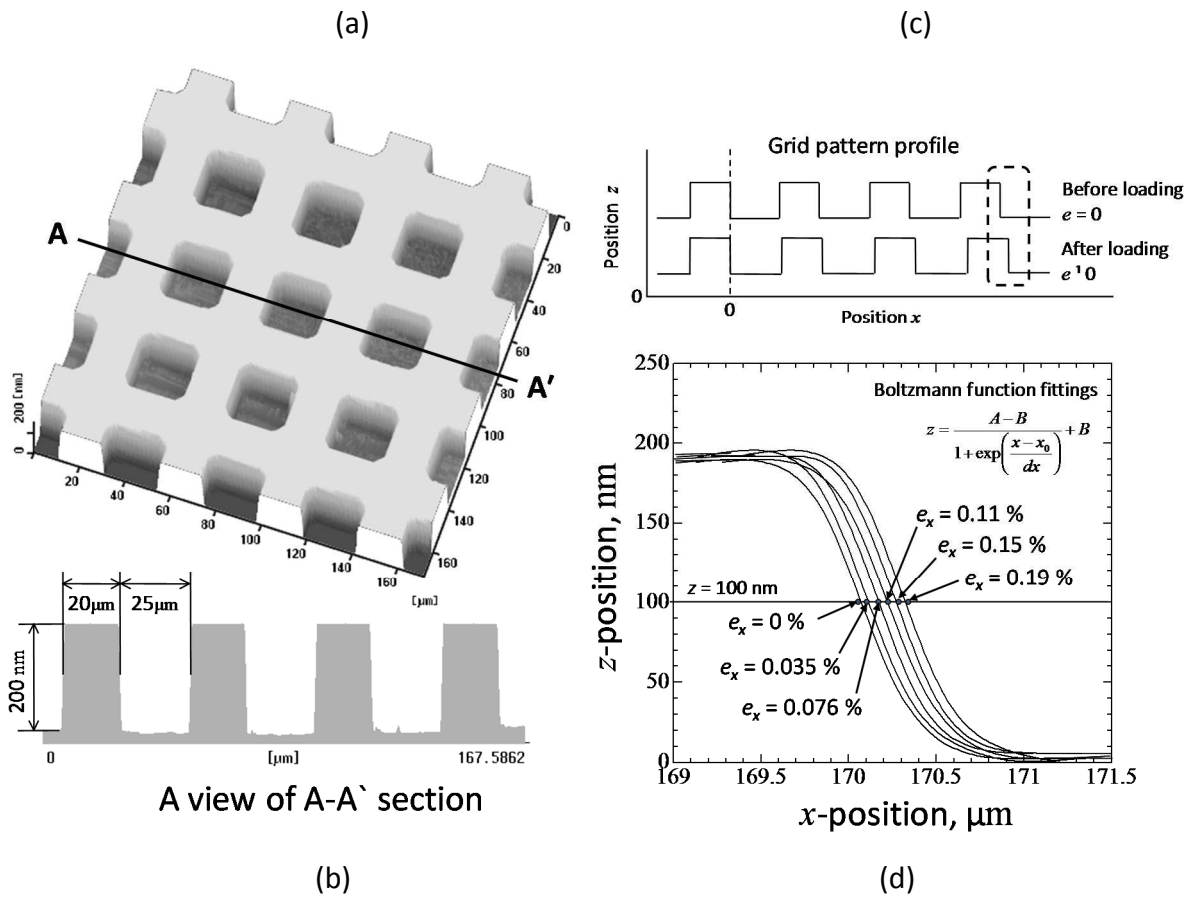
Fig. 2.4 3D (a) and sectional (b) AFM images of a grid pattern on the tensile specimen, (c) change of the gauge pattern profile with increasing tensile load, and (d) Boltzmann functions to improve the resolution.

3 5

2.3   Evaluation Techniques of Mechanical Properties for PE-CVD SiNx Film

Young's modulus of submicron SiNx/SCS substrates can be estimated from the effective elastic modulus, E_{1+2}, of SiNx/SCS laminated specimens. The longitudinal strain of the SiNx film can be regarded as being equal to that of the SCS substrate in **Fig. 2.5**, because of the fixed boundary condition of SiNx and SCS layers, without due consideration of difference in Poisson's ratio between the film and substrate. Then, E_{1+2} is roughly given by:

$$E_{1+2} = \frac{t_1 E_1 + t_2 E_2}{t_1 + t_2} \qquad\qquad (2.1)$$

where, E is Young's modulus, t is thickness, and the subscripts 1 and 2 indicate SCS substrate and SiNx film, respectively. Even if Poisson's ratio of the film takes into account the calculation of Young's modulus, E_2, of the film, uncertainty of only 5 to 6 % is produced in the calculation [12]. For simple and easy evaluation of Young's modulus of the film, **Eq. (2.1)** was used in this research.

To estimate E_2 using **Eq. (2.1)**, the film thickness, t_2, and the effective elastic modulus, E_{1+2}, have to be measured precisely. The film thickness, t_2, is not a topside of but a sum of both side of SiNx film, described in the **Fig. 2.5**. The value can be measured precisely with a calibration of dimensional measurement using a commercial sample of line patterns with a regular interval inside the FE-SEM. Even if 10 % error was produced in the measurement of thickness from the real value, E_2 calculated from **Eq. (2.1)** would have only uncertainty less than 5 % for the samples used here. The effective elastic modulus, E_{1+2}, was derived from the gradient of stress-strain curve, where the gradient was calculated by the least squares method. The least squares method and the data fitting of AFM image in **Fig. 2.4** make a fine measurement of E_{1+2}, so that E_2 can be precisely determined by **Eq. (2.1)** regardless of the small value of $t_2/(t_1+t_2)$ [12].

To evaluate Poisson's ratio of SiNx film, a nano-indentation test was performed in addition to the tensile test. The nano-indentation test is able to directly measure the reduced modulus,
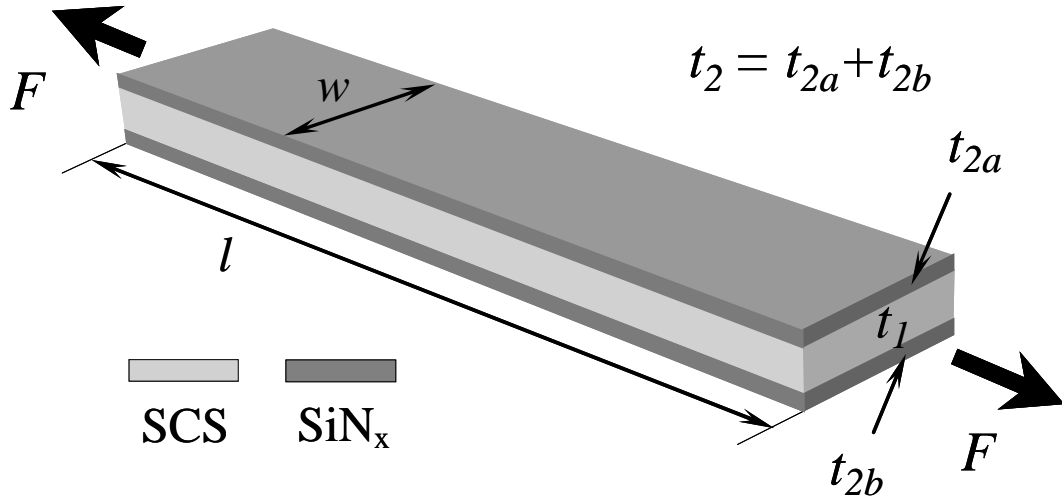
Fig. 2.5 Schematic of SiNx/SCS laminated specimen for tensile test. The thickness of SiNx film, t_2, is composed of the top and back side film layer.

E_r, from the unloading stiffness in the load-penetration depth curve. The indentation tests for 2 μm SiNx films coated on 400 μm SCS substrate were carried out on a basis of the theory proposed by W. C. Oliver *et al.* [13]. The unloading stiffness, S, corresponding to the slope of the unloading curve is expressed as:

$$\frac{1}{S} = C_f + \frac{\sqrt{\pi}}{2E_r} \frac{1}{\sqrt{A}} \tag{2.2}$$

where C_f is the compliance of the load frame in the nano-indentation tester, and A is the contact area between the film and the indenter. C_f needs to be calibrated before the indentation test. E_r can also be expressed as the sum of the plane-strain moduli of the SiNx film and an indenter:

$$\frac{1}{E_r} = \frac{1-v_2^2}{E_2} + \frac{1-v_i^2}{E_i} \tag{2.3}$$

where v_2 is Poisson's ratio of the SiNx film, and E_i and v_i are Young's modulus and Poisson's ratio of a diamond indenter used in the test, respectively. The plane-strain modulus of the indenter, $(1-v_i^2)/E_i$, in **Eq. (2.3)** was calibrated by indentation test using a material having known mechanical properties. If E_r is determined experimentally, v_2 can be calculated by applying E_2

and $(1-v_i^2)/E_i$ into **Eq. (2.3)**.

In the nano-indentation test using a thin film deposited on a substrate, the maximum penetration depth should be ordinarily set to be less than 1/10 of the film thickness in order to exclude the influence of elastic deformation of the substrate on the load-penetration depth curve of the film [13]. We carried out indentation tests with a commercial indentation tester (ELIONIX^{TM}, ENT-1100a) at the maximum penetration depth ranging from 0.05 to 0.14 μm, indicating that the maximum depths were within the range from 1/40 to 7/100 times on 2 μm Si Nx film.

2.4   Results of AFM Tensile Testing

Fig. 2.6 shows typical tensile stress-strain curves of SiNx/SCS specimens deposited with NH$_3$-to-SiH$_4$ ratios of (a) 1.5 (PE-CVD machine #1), (b) 2.2 (PE-CVD machine #2) and (c) 5.0 (PE-CVD machine #2). The longitudinal strain of closed plots is directly measured by the AFM. The solid lines are drawn using the strain estimated from the relative displacement between specimen holders by LVDT, where the displacement has been simultaneously corrected by the finite element analysis (FEA) in **Fig. 2.7**. This is because the longitudinal elongation at the gauge section was analyzed to be 0.58 times the displacement applied to the entire specimen due to the strain distribution on the x-y plane of specimen. Initial loads in **Fig. 2.6** was applied before all tensile tests to remove the gap between the square holes of specimen and the specimen holders. If the gap exists, the relative displacement between two specimen holders measured by LVDT is different from the entire elongation of specimen. The friction force between the grip areas of specimen and the specimen holders will also be generated.

All the SiNx/SCS specimens have shown a linear stress-strain relation and failed in a brittle manner. Effective elastic moduli, $E_{1+2}{}^{LVDT}$, of SiNx/SCS specimens estimated by LVDT are each lower than those by AFM. A narrow gap between the specimen and holder could have under estimated the elastic moduli in LVDT measurement even after correction by FEA. Therefore, the AFM direct tracing for elongation on the gauge section is appropriate for accurate evaluation of elastic modulus in this paper. Effective elastic moduli, $E_{1+2}{}^{AFM}$, of the SiNx/SCS specimens calculated by AFM are 166.57, 166.41 and 167.93 GPa, for case 1, 2 and 3, respectively. Substituting $E_{1+2}{}^{AFM}$, E_1, t_1 and t_2 into **Eq. (2.1)**, Young's moduli, E_2, of the SiNx films are calculated to be 109.7, 104.0 and 143.6 GPa, respectively.

Fig. 2.8 shows a typical load-penetration depth curve obtained in the nano-indentation test using the 2 μm SiNx film. Applied load was set from 4.41 to 6.37 μN, so that the penetration depth was less than 0.2 μm. The reduced modulus, E_r, was calculated from the tangential line of unloading curve using **Eq. (2.3)**. **Table 2.4** summarizes averaged mechanical properties obtained from AFM tensile and nano-indentation tests, as average value of three specimens in each deposition condition. Young's moduli for only SiNx films, E_2, obtained from tensile tests were approximately 3.2 to 5.6 % higher than reduced moduli, E_r, because of the plane-strain

modulus of the indenter, $(1-\nu_i^2)/E_i$. Poisson's ratios, ν_2, of the SiNx films, calculated by **Eq. (2.3)**, are in the range of 0.19 to 0.27.
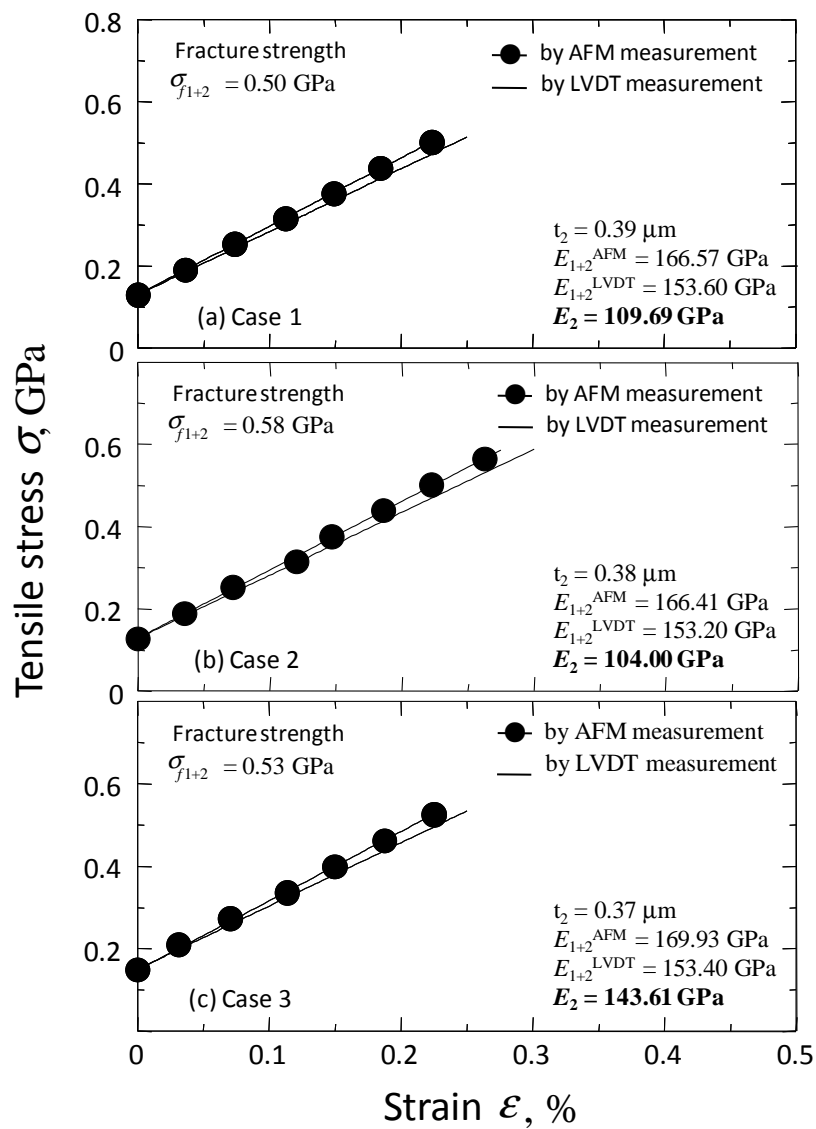
Fig. 2.6 Typical stress-strain curves of SiNx/SCS laminated specimens. The gas flow ratio of NH$_3$ to SiH$_4$ during deposition were (a) 1.5, (b) 2.2, (c) 5.0.
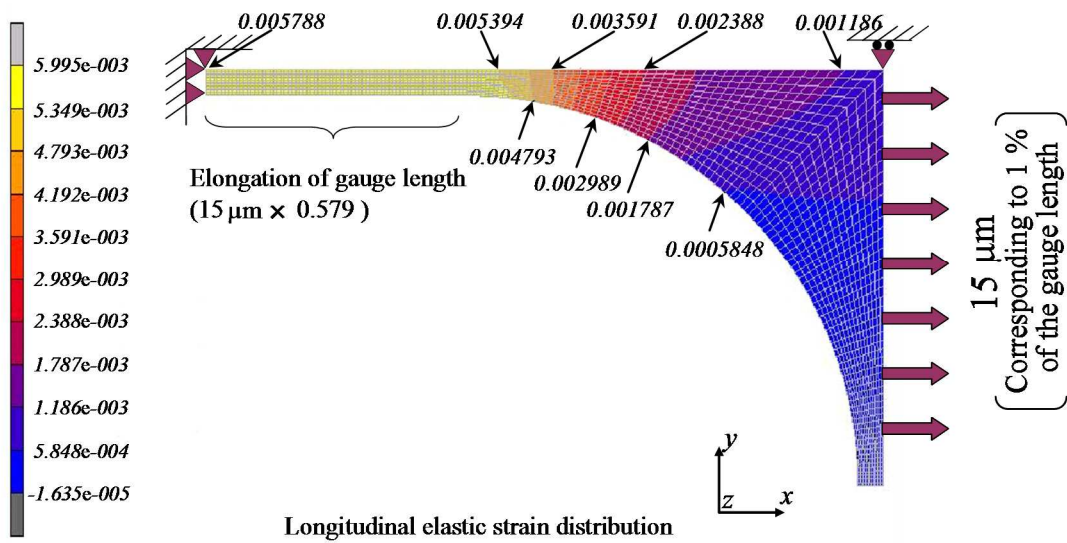
Fig. 2.7 Longitudinal elastic strain distribution obtained by FEA under application of the 1 % elongation of the gauge length to the entire specimen model.
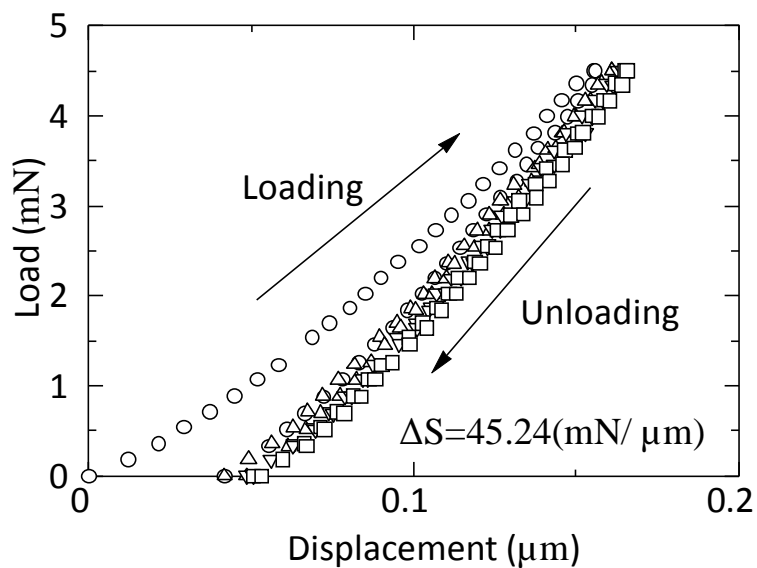
Fig. 2.8 Typical load vs. penetration depth curves of the SiN$_x$/SCS specimen.

Table 2.4 Summary of the mechanical properties for SCS and SiNx thin films.

Specimen group			Thickness		AFM tensile test		
			SiNx	SCS	Resultant modulus of specimen	Young's modulus of SiNx film	Fracture strength of specimen
			t_2 [μm]	t_1 [μm]	E_{1+2}^{AFM} [GPa]	E_2 [GPa]	$\sigma_{f\,1+2}$ [GPa]
SiNx/ SCS	Case 1	A	0.14	9.52	168.053	109.0	0.54
		B	0.38	9.52	166.576	108.9	0.44
		C	0.69	9.52	164.936	109.8	0.41
	Case 2	A	0.14	9.50	167.968	103.0	0.70
		B	0.38	9.51	166.376	103.2	0.43
		C	0.69	9.52	164.275	99.52	0.40
	Case 3	A	0.14	9.51	168.527	143.2	0.46
		B	0.38	9.52	167.896	142.5	0.48
		C	0.68	9.52	167.245	144.3	0.32

Specimen group			AFM tensile + Nano-indentation test	Nano-indentation test
			Poisson's ratio of SiNx film	Reduced modulus
			v_2	E_r [GPa]
SiNx/ SCS	Case 1	A	0.25	
		B	0.26	105.83
		C	0.24	
	Case 2	A	0.19	
		B	0.19	97.96
		C	0.27	
	Case 3	A	0.25	
		B	0.27	135.65
		C	0.25	

2.5 Mechanical Properties of PE-CVD SiNx Films Deposited at Several Gas Flow Ratios

Fig. 2.9(a) depicts Young's moduli of SiNx films as a function of film thickness. Young's moduli of SiNx film deposited at each NH$_3$-to-SiH$_4$ ratio are independent of film thickness, with average value of 109.2, 102.6 and 143.2 **GPa**, for case 1, 2 and 3, respectively. These are comparable to PE-CVD SiNx films in previous works, listed in **Table 2.5 [11, 16-20]**. Young's moduli of PE-CVD SiNx films listed are ranging of 97 to 221 **GPa**. Since deposition conditions such as gas flow ratio, substrate temperature, electric discharge power and vacuum condition are different one another, Young's moduli would have varied widely. Sputtered SiNx film also has a similar value to PE-CVD films, but SiNx films deposited by the LP-CVD in **Table 2.5** exhibit higher moduli ranging of 202 to 370 **GPa**. LP-CVD SiNx film coated at a high temperature has minimal hydrogen present in the films, whereas hydrogen atoms are easily incorporated into PE-CVD SiNx films because of a low deposition temperature **[21, 22]**. The LP-CVD SiNx films would have resulted in larger Young's modulus due to a lower incorporation of hydrogen atoms.

On the assumption that Poisson's ratio of SiNx films has no correlation with the film thickness, as well as the Young's moduli, this research has also estimated Poisson's ratio from **Eq. (2.3)** using the reduced moduli obtained from 2 μm SiNx films. **Fig. 2.9 (b)** shows Poisson's ratios of SiNx films at each film thickness. Poisson's ratios estimated by SiNx films with thicknesses about 0.14 μm are scattered in a wide range of 0.13 to 0.37. But, the data scatter decreases with an increase of the film thickness. This is because standard deviations of Young's modulus, E_2, used in **Eq. (2.3)** are inversely proportional to the film thickness. For example, the deviations are found to be 3.02, 1.76 and 0.25, for 0.14, 0.38 and 0.69 μm films in case 1, respectively. The wide scatter of Poisson's ratio in the thinner films has been directly affected by the scatter of E_2.

Fig. 2.9 (c) correlates the fracture strength of SiNx/SCS specimens with film thickness. The fracture strength is inversely proportional to the film thickness at each specimen group, with a scattering of several data. The maximum fracture strength was about 0.72 **GPa**, which was smaller than that of 10 μm SCS specimen **[12]**. This might be caused by a crack initiation and propagation of the SiNx films at the top surface, inside, or the film-substrate interface. The SiN

x films would have fractured first, and the substrates broken immediately due to the impact of the film breaking. However, the essence of fracture behavior in the SiN*x*/SCS specimens cannot be concluded until further observations have been performed.
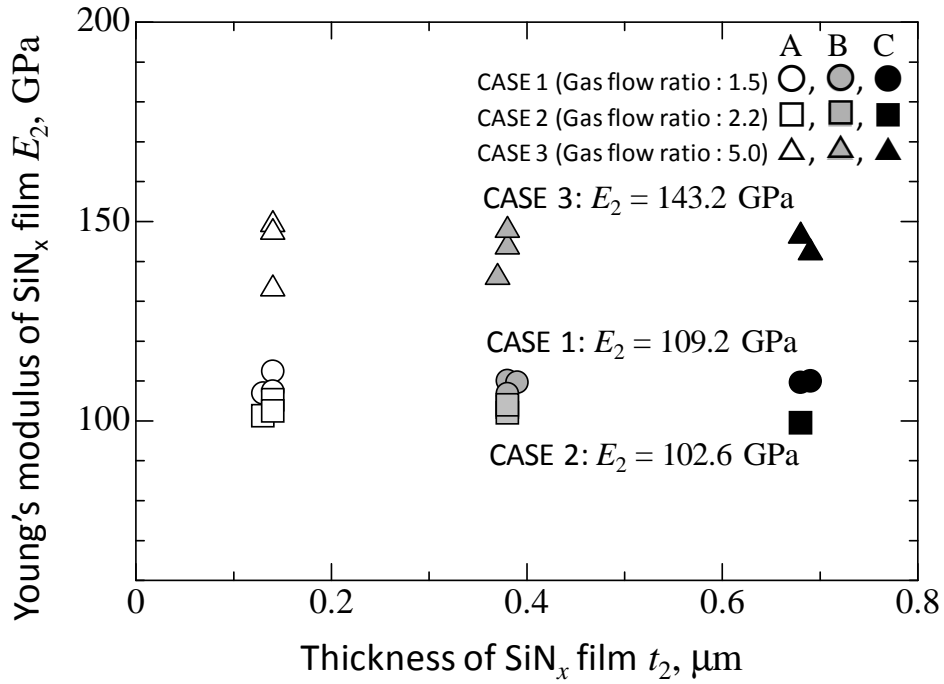
(a) Young's modulus vs. thickness
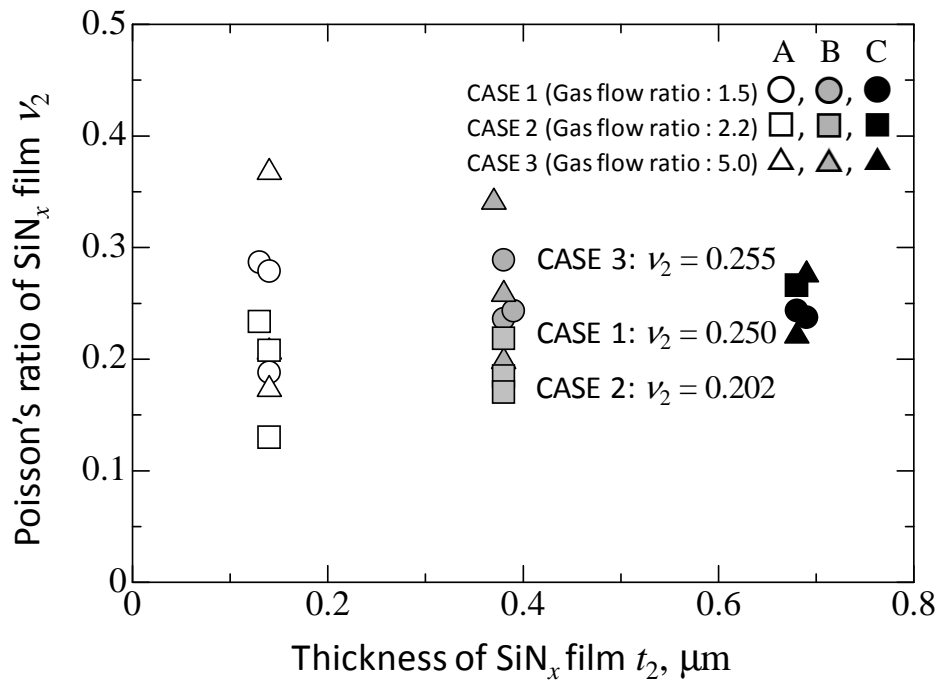
(b) Poisson's ratio vs. thickness
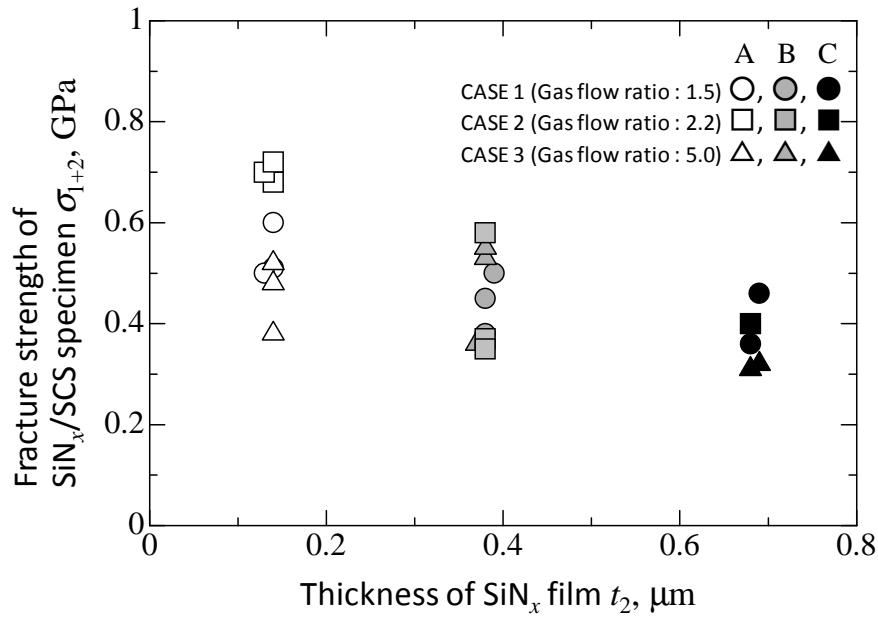
(c) Fracture strength vs. thickness

Fig. 2.9 (a) Young's modulus, (b) Poisson's ratio and (c) Fracture strength vs. film thickness for the SiN$_x$/SCS specimens prepared under the different gas flow ratios. Lines in (a) show the average of Young's modulus at each gas flow ratio.

Table 2.5 Literature value of SiN$_x$ material properties.

Reference	Year Published	Coating Method	Test Method	Young's moulus E (GPa)	Film Thickness t (nm)	Depositon Temp. (°C)
C. T. Lynch [15]	-	Crystal	-	317	-	-
M. Vila *et al.* [5]	2003	Sputtered	Indentation	100~210	-	(1750)
O. Tabata *et al.* [3]	1989	LP-CVD	Membrane	290	200	790
Tetsuo Yoshioka *et al.* [6]	2000	LP-CVD	Tension	370	100	750
T.Y. Zhang *et al.* [7]	2000	LP-CVD	Tension	202.57±15.80	760	840
D.M.Profunser *et al.* [10]	2004	LP-CVD	BAW *	260	520	700
Yeon-Gil Jung *et al.* [16]	2004	LP-CVD	Indentation	266±4	50~1500	830
R.L. Edwards *et al.* [8]	2004	LP-CVD	Tension	257	500	-
Wen-Hsien Chuang *et al.* [9]	2004	LP-CVD	Bending	260.5	450	-
O. Tabata *et al.* [3]	1989	PE-CVD	Membrane	210	500	300
J. Ashley Taylor [1]	1991	PE-CVD	Indentation	178~221 **	-	400
Torsten Kramer *et al.* [17]	2002	PE-CVD	Bulge	150±7	1900	300
Torsten Kramer *et al.* [11]	2003	PE-CVD	Bulge	160	500	300
Yeon-Gil Jung *et al.* [16]	2004	PE-CVD	Indentation	119±3	500	100
H Huang *et al.* [18]	2005	PE-CVD	Indentation	97±1.6	300~1200	125
This work	**2005**	**PE-CVD**	**Tension**	**102.6~143.2**	**100~700**	**-**

* BAW : bulk acoustic waves   ** values were calculated from the equation of E/(lv^2)

4 5

2.6   Effect of Film Composition on Elastic Properties

The gas flow ratio of NH_3 to SiH_4 in PE-CVD will determine the film composition of $SiNx$, which can affect its mechanical properties. In this research, Auger spectroscopy investigates atomic content of the $SiNx$ films in order to reveal the effect of the film composition on mechanical properties. **Fig. 2.10** shows typical Auger spectra of the $SiNx$ films deposited with NH_3-to-SiH_4 ratios of 1.5 (CASE 1), 2.2 (CASE 2) and 5.0 (CASE 3). The $SiNx$ films are found to mainly contain atoms of N, Si, O, and C. Hydrogen atom is also probably contained in the films, but Auger spectroscopy cannot detect it because of the light atomic weight. Auger spectra have two obvious peaks corresponding to N and Si atoms. This indicates that N and Si are the dominant atoms as compared with other atoms. The N-to-Si ratio equivalent to the peak intensity ratio is calculated to be 1.11, 0.96 and 1.15 for cases 1, 2 and 3, respectively. Although the atomic content ratio (N-to-Si ratio) of case 1 is expected to be the minimum from the viewpoint of gas flow ratio (NH_3-to-SiH_4 ratio), the N-to-Si ratio of case 2 is smaller than that of case 1. This is because the PE-CVD machines used are different in case 1 and 2; therefore, the atomic content ratio doesn't always directly relate to the gas flow ratio during deposition.
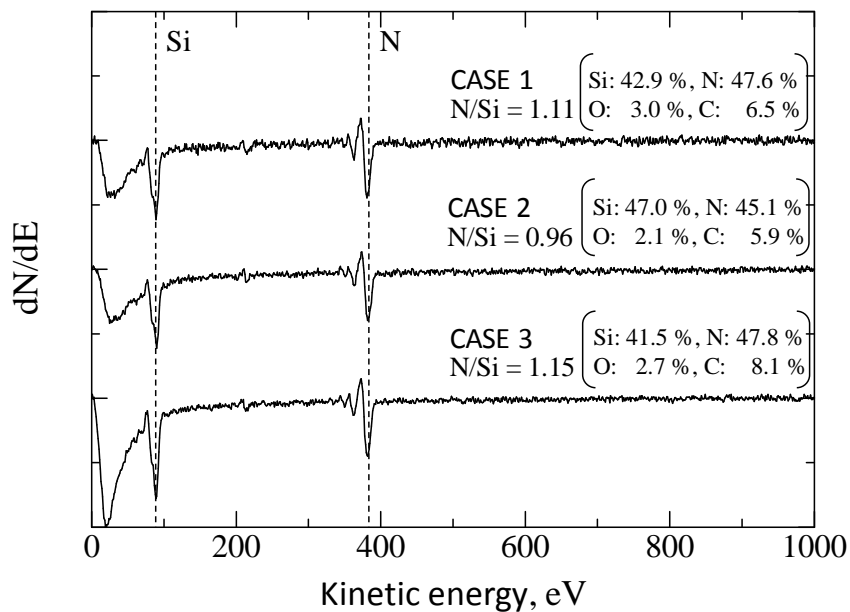
Fig. 2.10 Typical Auger spectra of $SiNx$ films.
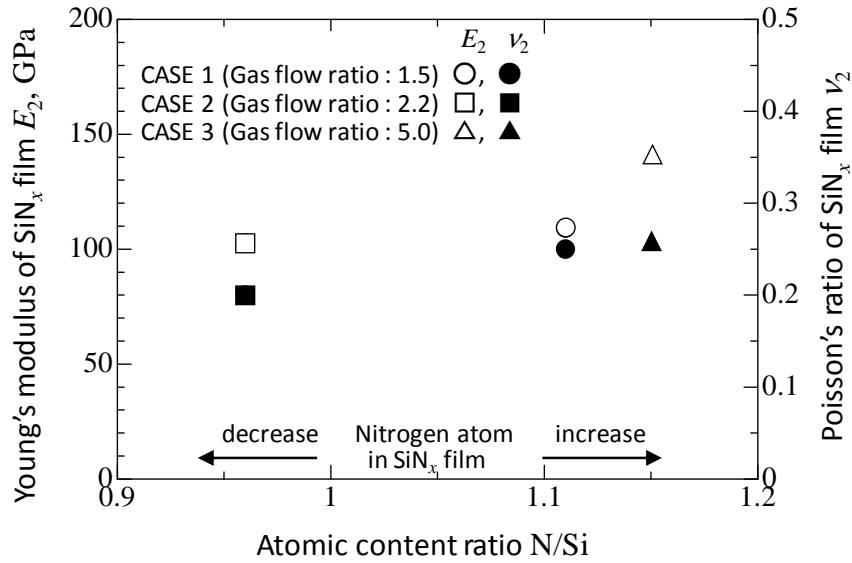
Fig. 2.11 Young's modulus and Poisson's ratio of SiNx films
as a function of the atomic content ratio.

Fig. 2.11 relates Young's modulus and Poisson's ratio with the atomic content ratio. Young's modulus and Poisson's ratio of the SiNx films increase with an increase of the atomic content ratio. An estimate of elastic properties for the SiNx films is possible based on the atomic content ratio rather than the gas flow ratio, even if different PE-CVD machines deposit the films. The variation of elastic properties with increasing the atomic content ratio shows a tendency to reach into poly-crystalline Si_3N_4, since Young's modulus and Poisson's ratio of Si_3N_4 are about 317 **GPa** and 0.27 at the atomic content ratio of 1.33 **[14]**. The gas flow rate of NH_3 and SiH_4, which can lead to the atomic content ratio of 1.33, should be employed in PE-CVD to deposit S iNx films with higher elastic constants.

2.7   Conclusions

In this research, submicron PE-CVD SiN_x films were characterized using the handmade uni-axial tensile tester built in AFM, in order to examine the influence of the gas flow ratio of NH_3 to SiH_4 on the elastic properties. The nano-indentation tests were also carried out for the estimation of Poisson's ratio for the SiN_x films. The AFM tensile tester accurately measured effective elastic modulus of SiN_x/SCS specimens, and we have succeeded in separating Young's modulus for only PE-CVD SiN_x films. Young's modulus ranged from 99.5 to 149.3 **GPa**, which were lower than that of LP-CVD SiN_x films due to low process temperature. Poisson's ratio of the films was also estimated as 0.13 to 0.37 from reduced modulus. The elastic properties of PE-CVD SiN_x films were greatly influenced by the gas flow ratio of NH_3 to SiH_4, regardless with film thickness. Fracture strength of the SiN_x/SCS specimens had in the range of 0.31 to 0.72 **GPa**, which is decreased with increasing film thickness. Auger spectroscopy was employed to reveal the film composition of the PE-CVD SiN_x films. Nitrogen and silicon atoms were dominant, contained more than 90 % in the films. Young's modulus and Poisson's ratio of the SiN_x films correlated with the atomic content ratio rather than the gas flow ratio. The SiN_x films with an atomic content ratio being close to that in crystalline Si_3N_4 yielded higher elastic constants.

References

[1] A.S. Ergun, Y. Huang, X. Zhuang, O. Oralkan, G.G. Yaraloiglu, and B.T. Khuri-Yakub: Capacitive Micromachined Ultrasonic Transducers: Fabrication Technology, *IEEE Transactions of Ultrasonics, Ferroelectrics, and Frequency control*, vol. 52, no. 12, pp. 2242-2258, 2005.

[2] A. Trautmann, P. Ruther, and O. Paul: Microneedle arrays fabricated using suspended etch mask technology combined with fluidic through wafer vias, *IEEE The 16th Annual International Conference on Micro Electro Mechanical Systems, Kyoto*, pp. 682–685, 2003.

[3] E. Sarajlic, M. J. de Boer, H. V. Jansen, N. Arnal, M. Puech, G. Krijnen, and M. Elwenspoek: Advanced plasma processing combined with trench isolation technology for fabrication and fast prototyping of high aspect ratio MEMS in standard silicon wafers, *Journal of Micromechanics and Microengineering*, vol. 14, pp. S70-S75, 2004.

[4] Y. Xu, C.W. Chiu, F. Jiang, Q. Lin, and Y.C. Tai: A MEMS multi-sensor chip for gas flow sensing, *Sensors and Actuators A*, vol. 121, pp. 253-261, 2004.

[5] M. Villa, D. Caceres, and C. Prieto: Mechanical properties of sputtered silicon nitride thin films, *Journal of Applied Physics*, vol. 94, no. 12, pp. 7868-7873, 2003.

[6] T. Yoshioka, T. Ando, M. Shikida, and K. Sato: Tensile testing of SiO2 and Si3N4 films carried out on a silicon chip, *Sensors and Actuators A*, vol. 82, pp. 291-296, 2000.

[7] T.Y. Zhang, Y.J. Su, C.F. Qian, M.H. Zhao, and L.Q. Chen: Microbridge testing of silicon nitride thin films deposited on silicon wafers, *Acta Materialia*, vol. 48, pp. 2843-2857, 2000.

[8] R.L. Edwards, G. Coles, and W.N. Sharpe: Comparison of tensile and bulge tests for thin-film silicon nitride, *Experimental Mechanics*, vol. 44, no. 1, pp. 49-54, 2004.

[9] W.H. Chuang, T. Luger, R.K. Fettig, and R. Ghodssi: Mechanical Property Characterization of LPCVD Silicon Nitride Thin Films at Cryogenic Temperatures, *Journal of Micromechanics and Microengineering*, vol. 13, no. 5, pp. 870-879, 2004.

[10] D.M. Profunser, J. Vollmann, and J. Dual: Determination of the material properties of microstructures by laser based ultrasound, *Ultrasonics*, vol. 42, pp. 641-646, 2004.

[11] T. Kramer and O. Paul: Mechanical properties of compressively prestressed thin films extracted from pressure dependent ripple profiles of long membranes, *Proc. of MEMS 2003 Kyoto, IEEE the sixteenth annual international conference*, pp. 678-681, 2003.

[12] Y. Isono, T. Namaze, and N. Terayama: Development of AFM Tensile Test Technique for Evaluating Mechanical Properties of Sub-Micron Thick DLC Films, *Journal of Microelectromechanical Systems*, vol.15, no.1, pp.169-180, 2006.

[13] W.C. Oliver and G.M. Pharr: An improved technique for determining hardness and elastic modulus using load and displacement sensing indentation experiments, *Journal of Materials Research*, vol. 7, no. 6, pp. 1564-1583, 1992.

[14] J.D.J. Ross, H.M. Pollock, J.C. Privin, and J. Takadoum: Limits to the hardness testing of films thinner than 1μm, *Thin Solid Films*, vol. 148, no. 2, pp. 171-180, 1987.

[15] C.T. Lynch: Practical Handbook of Materials Science, p. 321, 1989.

[16] Y.G. Jung, B.R. Lawn, M. Martyniuk, H. Huang, and X.Z. Hu: Evaluation of elastic modulus and hardness of thin films by nano-indentation, *Journal of Materials Research*, vol. 19, No. 10, pp. 3076-3080, 2004.

[17] T. Kramer and O. Paul: Postbuckled micromachined square membranes under differential pressure, *Journal of Micromechanics and Microengineering.*, vol. 12, pp. 475-478, 2002.

[18] H. Huang, K. Winchester, Y. Liu, X.Z. Hu, and C.A. Musca: Determination of mechanical properties of PECVD silicon nitride thin films for tunable MEMS Fabry-Perot optical filters, *Journal of Micromechanics and Microengineering*, vol. 15, pp. 608-614, 2005.

[19] J.A. Taylor: The mechanical properties and microstructure of plasma enhanced chemical vapor deposited silicon nitride thin films, *Journal of Vacuum Science & Technology A*, vol. 9, no.4, pp. 2464-2468, 1991.

[20] O. Tabata, K. Kawahata, S. Sugiyama, and I. Igarashi: Mechanical Property Measurements

of Thin Films Using Load-Deflection of Composite Rectangular Membranes, *Sensors and Actuators*, vol. 20, pp. 135-141, 1989.

[21] A. Stoffel, A Kovacs, W. Kronast, and B. Muller: LPCVD against PECVD for micromechanical applications, *Journal of Micromechanics and Microengineering*, vol. 6, pp. 1-13, 1996.

[22] J. Yota, J. Hander, and A.A. Saleh: A comparative study on inductively-coupled plasma high-density plasma, plasma-enhanced, and low pressure chemical vapor deposition silicon nitride films, *Journal of Vacuum Science & Technology A*, vol. 18, pp. 372-376, 2000.

Chapter 3

Strain Rate Dependence of Mechanical Properties for Sub 100 nm-Thick Au Film Using EANAT

3.1 Introduction

Focuses on the material properties depend on the actual situations of their use. Au thin films have been used in electronic industries typically as wires on the devices for electric circuits. Hence, the use of Au thin films is ubiquitous in the broad range of applications. Although Au itself is not intrinsically a new material, mechanical properties of materials generally depend on the fabrication processes as they define the microscopic structures. Conventional fabrication of the metallic wires on the substrate has been either thermal evaporation or sputtering process. Recent advances in the technologies related to micro- and nano-electromechanical systems (MEMS/NEMS) have provided new opportunities for the miniaturization of not only the mechanically moving part of MEMS/NEMS themselves but also the electronic circuits. In particular, the novel method, called "nano-transfer printing (n-TP)", has been developed [1-5]. In this method, the patterns of wires of Au films are printed on the substrate to be used for devices. The film thickness of Au in the devices can be less than 100 nm. The consequence of applied stress in the contact process of n-TP needs to be clarified for the full industrial use. The fundamental understanding based on the materials mechanics is necessary to enable the prediction essential for device design. Furthermore, the tolerance of loading conditions in n-TP while in use is of primary importance in order to ensure the device performance and reliability. The wide-spread method for the mechanical characterization at device design stages is the numerical analysis based on the continuum mechanics such as finite element method (FEM). This is now part of the ordinary procedure of industrial designing due to the relatively good cost performance. However, the reliability of such analysis is obviously affected by the precision of basic material properties used as the input parameters, which are obtained from direct measurements in the experiments. Once the basic mechanical properties are determined, it becomes feasible to predict the mechanical properties affected by the specific situations of n-TP.

Therefore, the direct measurement on the mechanical properties of sub-100-nm Au films

is important for the reliable applications of n-TP. The question is how to test the specimens with such an extremely small size. Although the basic concept is the same as macroscopic tensile tests, the mechanical characterization of sub-100-nm specimen accompanies difficulties to overcome. First, the fixation of specimen needs high precision. Second, the preloading before the test has to be avoided. Third, the magnitude of the applied load and the resolution of load and displacement have to be small enough. In this study, we have measured the tensile properties of the Au thin films with the thickness of sub-100-nm regime. In the previous study, we developed the tensile testing system based on the MEMS technology. Here, we have modified the design of our system, fabricated the device, and realized the tensile tests of such Au thin films. In our system, the specimen is fabricated during the device fabrication process. This all-in-one fabrication does not require the specimen fixation procedure, and enables the high precision in the specimen alignment direction. It also circumvents the possible preloading in the specimen fixation. The electrostatic actuation provides the fine tuning of the applied load, and the high resolution of the displacement is realized by the lever motion amplification mechanism. We show the results of tensile tests and discuss the obtained mechanical properties with an emphasis on the impact of material fabrication process.

3.2   Specimen Preparation and AFM Based Tensile Testing System

The schematic of our tensile testing device is shown in **Fig. 3.1**. The device consists of the specimen part, actuator part, and measurement part. The specimen part consists of the specimen of Au thin film in the form of the doubly-clamped beam. The actuator part consists of the comb drive actuators that are electrostatically actuated. The number of comb drive actuators can be roughly calculated and determined by the cross section of specimen. The actuator part is not in contact with the specimen part at the neutral position, *i.e.*, without the applied voltage for the test. They are in contact with each other after the 4 μm displacement (d_s) of the actuator part (**Fig. 3.1**). This gap avoids the preloading of specimen before loading for tensile test. The measurement part consists of the lever-motion amplification system, where the displacement caused by the specimen elongation is amplified to realize the measurement of high resolution. The actuator part and the measurement part have a 3 μm gap between each other (d_m) (**Fig. 3.1**). This gap is designed to be smaller than that between the actuator part and specimen part in order to ensure that the displacement of the actuator part first causes the contact with the measurement part and subsequently with the specimen part, thereby the displacement of the measurement part captures the specimen elongation from the beginning of the tensile loading on it. During the fabrication process, dry etching method by ICP-RIE was used to etch the silicon comb drive and measurement parts. In theory, dry etching direction is perpendicular to the plasma, however, the condition is not always ideal. So in case of **Fig. 3.1**, when actuator part contacts measurement part, it is more likely to be a point contact instead of a line contact. In this case the measurement part will be impacted the substrate by torsion, eventually stiction can arise in the lower applied voltage rather than the designed voltage. Therefore, this led to the nonzero displacements in the direction perpendicular to the tensile direction. In this study, we re-designed the symmetric configuration to avoid this problem and improved the precision of the measurement. Here, two cantilevers play a role of geometric amplification system for a deflection of the doubly-clamped beam, where the cantilevers are symmetrically placed on the doubly-clamped beam at the distance of $L/4$ from its fixed ends since the bending moment of the doubly-clamped beam at the $L/4$ is 0. All of the movable components of specimen, actuator, and measurement parts are supported by the beams, and the mechanical contributions in the

tensile tests is considered and calibrated. In our system, the displacements were monitored by optical microscope (Olympus Co., SZX12) coupled to a charge coupled device (CCD) camera (Hitachi, KP-F120CL). The resolution of the CCD camera was 6.45 μm/pixel and had 1392 × 1040 pixels. The maximum frame rate was 30 fps. The block matching and linear compensation method was used for the image analysis, which improves the resolution 25 times from the CCD [8, 9]. In combination with these setups, we use the lever-motion amplification at the measurement part shown in **Fig. 3.2 (a)**. The amplification factor of the system was calculated from Euler-Bernoulli equation and FEA. **Fig. 3.2 (b)** shows the equivalent strain distribution of the doubly-clamped beam, when the displacement of 1 μm in the y-direction is given at the point A in the figure. The equivalent strain at the point B was not produced practically since the moment at the $L/4$ from the fixed end is 0, which can guarantee the face angle of the cantilevers are kept at 90 degree against the face of the doubly-clamped beam at the $L/4$. **Table 3.1** lists the coordinates of the point A, B, and C shown in **Fig. 3.2 (b)** before and after the deflection of
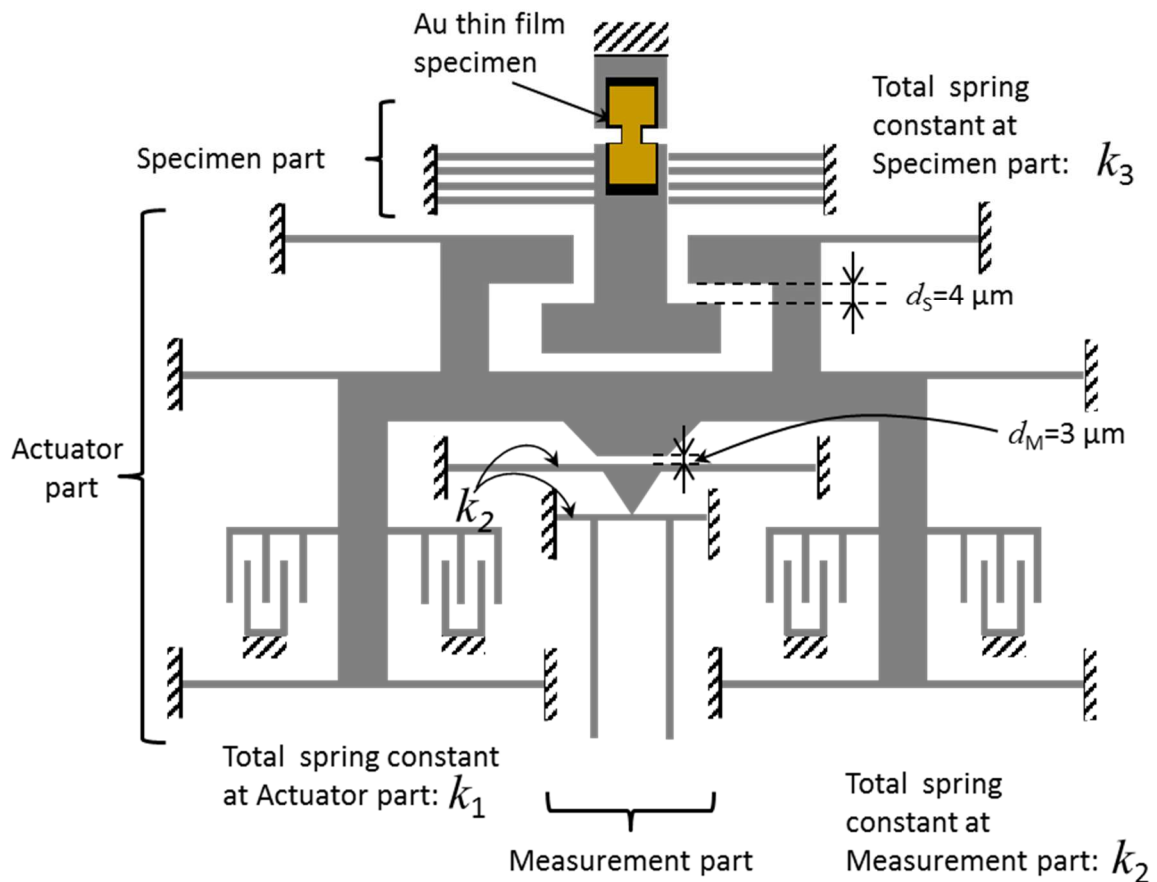
Fig. 3.1 Schematic diagram of the MEMS-based tensile testing device.

5 5

the doubly-clamped beam, which were calculated from the linear elastic deformation theory and FEA. The differences in the coordinates between the linear elastic theory and FEA are very small at each point, although the x-coordinate of the point C was underestimated from FEA with 0.1 % error. Thus, this research employs 20.1 as an amplification factor of the actuator displacement from the FEA. Consequently, the total resolution in the displacement of our system reached 0.65 nm.

The device fabrication was realized by the typical techniques used in MEMS, which is based on the semiconductor processing (**Fig. 3.3**). The device was fabricated from a SOI wafer (100) consisting of 400 μm of substrate, 3 μm of BOX, and 35 μm of active layer. First, thermal oxidation

$$D \cong d \times 20.1$$
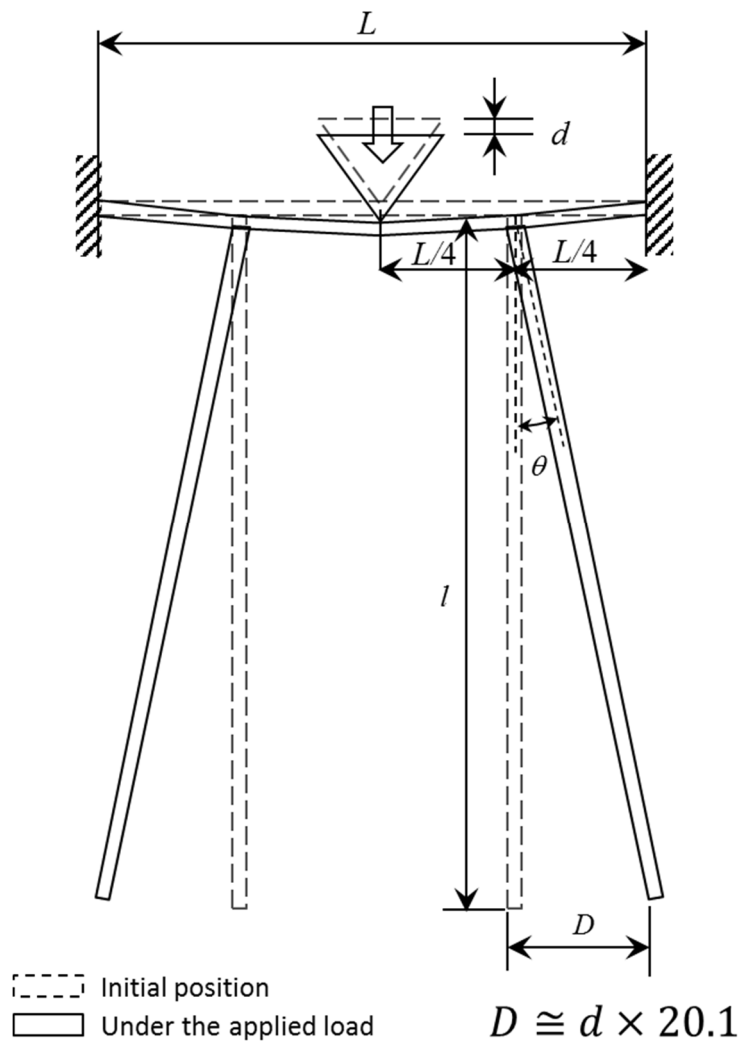
(a) Schematic of the lever-motion amplification system at the measurement part.
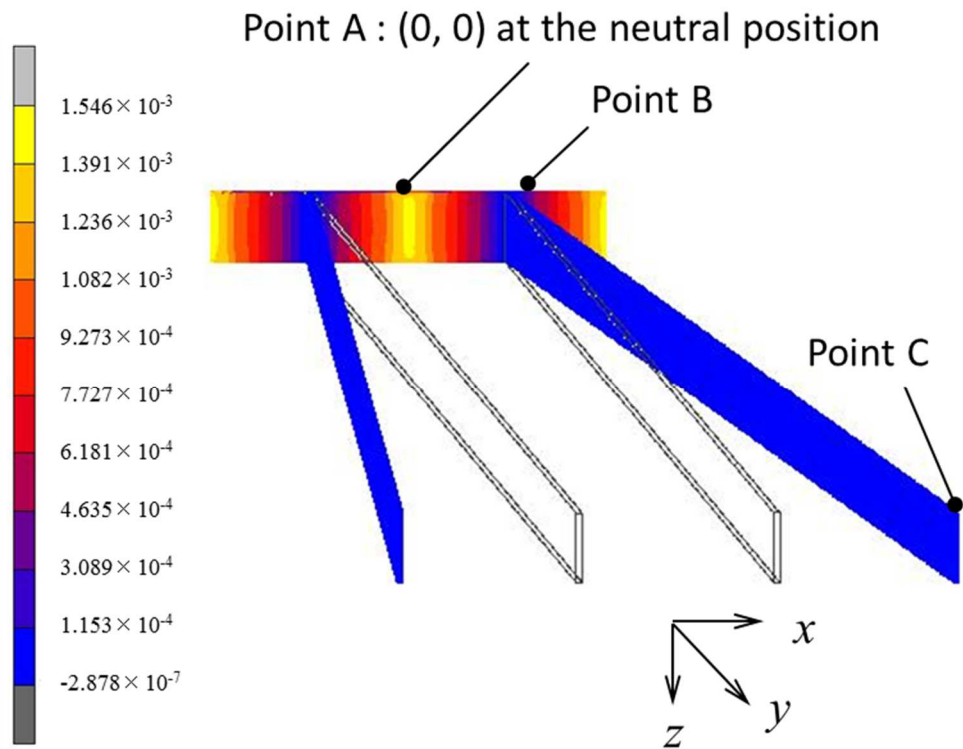
(b) Equivalent strain distribution of doubly-clamped beam calculated from FEA.

Fig. 3.2 Schematic of the lever-motion amplification system used for the magnification of the actuator displacement. Specification of l = 2000 mm and L = 300 mm leads to the 20.1 times of amplification factor.

Table 3.1 Coordinates at Point A, B and C of the measurement part, when the displacement of 1 μm is applied to Point A.

	Neutral coordinates, (x, y), without displacement	Coordinates after the deflection of beam (the linear elastic theory)	Coordinates after the deflection of beam (FEA)
Point A	(0, 0)	(0, 1)	(0, 1)
Point B	(75, 0)	(75, 0.5)	(75.015, 0.5000)
Point C	(75, 2000)	(95, 2000.5)	(95.097, 2000.5)

layer with a thickness of 800 nm was grown on the top. Then, Cr was deposited on the SiO_2 layer of the substrate by the thermal evaporation as a seed layer for Au film. The measured thickness of Cr layer was 3 nm at most. This Cr layer was removed by O_2 plasma treatment method which inductively coupled plasma reactive ion etching (ICP-RIE) later, not by wet etching method because of the high risk of breakdown of Au specimen. The 15-nm-thick Au layer was deposited on the Cr layer using the same apparatus using an Au wire with a volume of 1.96 mm^3, and the 70-nm-thick Au thin film was continuously fabricated by the RF-sputtering process for 25 seconds, which becomes the major part of the Au film specimen. The specimen shape was patterned by the photolithography. The comb structures of the actuator part and cantilever structure of the measurement part were also fabricated with photolithography after the deposition of Cr film by thermal evaporation. This Cr film also played a good role as a protective film of Au specimen. The Cr was etched by the wet process after the photoresist patterning. In order to make the suspended structure of the specimen part, the silicon on the bottom side of the substrate was removed by the ICP-RIE after the masking with Cr and Al films for the irrelevant part by photolithography. Finally, the SiO_2 layers of the top and bottom surfaces and the BOX layer were removed by vapor HF. This process makes the comb drive structure movable by the input of voltage.

Process number

 # 01 Specification for silicon on insulator (SOI) wafer

Figure

A-A cross-section

Top view

Bottom view
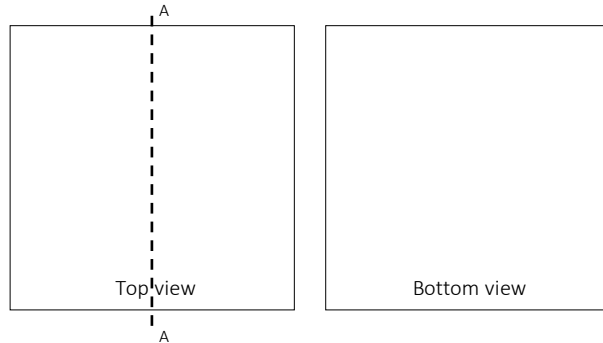
Condition

[Specification of Wafer]
• Diameter : 100 mm (4 inch) , 150 mm (6 inch)
• The thickness of active layer : 35 µm (4 inch, 6 inch)
• The thickness of Buried Oxide(BOX) layer : 3 µm (4 inch), 2 µm (6 inch)
• The thickness of Substrate : 400 µm (4 inch, 6 inch)
• Total thickness : 438 µm (4 inch), 439 µm (6 inch)
• Dopant : Phosphorus (Type : P)

Process number

 # 02 SOI wafer cutting (Half size)

Figure

Condition

(1) Dehydration bake on a hot-plate
    5 min @ 110 ºC
(2) Spin coating of photoresist (OFPR800 23 or 54cp)
    Rotation speed & time
    1st : 5 sec @ 500 rpm
    2nd : 30 sec @ 3000 rpm
(3) Bake on a hot-plate
    10 min @ 110 ºC
(4) Adhere a dicing sheet to the reverse side of SOI wafer
    Thickness : 80 µm

(5) Cut SOI wafer
    Blade speed : 5.0 mm/s
(6) Rinse in acetone : 10 min (two times)
(7) Rinse in ethyl alcohol : 10 min
(8) Rinse in pure water : 10 min

◯ Si   🔵 SiO2   🟠 Cr   🔴 P.R.   ⚪ Al   🟡 Au

Fig. 3.3 Schematic diagram of the device fabrication process (continued).

Process number

03 SOI wafer cleaning

Figure
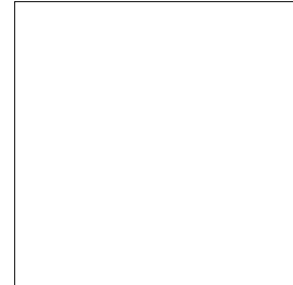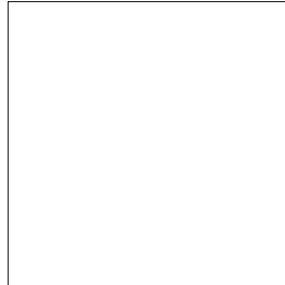
Condition

(1) SPM cleaning : 5 min
$H_2SO_4 : H_2O_2 = 2 : 1$
(2) Pure wafer rinse : 10 min
(3) APM cleaning : 5 min @ 110 ºC (hotplate temp.)
$NH_3 : H_2O_2 : H_2O = 1 : 1 : 5 \sim 1 : 1 : 10$
(4) Pure wafer rinse : 10 min
(5) HPM cleaning : 5 min @ 110 ºC (hotplate temp.)
$HCl : H_2O_2 : H_2O = 1 : 1 : 5 \sim 1 : 1 : 10$
(6) Pure wafer rinse : 10 min
(7) BHF etching : 10 sec (etching speed : 1 nm / sec)
(8) Pure wafer rinse : 10 min

Process number

04 Wet oxidation on SOI wafer

Figure

Condition

[Conditions of oxidation]
- Time : 6 hours
- Oxidation furnace temperature : 1000 deg.
- Estimated thickness : about 800 nm
- Gas flow of oxide gas : 1.2 liter/min
- steamed water temperature : 90 deg. (measured using a thermometer)

◯ Si   🔵 SiO2   🟠 Cr   🔴 P.R.   ⚪ Al   🟡 Au

Fig. 3.3 Schematic diagram of the device fabrication process (continued).

Process number

05 Chromium (Cr) & gold (Au) thin film deposition

Figure
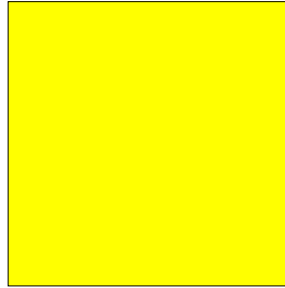
Condition

(1) Chromium deposition
    Time : 60 sec
    Pressure : 1.0×10^{-3} Pa
    Current : 65 A
    Estimated thickness : 10 nm
(2) Gold deposition
    Time : 120 sec
    diameter = 0.5 mm & length = 10 mm
    Pressure : 1.0×10^{-3} Pa
    Current : 65 A
    Estimated thickness : 15 nm

Process number

06 Gold sputtering

Figure
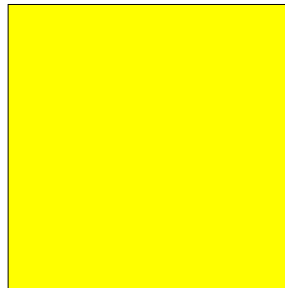
Condition

(1) Gold sputtering
    Time : 25 sec
    Pressure : 0.8 Pa
    RF Power : 150 W
    Estimated thickness : about 50 nm

Measure the thickness of chromium & gold layer by AFM
The thickness of each chromium & gold layer should be below 15nm & 80nm

◯ Si   🔵 SiO2   🟠 Cr   🔴 P.R.   ⚪ Al   🟡 Au

Fig. 3.3 Schematic diagram of the device fabrication process (continued).

Process number

07 Photolithography (1st)

Figure

Condition

(1) Dehydration bake in the oven
    5 min @ 110 ºC
(2) Spin coating of OAP
    Rotation speed & time
    1st : 5 sec @ 1000 rpm
    2nd : 30 sec @ 5000 rpm
(3) Bake for drying OAP in the oven
    3 min @ 110 ºC
(4) Spin coating of Photoresist (OFPR800 23cp)
    Rotation speed & time
    1st : 5 sec @ 1000 rpm
    2nd : 30 sec @ 5000 rpm

(5) Pre-bake in the oven
    2 min @ 110 ºC
(6) Exposure
    Time : 1.8 sec
(7) Development (TMAH 2.38% NMD-3)
    Time : 30~40 min
(8) Pure wafer rinse : 10 min
(9) Post-bake on a hot-plate
    10 min @ 110 ºC

Process number

08 Wet gold thin film etching & photoresist removal

Figure
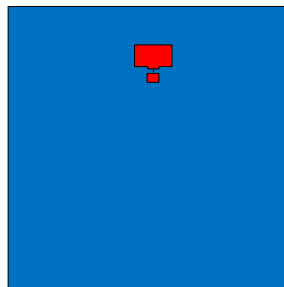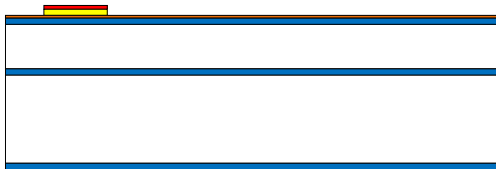
Condition

(1) Gold thin film etching (using new gold etchant)
    Time : ~ **2 min.**
    depending on the thickness of gold layer
(2) Pure wafer rinse : 10 min
(3) Photoresist removal (remover 104)
    5 min @ 110 ºC (hotplate temp.)
(4) Pure wafer rinse : 10 min
(5) Check the unnecessary gold layers by optical microscopy. And
    totally remove the gold layers.

○ Si   ● SiO2   ● Cr   ● P.R.   ● Al   ● Au

Fig. 3.3 Schematic diagram of the device fabrication process (continued).

Process number

09 SPM cleaning

Figure
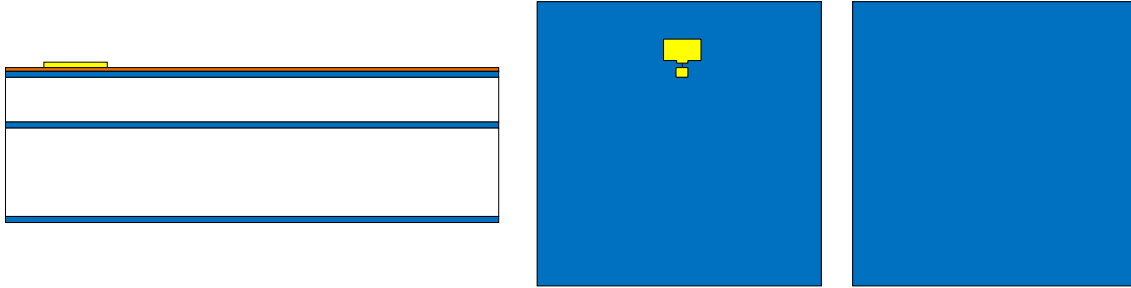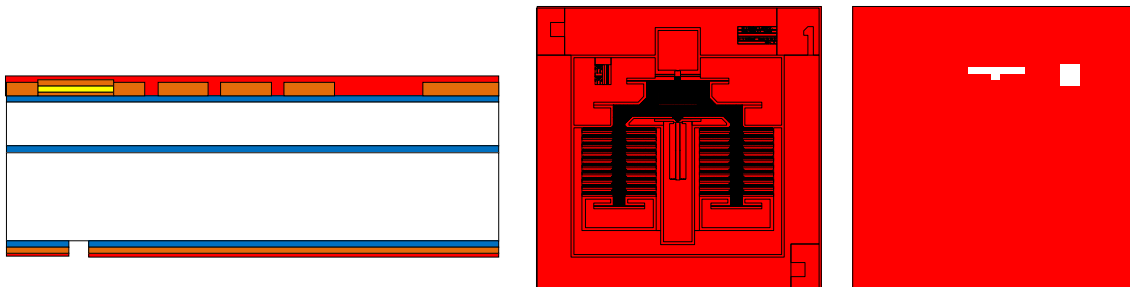

Condition

(1) SPM cleaning : 5 min
$H_2SO_4 : H_2O_2 = 2 : 1 \sim 4 : 1$
(2) Pure wafer rinse : 10 min

Process number

10 Chromium thin film deposition

Figure
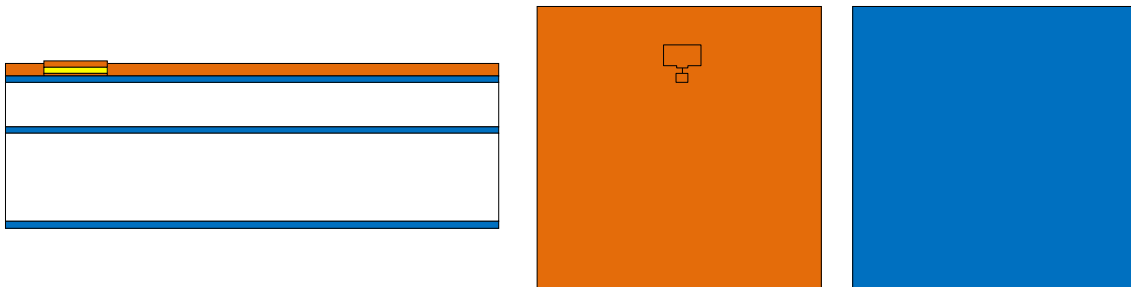
Condition

(1) Deposition of Chromium : **3 min**
Pressure : 1.0×10^{-3} Pa
Current : 65 A

Measure the thickness of chromium layer by AFM
Chromium layer should be below 10 nm

| ◯ Si | 🔵 SiO2 | 🟧 Cr | 🔴 P.R. | ⚪ Al | 🟡 Au |

Fig. 3.3 Schematic diagram of the device fabrication process (continued).

Process number

11 Photolithography (2nd)

Figure

Condition

(1) Dehydration bake in the oven
    5 min @ 110 ºC
(2) Spin coating of OAP
    Rotation speed & time
    1st : 5 sec @ 1000 rpm
    2nd : 30 sec @ 5000 rpm
(3) Bake for drying OAP in the oven
    3 min @ 110 ºC
(4) Spin coating of Photoresist (OFPR800 23cp)
    Rotation speed & time
    1st : 5 sec @ 1000 rpm
    2nd : 30 sec @ 5000 rpm

(5) Pre-bake in the oven
    2 min @ 110 ºC
(6) Exposure
    Time : 1.8 sec
(7) Development (TMAH 2.38% NMD-3)
    Time : 30~40 min
(8) Pure wafer rinse : 10 min
(9) Post-bake on a hot-plate
    10 min @ 110 ºC

Process number

12 Wet Chromium thin film etching

Figure
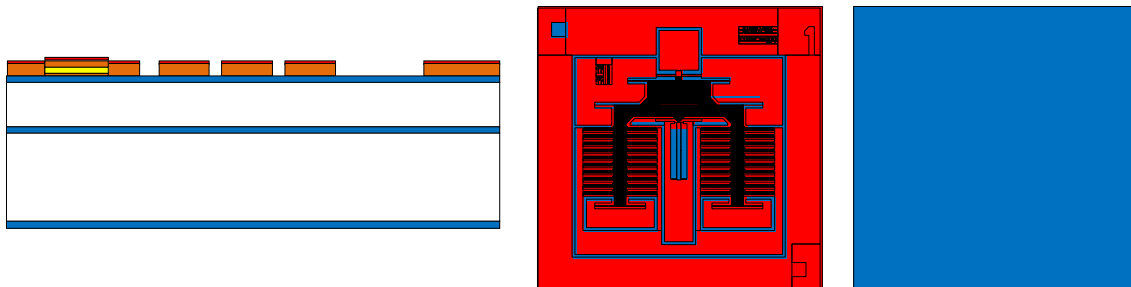
Condition

(1) Cooling the specimens for 2 ~ 3 hours
(2) Chromium etching (Chromium etchant)
    Time : 30 ~ 60 sec.
(3) Pure wafer rinse : 10 min

○ Si   ● SiO2   ● Cr   ● P.R.   ● Al   ● Au

Fig. 3.3 Schematic diagram of the device fabrication process (continued).

Process number

13 Photoresist removal & SPM cleaning
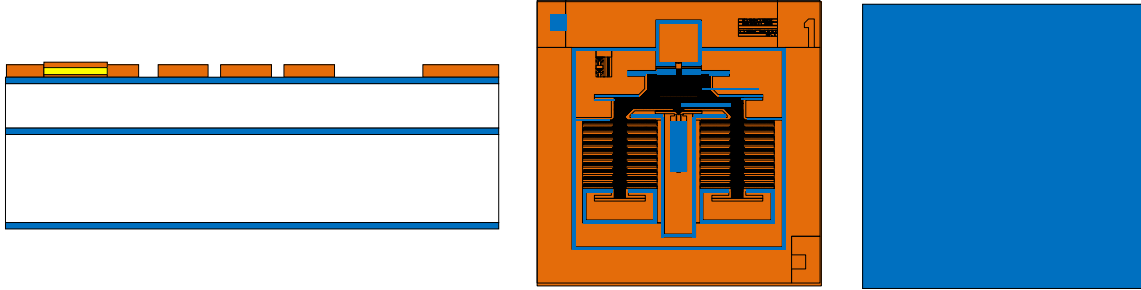
Figure
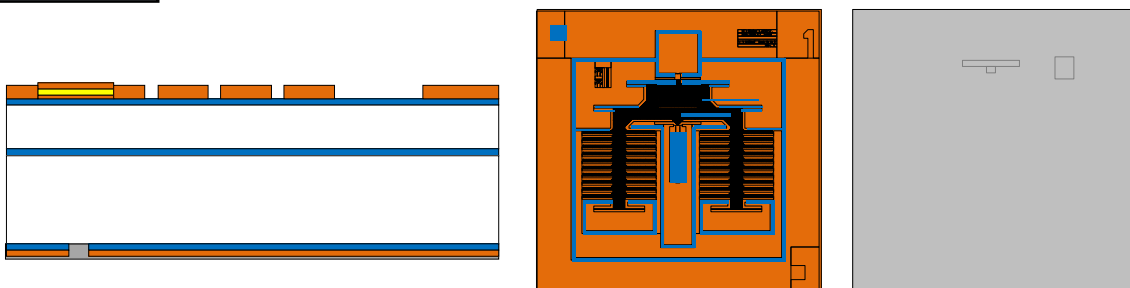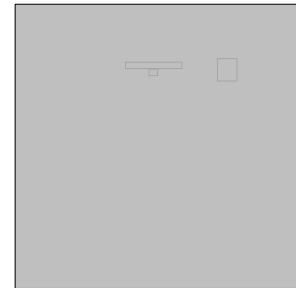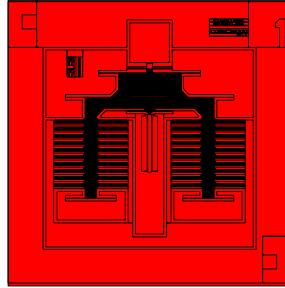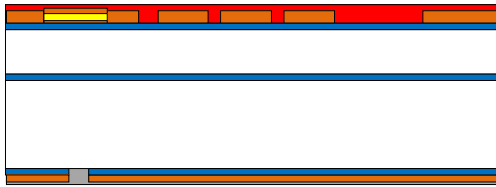

Condition

(1) Photoresist removal (remover 104)
    5 min @ 110 ºC (hotplate temp.)
(2) Pure wafer rinse : 10 min
(3) SPM cleaning : 10 min
(4) Pure wafer rinse : 10 min

Process number

14 Deposition of Chromium thin film

Figure
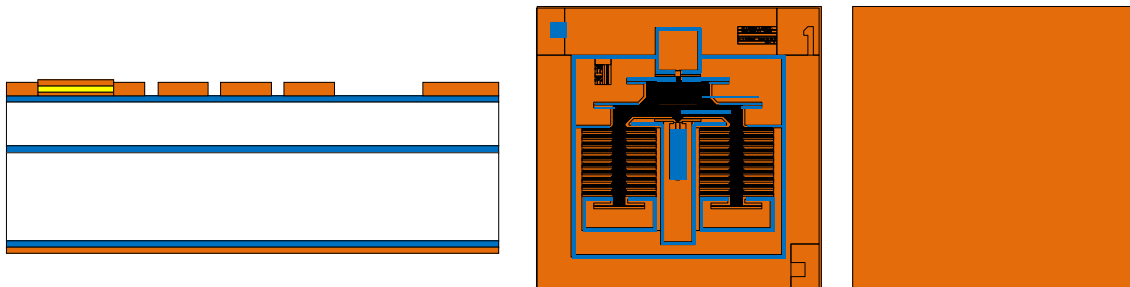
Condition

(1) Deposition of Chromium : 10 min
    Pressure : 1.0×10^{-3} Pa
    Current : 65 A

○ Si   ● SiO2   ● Cr   ● P.R.   ● Al   ● Au

Fig. 3.3 Schematic diagram of the device fabrication process (continued).

Process number

15 Coating P.R. for protecting the comb drivers
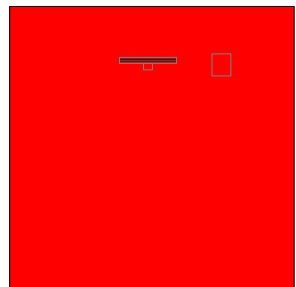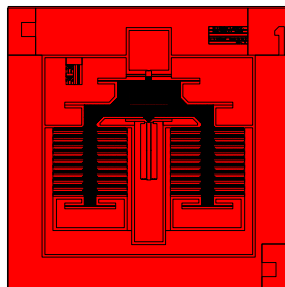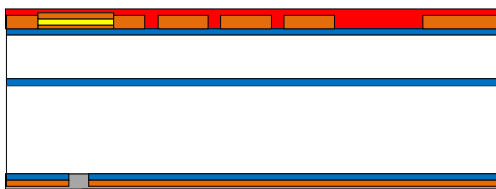
Figure
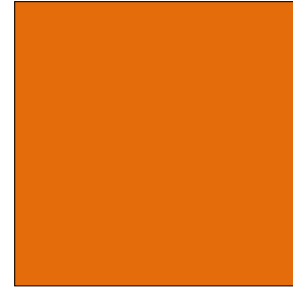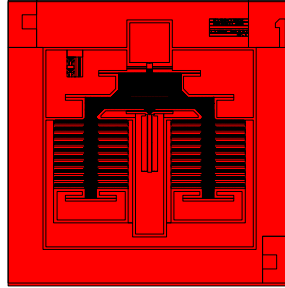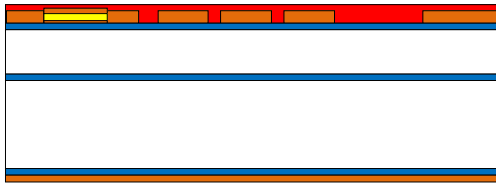
Condition

(1) Dehydration bake on a hot-plate
    5 min @ 110 ºC
(2) Spin coating of photoresist (OFPR800 23cp) – **without using OAP**
    Rotation speed & time
    1st : 5 sec @ 1000 rpm
    2nd : 30 sec @ **3000 rpm**
(3) Post-bake on a hot-plate : 10 min @ 110 ºC

Process number

16 Photolithography (3rd – both side alignment)

Figure
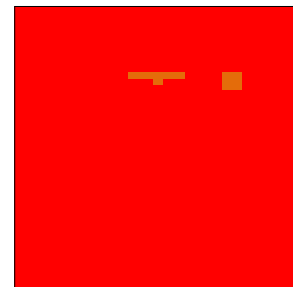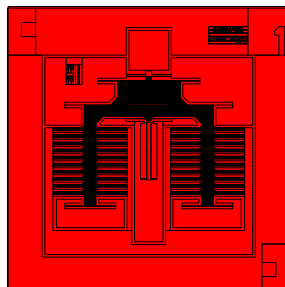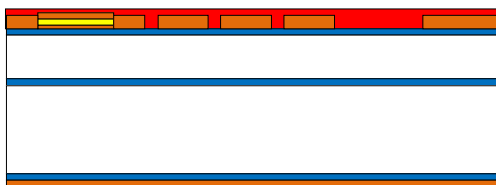
Condition

(1) Spin coating of OAP
    Rotation speed & time
    1st : 5 sec @ 1000 rpm
    2nd : 30 sec @ 5000 rpm
(2) Bake for drying OAP in the oven
    3 min @ 110 ºC
(4) Spin coating of Photoresist (OFPR800 23cp)
    Rotation speed & time
    1st : 5 sec @ 1000 rpm
    2nd : 30 sec @ 5000 rpm

(5) Pre-bake in the oven
    2 min @ 110 ºC
(6) Exposure
    Time : 6 sec
(7) Development (TMAH 2.38% NMD-3)
    Time : 15 min
(8) Pure wafer rinse : 10 min
(9) Post-bake on a hot-plate
    10 min @ 110 ºC

◯ Si   ● SiO2   ● Cr   ● P.R.   ● Al   ● Au

Fig. 3.3 Schematic diagram of the device fabrication process (continued).

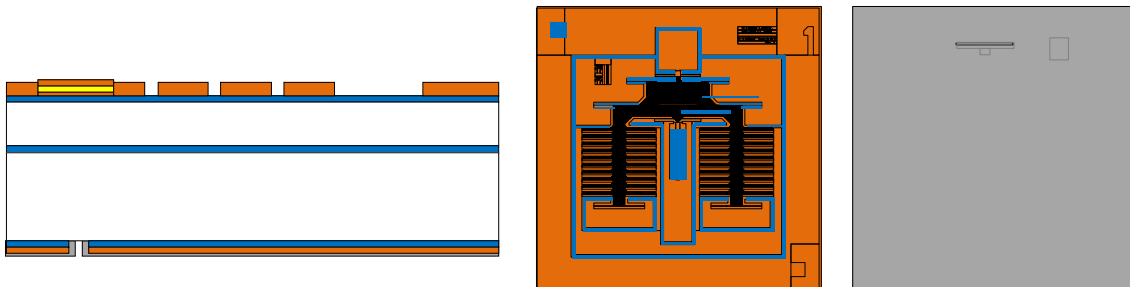| Process number |
|---|

17 Wet etching for Cr thin film

Figure
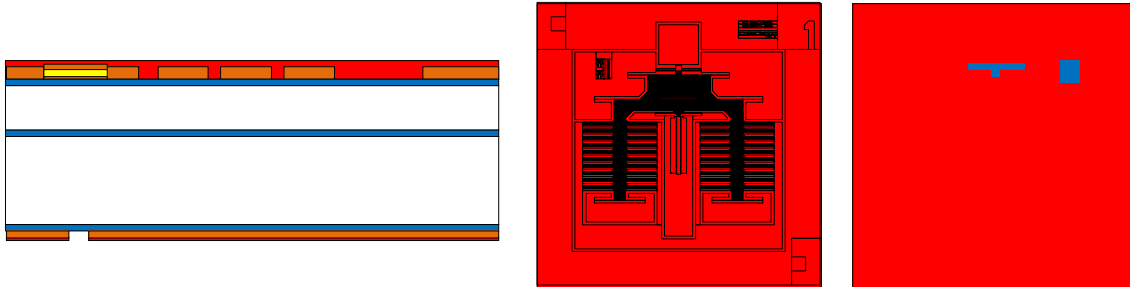
Condition

(1) Coating of photoresist by brush for protecting the comb drive
(2) Post-bake on a hot-plate
    10 min @ 110 ºC
(3) **Cooling the specimens for 2~3 hours**
(4) Chromium etching (Chromium etchant)
    Time : 60 sec **(Not dipping)**
(5) Pure wafer rinse : 10 min

Process number

18 Wet etching for SiO$_2$ layer

Figure

Condition

(1) BHF etching for SiO$_2$ layer : 15 min
(2) Pure wafer rinse : 10 min
(3) Photoresist removal (Remover 104)
    5 min @ 110 ºC
(4) Pure wafer rinse : 10 min
(5) SPM cleaning : 10 min
(6) Pure wafer rinse : 10 min

⚪ Si	🔵 SiO2	🟠 Cr	🔴 P.R.	⚪ Al	🟡 Au

Fig. 3.3 Schematic diagram of the device fabrication process (continued).

Process number

19 Photoresist removal & SPM cleaning
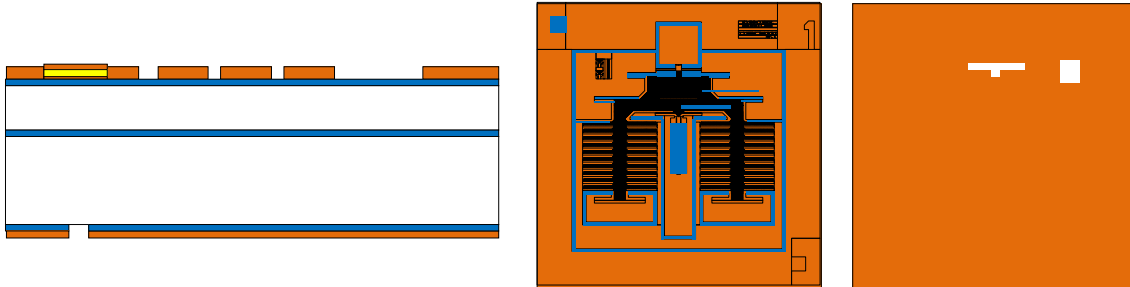
Figure

Condition

(1) Photoresist removal (remover 104)
    5 min @ 110 ºC (hotplate temp.)
(2) Pure wafer rinse : 10 min
(3) SPM cleaning : 10 min
    cleaning dummy chip also
(4) Pure wafer rinse : 10 min

Process number

20 Deposition of Aluminum thin film

Figure

Condition

(1) Deposition of Aluminum : 5 min
    Pressure : 1.0×10^{-3} Pa
    Current : **50 A**
    Al wire (ϕ = 0.5 mm – l = 50mm)

◯ Si	🔵 SiO2	🟠 Cr	🔴 P.R.	⚪ Al	🟡 Au

Fig. 3.3 Schematic diagram of the device fabrication process (continued).

Process number	# 21 Photoresist coating

Figure

Condition

(1) Dehydration bake on a hot-plate
    5 min @ 110 ºC
(2) Spin coat of photoresist (OFPR800 23cp) – **without using OAP**
    Rotation speed & time
    1st : 5 sec @ 1000 rpm
    2nd : 30 sec @ 3000 rpm
(3) Post-bake on a hot-plate : 10 min @ 110 ºC

Process number	# 22 Photolithography (4th – back-side alignment)

Figure

Condition

(1) Dehydration bake in the oven
    5 min @ 110 ºC
(2) Spin coating of OAP
    Rotation speed & time
    1st : 5 sec @ 1000 rpm
    2nd : 30 sec @ 5000 rpm
(3) Bake for drying OAP in the oven
    3 min @ 110 ºC
(4) Spin coating of Photoresist (OFPR800 23cp)
    Rotation speed & time
    1st : 5 sec @ 1000 rpm
    2nd : 30 sec @ 5000 rpm

(5) Pre-bake in the oven
    2 min @ 110 ºC
(6) Exposure
    Time : 1.8 sec
(7) Development (TMAH 2.38% NMD-3)
    Time : 30~40 min
    Also etching the aluminum layer
(8) Pure wafer rinse : 10 min
(9) Post-bake on a hot-plate
    10 min @ 110 ºC

◯ Si	🔵 SiO2	🟠 Cr	🔴 P.R.	⚪ Al	🟡 Au

Fig. 3.3 Schematic diagram of the device fabrication process (continued).

Process number

23 Wet etching for Aluminum thin film
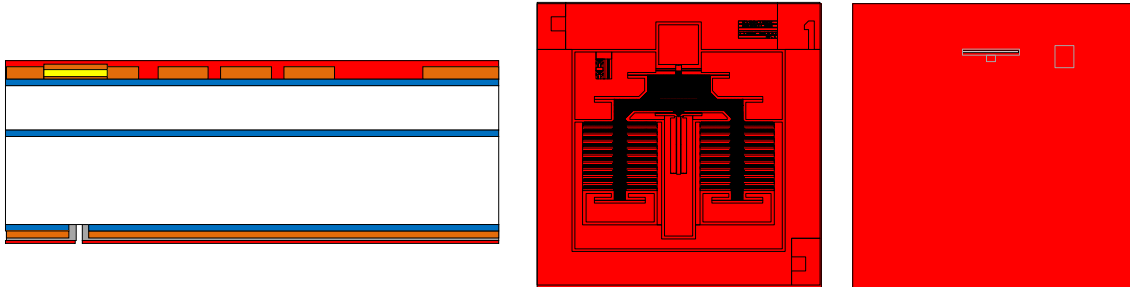
Figure

Condition

(1) Aluminum etching (Aluminum etchant) : 2 min
(2) Pure wafer rinse : 10 min

Process number

24 Photoresist removal

Figure

Condition

(1) Photoresist removal (remover 104)
     10 min @ 110 ºC (hotplate temp.)
(2) Pure wafer rinse : 10 min

◯ Si   🔵 SiO2   🟠 Cr   🔴 P.R.   ⚪ Al   🟡 Au

Fig. 3.3 Schematic diagram of the device fabrication process (continued).

Process number

25 Specimen cutting by dicing saw machine

Figure

Condition

(1) Dehydration bake on a hot-plate
    5 min @ 110 ºC
(2) Spin coating of photoresist (OFPR800 23 or 54cp)
    Rotation speed & time
    1st : 5 sec @ 500 rpm
    2nd : 30 sec @ 3000 rpm
(3) Bake on a hot-plate
    10 min @ 110 ºC
(4) Adhere a dicing sheet to the reverse side of SOI wafer
    Thickness : 80 µm

(5) Cut SOI wafer
    Blade speed : 5.0 mm/s
    Pitch : 11 mm (both)
(6) Rinse in acetone : 10 min (two times)
(7) Rinse in ethyl alcohol : 10 min
(8) Rinse in pure water : 10 min

Process number

26 Photoresist coating
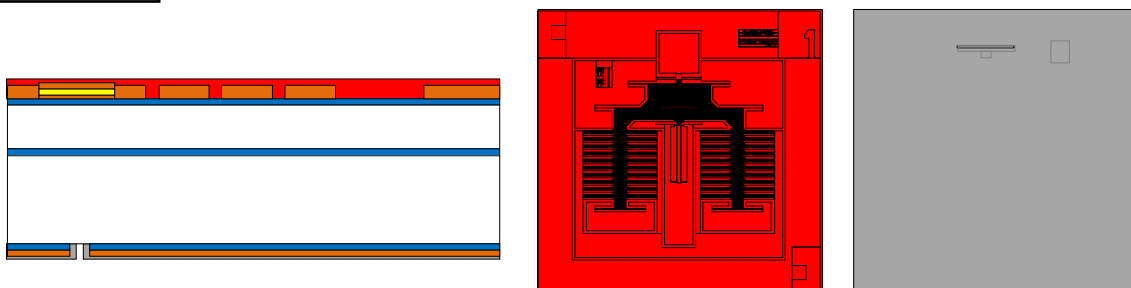
Figure

Condition

(1) Spin coat of photoresist (OFPR800 54cp) – **without OAP**
    Rotation speed & time
    1st : 5 sec @ 500 rpm
    2nd : 15 sec @ 1000 rpm
(2) Post-bake on a hot-plate : 10 min @ 110 ºC
(3) Repeat the procedure of (1-2)

   ⚪ Si   🔵 SiO2   🟠 Cr   🔴 P.R.   ⚪ Al   🟡 Au

Fig. 3.3 Schematic diagram of the device fabrication process (continued).

Process number

27 Dry etching for Substrate Silicon using ICP-RIE (1st ICP Etching)
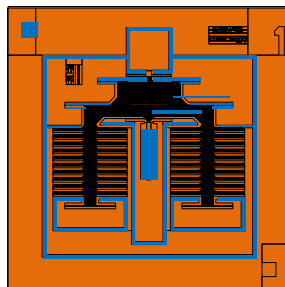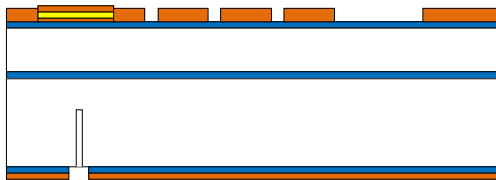
Figure
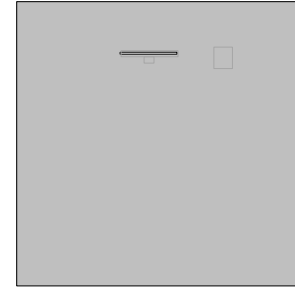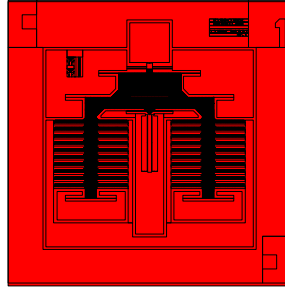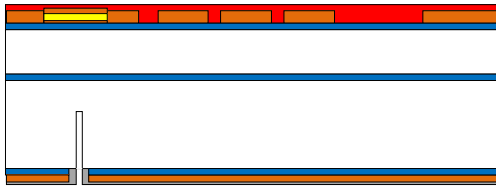
Condition

(1) Etching gas & flow rate : SF_6 130 sccm
   Etching time : 12 sec / cycle
   Etching pressure : **3 Pa**
   Passivation gas & flow rate : **C_4F_8 45 sccm**
   Passivation time : 5 sec / cycle
   Passivation pressure : 2.26 Pa
   Helium pressure : 1333 Pa
   Coil power : 600 W
   Platen power : 15 W
   Chiller temperature : 30 deg.
   Etching cycles : **300 cycles**

Process number

28 P.R. and Aluminum Removing

Figure
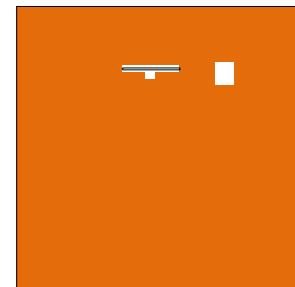
Condition

(1) Photoresist removal (remover 104)
    10 min @ 110 ºC (hotplate temp.)
(2) Pure wafer rinse : 10 min
(3) SPM cleaning : 10 min
(4) Pure wafer rinse : 10 min

◯ Si   🔵 SiO2   🟠 Cr   🔴 P.R.   ⚪ Al   🟡 Au

Fig. 3.3 Schematic diagram of the device fabrication process (continued).

Process number
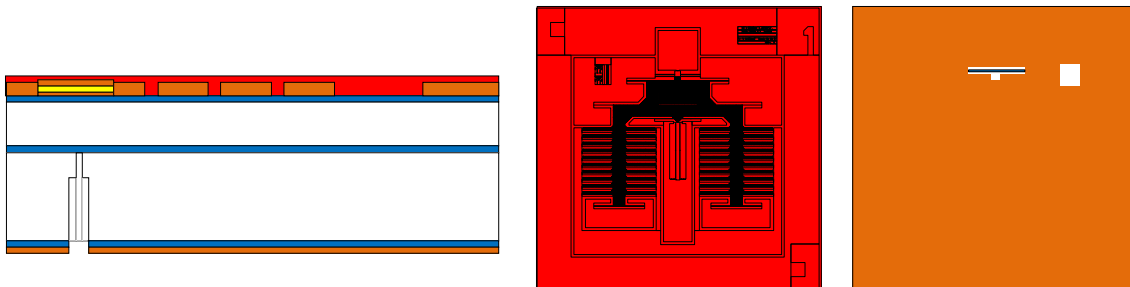
29 Photoresist coating
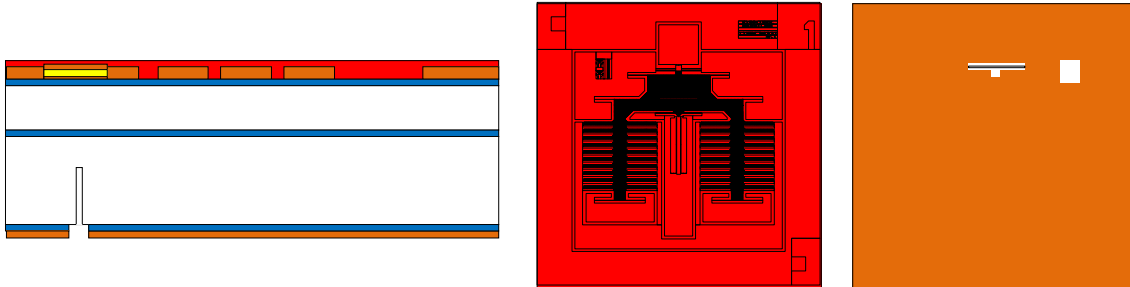
Figure

Condition

(1) Spin coat of photoresist (OFPR800 54cp) — **without OAP**
    Rotation speed & time
    1st : 5 sec @ 500 rpm
    2nd : 15 sec @ 1000 rpm
(2) Post-bake on a hot-plate : 10 min @ 110 ºC
(3) Repeat the procedure of (1-2)

Process number

30 Dry etching for Silicon by ICP-RIE (2nd ICP)

Figure

Condition

(1) Etching gas & flow rate : SF_6 130 sccm
    Etching time : 12 sec / cycle
    Etching pressure : 3 Pa
    Passivation gas & flow rate : C_4F_8 45 sccm
    Passivation time : 5 sec / cycle
    Passivation pressure : 2.26 Pa
    Helium pressure : 1333 Pa
    Coil power : 600 W
    Platen power : 15 W
    Chiller temperature : 30 deg.
    Etching cycles : **300 + 20 + 10 + a**
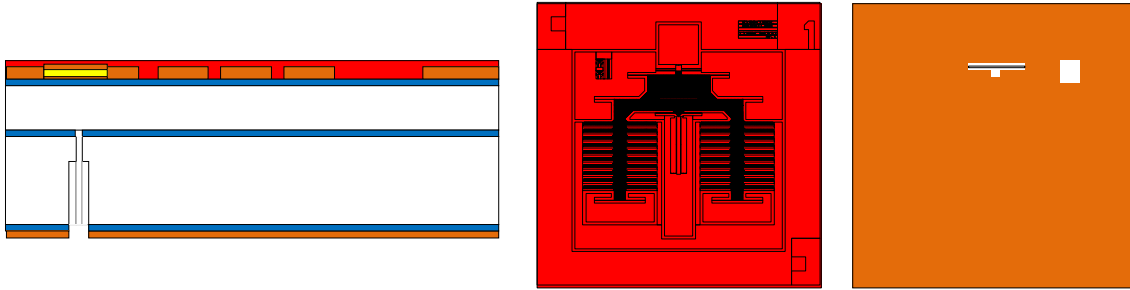
○ Si	● SiO2	● Cr	● P.R.	● Al	● Au

Fig. 3.3 Schematic diagram of the device fabrication process (continued).

Process number

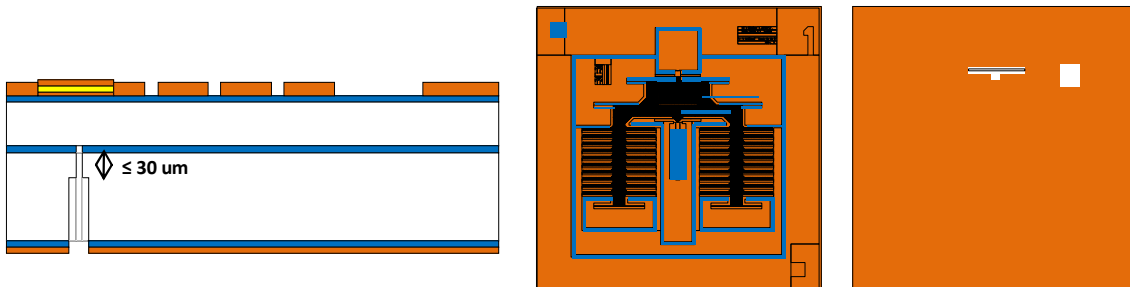# 31 Wet etching for SiO2 Buried oxide layer

Figure

Condition

(1)SiO$_2$ Etching (**HF** not BHF)
       Time : 5 min for 6 inch.
             6 min for 4 inch.
(2) Pure wafer rinse : 10 min
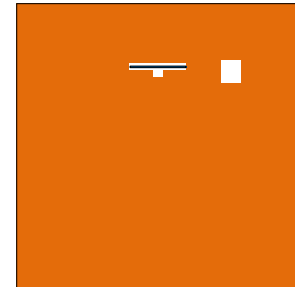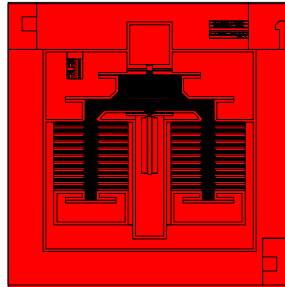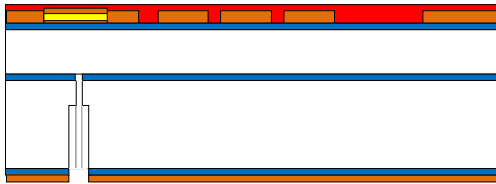
Process number

32 Photoresist removal

Figure

≤ 30 um

Condition

(1) Photoresist removal (remover 104)
       10 min @ 110 ºC (hotplate temp.)
(2) Pure wafer rinse : 10 min

Si   SiO2   Cr   P.R.   Al   Au

Fig. 3.3 Schematic diagram of the device fabrication process (continued).

Process number

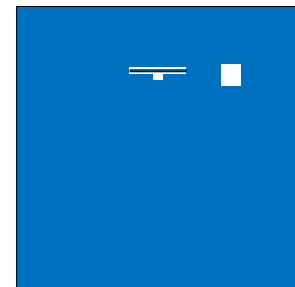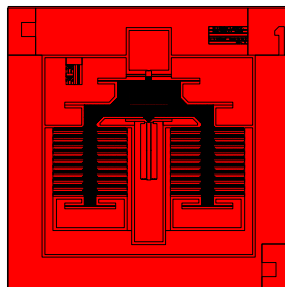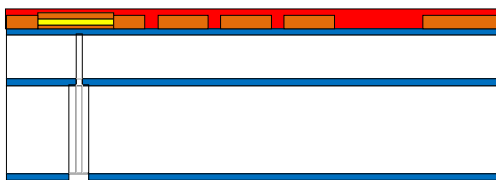# 33 Photoresist coating

Figure

Condition

(1) Spin coat of photoresist (OFPR800 54cp) – **without OAP**
   Rotation speed & time
   1st : 5 sec @ 500 rpm
   2nd : 15 sec @ 1000 rpm
(2) Post-bake on a hot-plate : 10 min @ 110 ºC

Process number

34 Dry etching for Silicon by ICP-RIE (3rd ICP) & Chromium etching by ICP-RIE
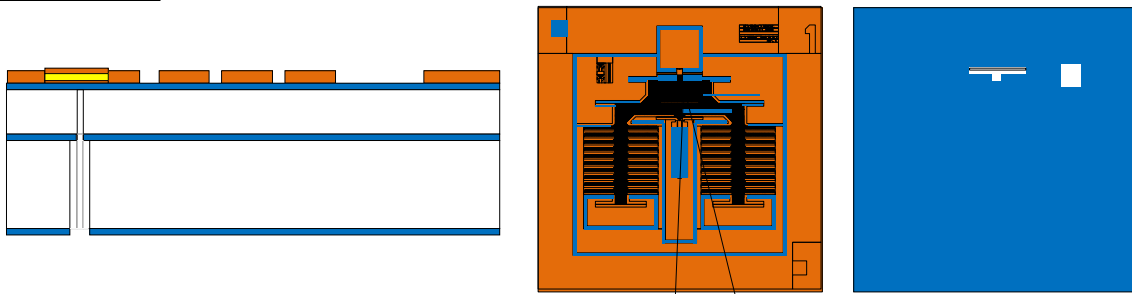
Figure

Condition

(1) Etching gas & flow rate : SF_6 130 sccm
   Etching time : 12 sec / cycle
   Etching pressure : 3 Pa
   Passivation gas & flow rate : C_4F_8 45 sccm
   Passivation time : 5 sec / cycle
   Passivation pressure : 2.26 Pa
   Helium pressure : 1333 Pa
   Coil power : 600 W
   Platen power : 15 W
   Chiller temperature : 30 deg.
   Etching cycles : **70**

(2) Cr etching : 5 min
   Etching gas : O_2
   RF Power : 600 W

| ◯ Si | 🔵 SiO2 | 🟠 Cr | 🔴 P.R. | ⚪ Al | 🟡 Au |

Fig. 3.3 Schematic diagram of the device fabrication process (continued).

Process number

35 Photoresist removal

Figure

Condition

(1) Photoresist removal (remover 104)
  10 min @ 110 ºC (hotplate temp.)
(2) Pure wafer rinse : 10 min
(3) SPM cleaning : 10 min
(4) Pure wafer rinse : 10 min
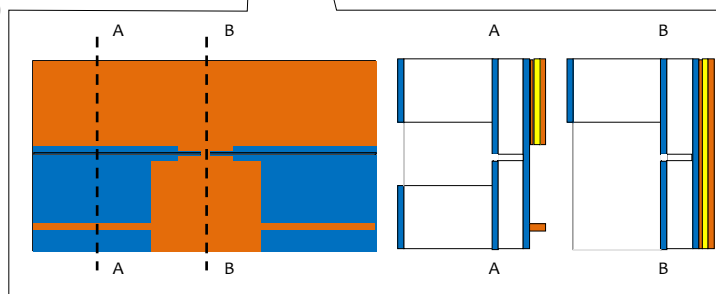
Process number

36 Dry etching for SiO_2 by RIE

Figure
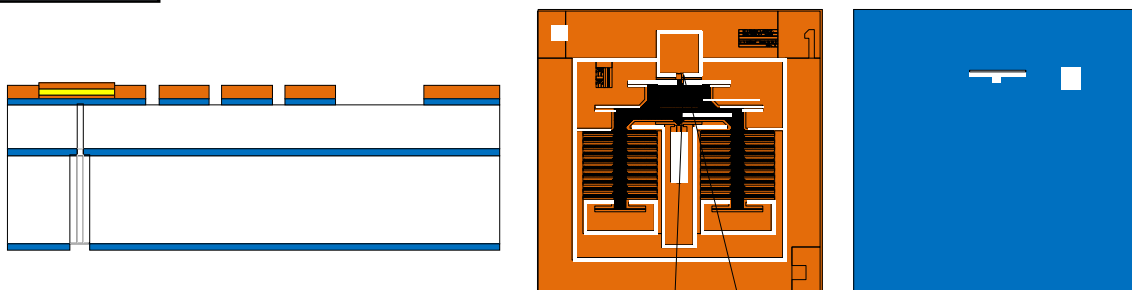
Condition

(1) SiO_2 thin film etching : **30 min**
  Etching gas : CHF_3 35 sccm
  Pressure : 5 Pa
  RF Power : 120W

| ○ Si | ● SiO2 | ● Cr | ● P.R. | ● Al | ● Au |
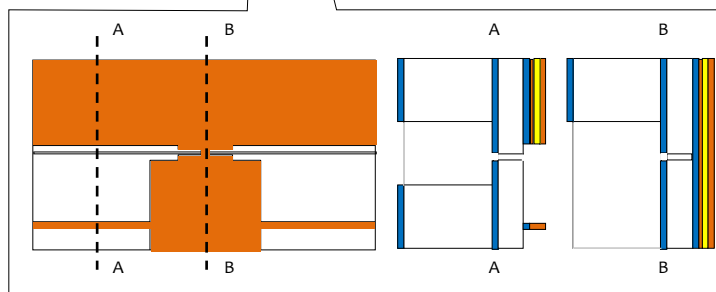
Fig. 3.3 Schematic diagram of the device fabrication process (continued).

Process number

37 Dry etching for Silicon by ICP-RIE (4th ICP)

Figure
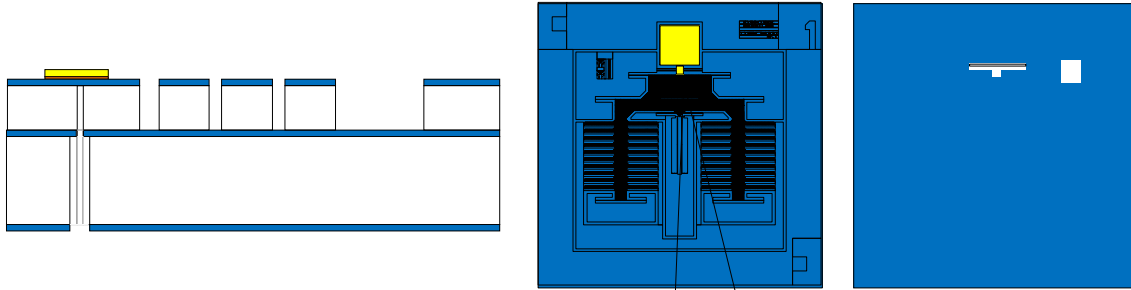
Condition

(1) Etching gas & flow rate : SF_6 130 sccm
    Etching time : 12 sec / cycle
    Etching pressure : 3 Pa
    Passivation gas & flow rate : C_4F_8 45 sccm
    Passivation time : 5 sec / cycle
    Passivation pressure : 2.26 Pa
    Helium pressure : 1333 Pa
    Coil power : 600 W
    Platen power : 15 W
    Chiller temperature : 30 deg.
    Etching cycles : **70**
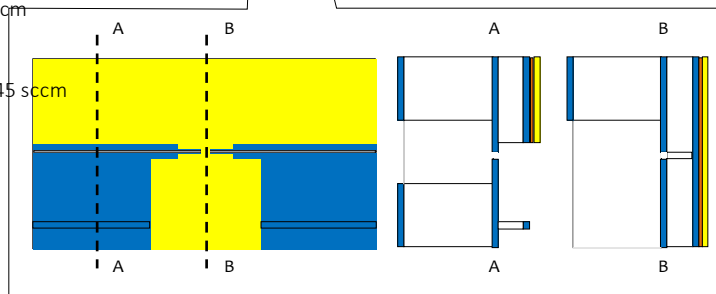
Process number

38 O_2 cleaning by ICP-RIE
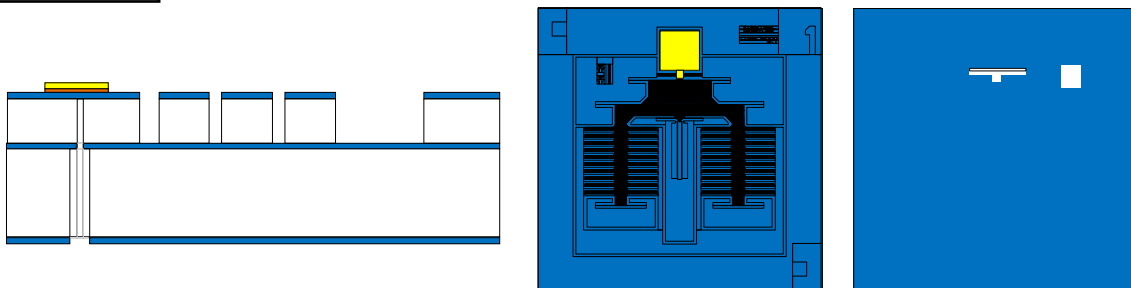
Figure

Condition

(1) Cr etching : 5 min
     Etching gas : O_2
     RF Power : 600 W

○ Si	● SiO2	● Cr	● P.R.	● Al	● Au

Fig. 3.3 Schematic diagram of the device fabrication process (continued).

Process number

39 Measurement of width/thickness of Au thin film specimen by AFM

Figure
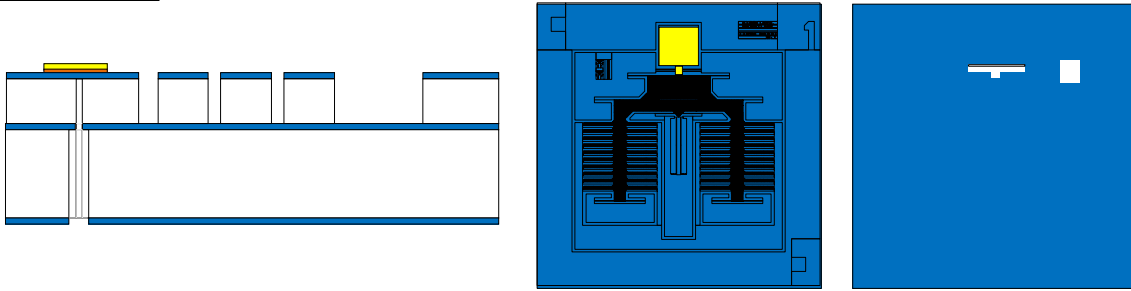
Condition

Process number

40 Vapor HF for etching silicon oxide layer
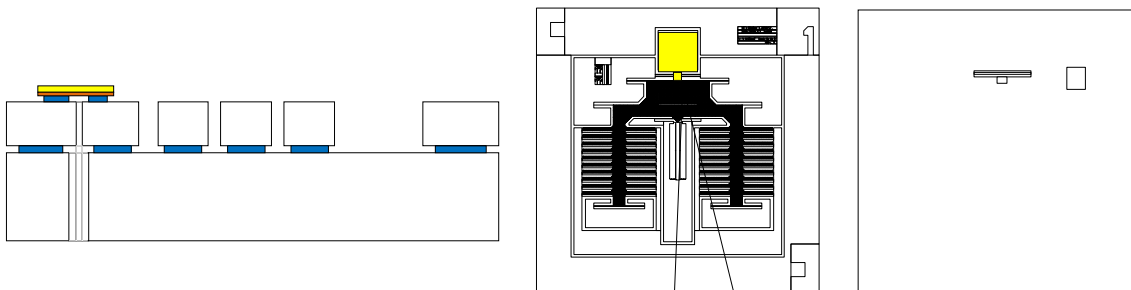
Figure

Condition

(1) Vapor HF
  Volume : 40 ml
  Chamber temp. : 50 deg. both
  Warm-up time : 90 min.
  Etching time : 15 min.
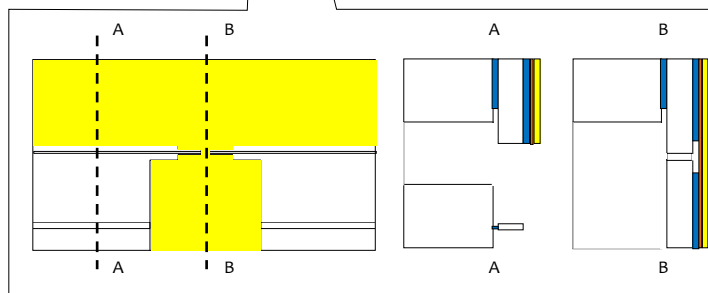
| ○ Si | ● SiO2 | ● Cr | ● P.R. | ● Al | ● Au |

Fig. 3.3 Schematic diagram of the device fabrication process (continued).

Process number

41 O_2 cleaning by ICP-RIE

Figure

Condition

(1) Cr etching : 5 min
   Etching gas : O_2
   Pressure : 5 Pa
   RF Power : 300 W

Process number

42 Vapor HF for etching silicon oxide layer

Figure

Condition

(1) Vapor HF
   Volume : 40 ml
   Chamber temp. : 50 deg. both
   Time : 90 min.
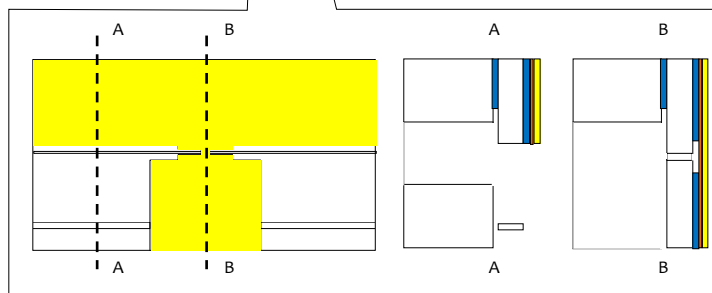
| Si | SiO2 | Cr | P.R. | Al | Au |

Fig. 3.3 Schematic diagram of the device fabrication process (continued).

Process number

43 Tensile Test

Figure
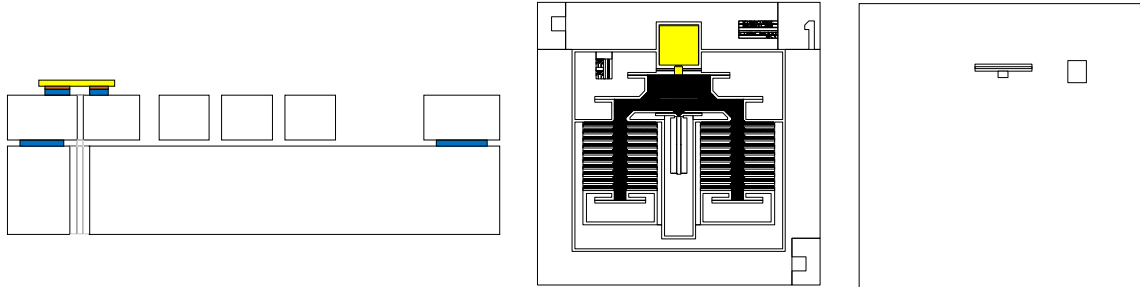
Condition

Process number

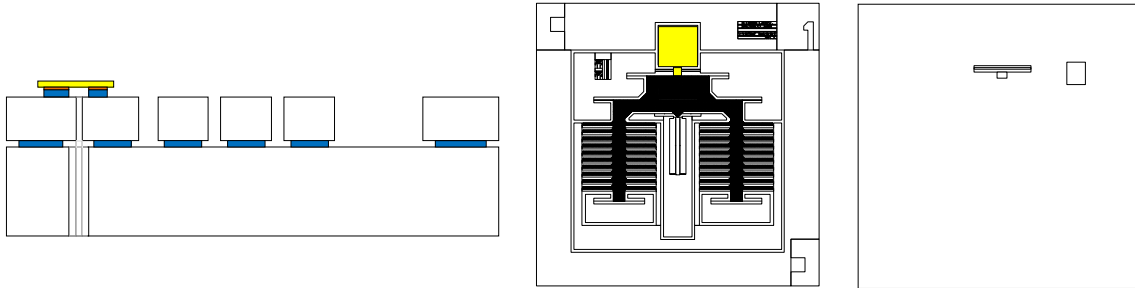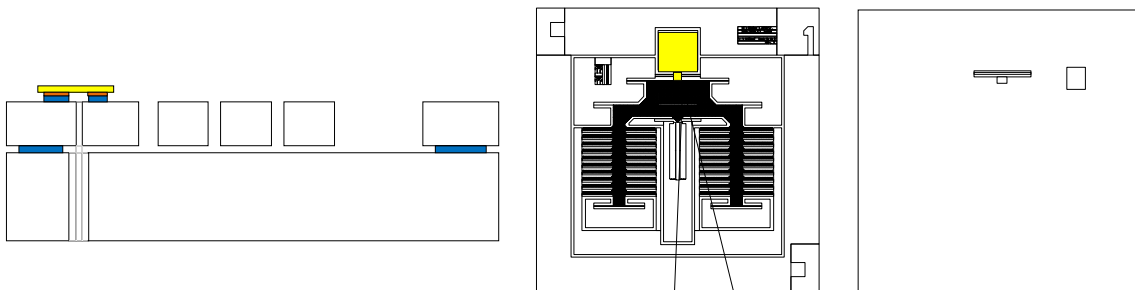# 44 Measurement for width of all supported beams by FE-SEM

Figure
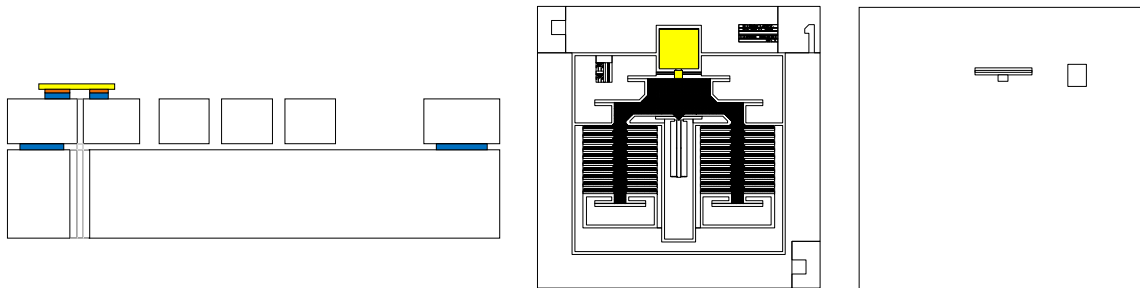
Condition

◯ Si   🔵 SiO2   🟠 Cr   🔴 P.R.   ⚪ Al   🟡 Au

Fig. 3.3 Schematic diagram of the device fabrication process.

3.3　Evaluation Technique of the Mechanical Properties for Au Films Using MEMS

Our scheme of tensile tests does not require the manipulation of the sub-100-nm thick specimens for alignment and fixation as they are already located on the device in the fabrication process. The tensile load on the specimens is applied by voltage on the comb drive actuators. As mentioned above, the preloading of the specimen is prevented by the gaps between the three parts of the device. As a consequence, the gradual increase of the applied voltage shows three stages of the load-displacement relation in the system.

The first stage starts just after the voltage application and it is defined in the period when the actuator part is not in contact with measurement and specimen part. The force f_1 on the actuator part is expressed by the displacement d_1 starting from the beginning of voltage application and the net spring constant k_1 originating from the suspended beams that support the actuator part as

$$f_1 = k_1 d_1 \qquad (3.1)$$

The displacement at the first stage is not explicitly detected as the measurement part is away from the actuator part. The second stage starts when the actuator part gets in contact with the measurement part while it is not in contact with the specimen part yet. The force f_2 by the actuator is described as

$$f_2 = k_1 d_{\mathrm{m}} + (k_1 + k_2) d_2 \qquad (3.2)$$

where d_{m} is the initial gap (3 μm on the specification) between the actuator part and the measurement part defined at the neutral position of the parts of the system, k_2 is the spring constant

by the suspended beams that support the measurement part, and d_2 is the displacement starting from the point where the gap between the actuator and the measurement part vanishes. Note that the origins of d_1 and d_2 are different. In other words, $d_m + d_2$ is the displacement of the actuator when the origin is defined at the neutral position of the actuator. The third stage starts when the actuator part gets in contact with the specimen part. The actuator part is in contact with both of the measurement and specimen parts and the elongation of the specimen starts. The force f_3 of actuator is described as

$$f_3 = k_1 d_m + (k_1 + k_2)(d_S - d_m) + (k_1 + k_2 + k_3)d_3 + f_S$$

(3.3)

where d_s is the initial gap (4 μm on the specification) between the actuator part and the specimen part at the neutral position of the system configuration, k_3 is the spring constant by the suspended beams that support the specimen part, d_3 is the displacement of the actuator part starting from the beginning of the third stage, and f_s is the tensile load acting on the specimen itself. Note that the origin of d_3 is different from that of d_2 or d_1. The initiation of the second and third stage can be read from the curve indicating the relation between the displacement of the cantilever edge and the applied voltage, which will be shown in the next section. In the actual measurement, d_3 is extracted from the displacement D of the cantilever edge of the lever-motion amplification system. Then, when the amplification factor is C, f_3 can be re-expressed as

$$f_3 = k_1 d_m + (k_1 + k_2)(d_s - d_m) + (k_1 + k_2 + k_3)[D/C - d_s] + f_s$$

(3.4)

The factor C was designed to be 20.1 as mentioned above. After the fracture of specimen, f_s vanishes from f_3. The force on the actuator by the voltage corresponding to the third stage after the specimen fracture leads to

$$f_4 = k_1 d_m + (k_1 + k_2)(d_s - d_m) + (k_1 + k_2 + k_3)[D'/C - d_s]$$

(3.5)

where D' is the displacement of cantilever edge after failure. Because simply $f_3 = f_4$ for the same voltage,

$$f_s = (k_1 + k_2 + k_3)(D' - D)/C \qquad (3.6)$$

Thus, the relation between the force on the specimen and the applied voltage can be determined from the voltage applications on the actuator firstly for the tensile test and secondly after that.

The relation between the voltage and displacement at the third stage of the tensile test is also used for the extraction of the strain of the specimen. The cross section and length of the specimen obtained from the scanning electron microscope (SEM) images are used for the conversion from the tensile load and elongation to the stress and strain, respectively. Thus, the stress-strain relation can be derived once the total spring constant of $k_1 + k_2 + k_3$ are calculated also using the SEM images of the cross sections of the beams that supports the three parts of the tensile testing device.

3.4   Results of Tensile Testing for Au Films Using MEMS

Fig. 3.4 shows the fabricated tensile testing device. The mean thickness and width of the six specimens were 88.3 ± 10.0 nm and 1.78 ± 0.31 μm, respectively. The details of the specimens are summarized in Table 3.2. As mentioned in the previous section, the tensile test consists of three stages from the viewpoint of the tensile loading and displacement detection. Fig. 3.5 shows an example of the displacement of the edge of cantilever that constitutes the lever-motion amplification system, as a function of the voltage applied on the comb-drive actuator. At the first stage, the voltage does not lead to the deflection of the cantilever. This range corresponds to the state where the actuator edge approaches the measurement part. The second stage of the tensile loading begins when the actuator reaches the measurement part. Initiation of the third stage can be observed by the discontinuous change of gradient in the deflection-voltage curve. The existence of these distinctive stages ensures the assumption of no preloading on the specimen by the geometric interference between the specimen, actuator, and measurement parts. A set of the two deflection-voltage curves, i.e., one is for the tensile loading on the specimen and the other is after the fracture of the specimen, is used for the derivation of the stress-strain curve of a specimen.
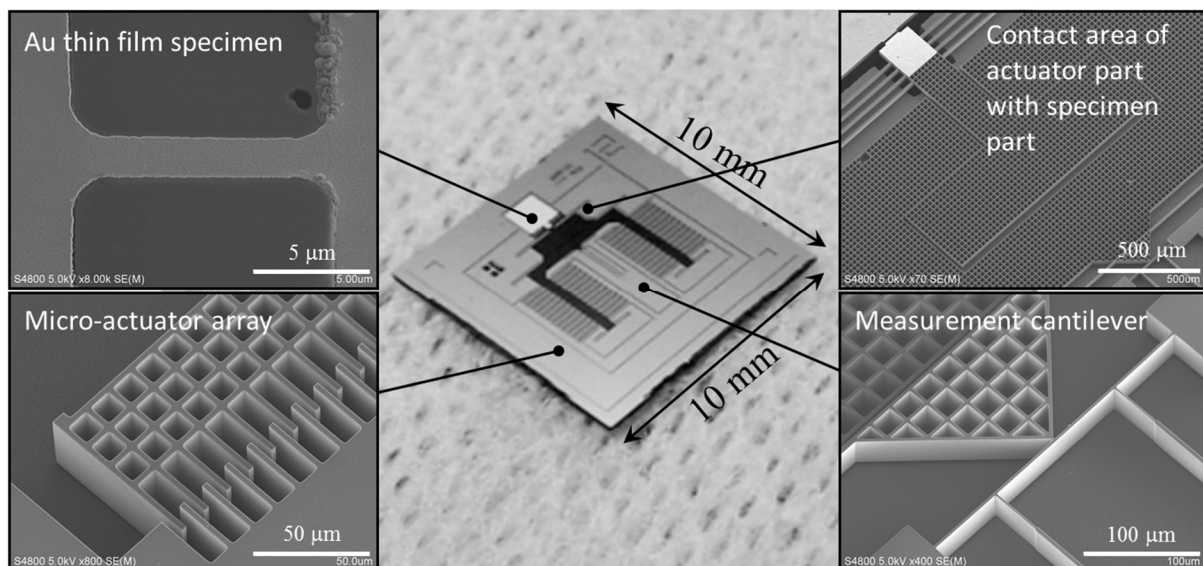
Fig. 3.4 SEM images of the fabricated device. The center figure is the overall view, and the both sides are specimen part, measurement part, and actuator part.

Table 3.2 Conditions and characteristics of the specimens.

Specimen Label	Strain rate (s^{-1})	Width (μm)	Length (μm)	Thickness (nm)
A	5×10^{-5}	1.70±0.03	11.25	80.5±8.9
B	1×10^{-4}	2.20±0.03	9.10	100.6±19.3
C	1×10^{-3}	1.66±0.02	8.80	93.5±24.8
D	2×10^{-3}	1.94±0.03	8.50	94.5±13.3
E	1×10^{-2}	1.88±0.02	8.86	84.7±19.0
F	5×10^{-2}	1.31±0.03	10.67	75.8±37.0
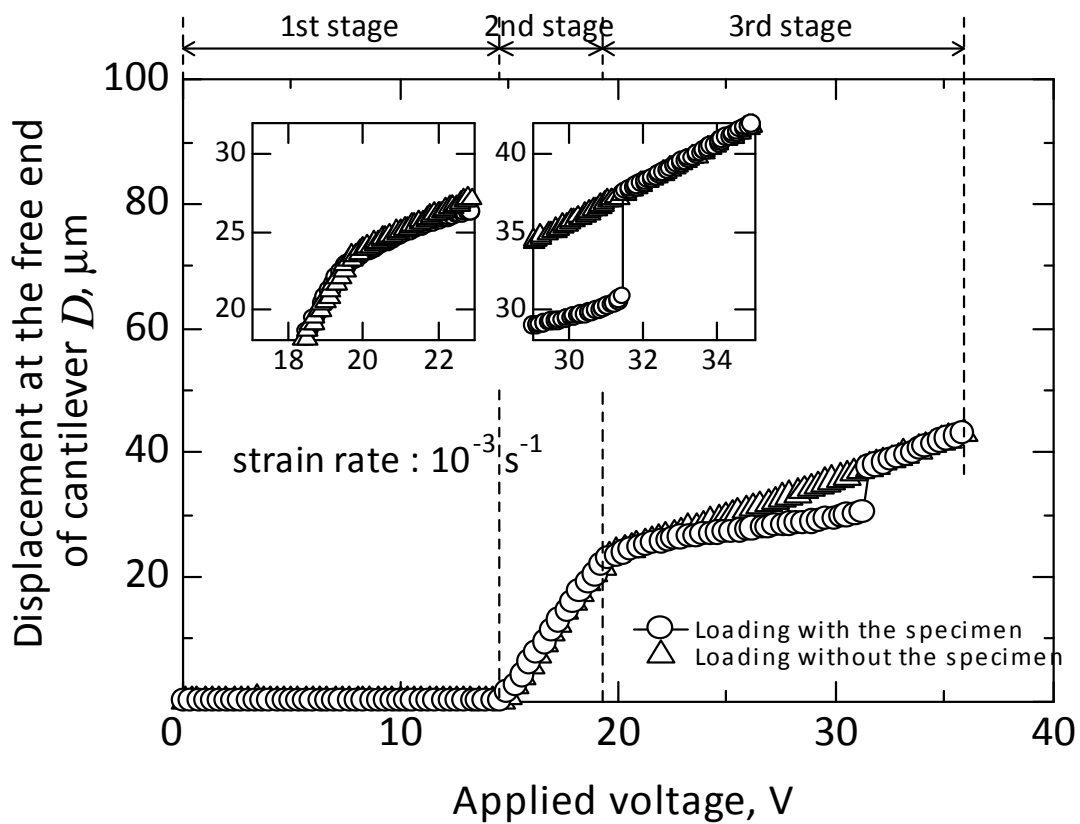
Fig. 3.5 Displacement of the cantilever edge of lever-motion amplification system as a function of the applied voltage in a tensile test.

Thus, a single tensile test consists of the loading procedure with and without a specimen. The obtained stress-strain relations of the Au thin films under different strain rates ranging from 5×10^{-5} s^{-1} to 5×10^{-2} s^{-1} are shown in **Fig. 3.6**. In order to derive these relations using **Eq. (3.6)**, total spring constants of the devices were obtained from the lengths, widths and cross sections of the supporting beams with elastic constant 169 **GPa** of the bulk single crystal silicon **[10]**. The cross section of the specimen necessary for the conversion of the force into the stress was measured by the SEM and AFM. The definition of strain was not a trivial problem. One of the specimens after the fracture by the tensile test is shown in **Fig. 3.7**. It can be observed that the both edge of the specimen have noticeable radius of curvature. The curvature was caused by the inherent limitation of the wet etching process in the specimen fabrication. This shape leaves an ambiguity in the length of specimen. Therefore, we defined the initial specimen length as the length of the part with the uniform width. Then, the relation between the elongation at the part with the uniform width and the directly measured total elongation in the tensile test was estimated by FEM. The computational model of FEM was based on the linear elastic model, and only the strain distribution was used for this estimation. We extracted the Young's modulus of each specimen from the linear regime of the deformation and plastic properties from the nonlinear regime shown in **Fig. 3.6**. In order for the strain to be defined uniquely in the stress-strain curves, the relation between the cantilever deflection and the elongation at the part of uniform width was assumed to be constant throughout the tensile test.

Defining the stress and strain in this way, the Young's modulus was determined to be 28±3 **GPa**. This is less than 40 % of the 79 **GPa** of the bulk Au and was insensitive to the strain rate **[11]**. In fact, the small Young's modulus of Au thin films compared to the bulk has been reported previously by several groups **[12-17]**. For example, Haque and Saif conducted the tensile tests of an Au film with a thickness of 350 nm fabricated by sputtering method **[14]**. They obtained the Young's modulus of 52 **GPa**. The elastically softer nature of grain boundary region compared to the grain interior was attributed to the main origin of such characteristics. The nature of grain boundary as well as their concentration or density depends on the material fabrication process. Thus, it is important to directly test such characteristics. Chasiotis *et al.* have conducted the tensile tests of Au films with thickness of 500 **nm** and 650 **nm** **[15]**. They obtained the Young's modulus of 35 **GPa** without any trend with strain rate or film thickness. They considered after the careful comparison with the existing reports that the small Young's modulus
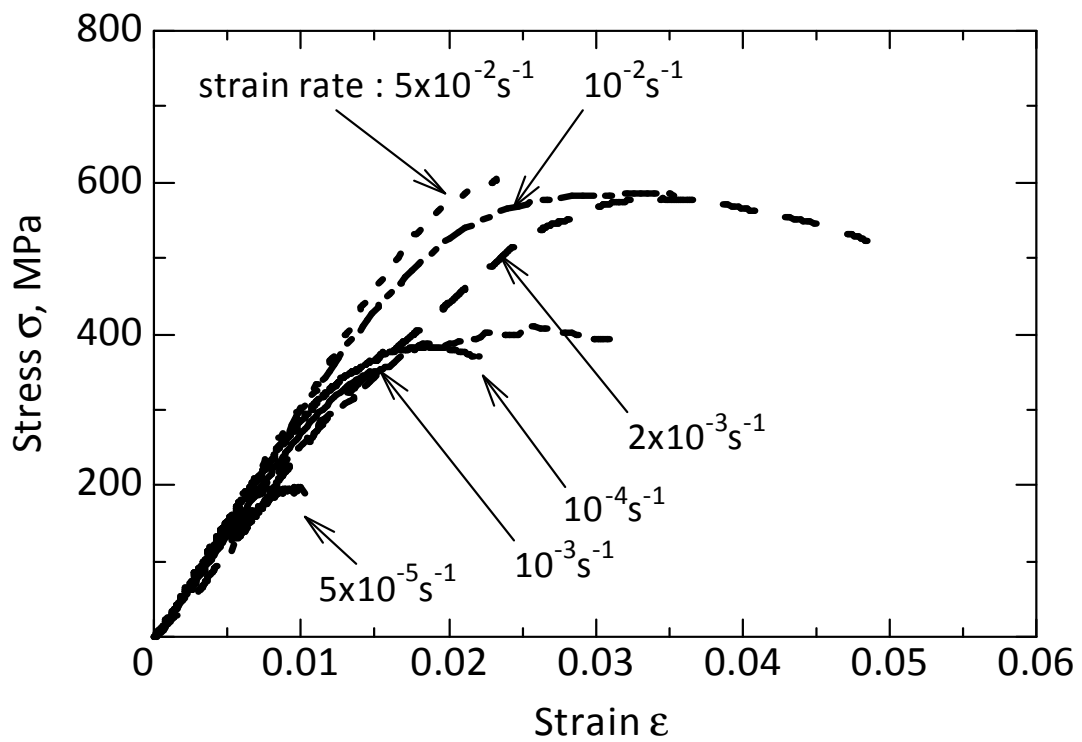
Fig. 3.6 Stress-strain relations of the specimens tested under the conditions of various strain rates.
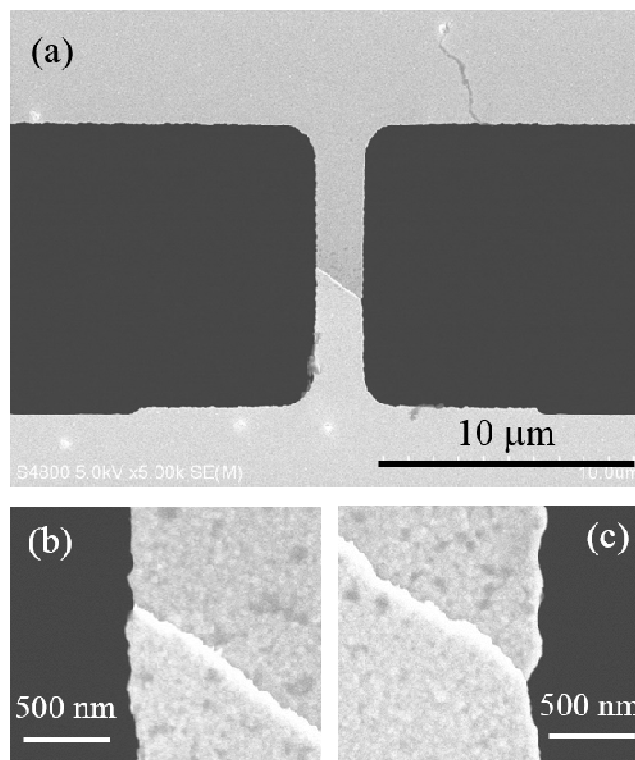
Fig. 3.7 SEM images of the specimen after the tensile test.

of their specimen was not due to the inelastic deformation mechanism but rather likely to be caused by the density lower than the bulk material. The lower density is related to the higher volume percentage of grain boundaries where the interatomic distances are longer than regular crystal structure. This can be related to the discussion by Haque and Saif [14]. In fact, the Young's modulus of an Au thin film can be different depending on the measurement methods. Emery and Povirk investigated the tensile properties of Au films with thickness ranging from 200 to 2000 nm [12]. They found that the Young's moduli obtained from the repeated loading were smaller than those obtained from repeated unloading.

Furthermore, they also found that the first loading process showed remarkably smaller Young's moduli compared to those obtained from the repeated loading after that. The Young's moduli of the films with thickness of 230 and 700 nm were in the range from 39 to 50 GPa when obtained from the first loading. The substantially smaller Young's modulus of sub-100-nm-thick Au films compared to the bulk is in qualitative agreement with the trend that have been reported on the thicker films. However, our result indicates even smaller value. The deposited metal thin films are not suitable for masking against wet etching process. This implies the existence of interstitial voids or pores which act as channels for etchants. As mentioned above, some of the existing studies point out the important role of grain boundaries in the soft elastic properties of the Au thin films. Therefore, a possible analogy with the property of nano-porous Au is worth some attention. The reported Young's modulus of the nano-porous Au is in the range from 5 to 40 GPa depending on the so-called ligament sizes [18-24]. Mathur and Erlebacher showed that the Young's modulus of nano-porous Au increases with decreasing ligament size, and obtained 40 GPa for the ligament size of 3 nm [22]. Although the texture is fundamentally different, these reports support the hypothesis that the vacancies between the grains of Au thin films plays some role in the Young's modulus substantially smaller than the bulk Au.

From above discussions, this research also observed the grain size of the Au thin films by SEM (Hitachi, S4800) and AFM (SII, SPM-HV-300) in the deposition process sequence. Table 3.3 lists SEM and AFM images of the Au thin films, which were deposited by the thermal evaporation and the RF-sputtering after the evaporation. Specific conditions are explained in Fig 3.3 #5 and #6. The Au thin film deposited by the thermal evaporation using the Au wire with a volume of 0.39 mm^3 has the grain size of 10 to 20 nm, and the grains were not combined each other in
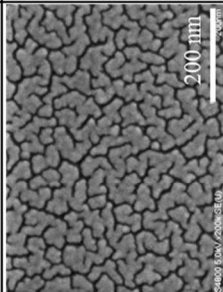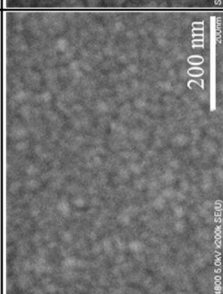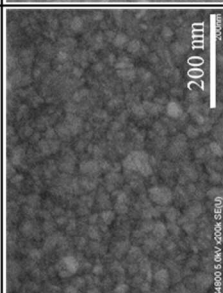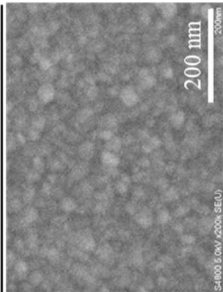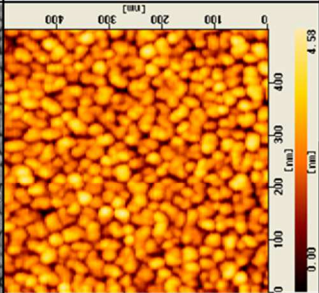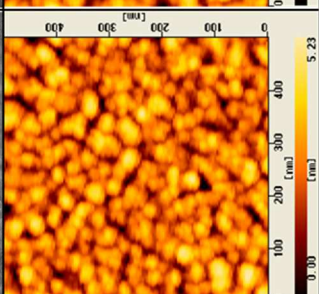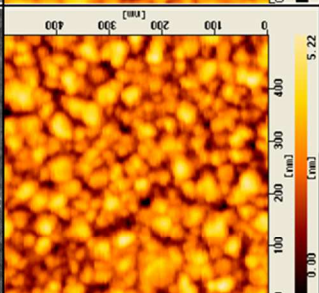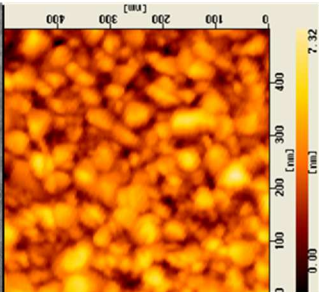
the SEM image. The ligament grains are observed in the SEM image of the Au thin film deposited using the Au wire with a volume of 0.98 mm^3. This was caused by that the tiny grains would have partially connected to the neighboring grains during the evaporation, but there are still a lot of vacancies between the ligaments. The surface of the Au film deposited by the RF-sputtering for 5 seconds, after the evaporation using the Au wire with a volume of 1.96 mm^3, shows again the spherical grains with the size of around 30 nm. The vacancies are also observed in the AFM image. In SEM and AFM images of the Au film after the RF-sputtering for 10 seconds, the grain size becomes 30 to 50 nm, and the vacancies are still observed in places although it reduces. Thus, the Au thin films prepared in this research would have consisted of small Au grains with the size ranging from 10 to 50 nm including several vacancies. These microstructures of the Au films caused the remarkably smaller Young's moduli in this research.

The actual tensile testing of the material provides the information of the plastic properties as well as the elastic property. **Fig. 3.7** shows that the normal direction of the fractured cross section is tilted against the tensile direction (**Fig. 3.7 (a)**). This feature was noticeable in all of the six specimens although the angles were difficult to determine because of the curl of fractured specimens except for the one shown in **Fig. 3.7.** Chasiotis *et al.* observed that the strain rate of 10^{-4} s^{-1} led to the shear failure for the Au thin film having thickness of 500 to 650 nm after the tensile test [15]. They also observed the Lüders band on the surface of the shear failure. On the other hand, we did not find Lüders band in the SEM image of fractured specimens.

In contrast to the Young's modulus, the yield strength defined as the 0.2 % offset yield strength depended on the strain rate of the tensile test because of deciding the exact yield strength. The yield strength decreased with decreasing strain rate as shown in **Fig. 3.8**. The yield strength suddenly decreased in the range of strain rate smaller than 10^{-3} or 10^{-4} s^{-1}. This would be caused by the effect of creep deformation of Au thin film. The specific values are summarized in **Table 3.4.** Compared to other researches, the yield strength by Emery and Povirk also depended on the strain rate while the film thickness was larger and the strain rate range was lower than this study [12]. Using the film with a thickness of 230 nm, they obtained 236, 360, and 455 MPa at the strain rates of 7×10^{-6} s^{-1}, 6×10^{-5} s^{-1}, 6×10^{-4} s^{-1}, respectively. In fact, the 360 MPa at 6×10^{-5} s^{-1} is equal to our result at 1×10^{-4} s^{-1}. On the other hand, Chasiotis *et al.* have obtained the 0.2 % yield stress of the 500-nm-thick Au films ranging from 140 to 240 MPa,

Table 3.3 SEM and AFM images of Au film surfaces deposited by thermal evaporation and sputtering process.

	Thermal evaporation using Au wire with a volume of 0.39 mm³	Thermal evaporation using Au wire with a volume of 0.98 mm³	Sputtering for 5 sec. after thermal evaporation	Sputtering for 10 sec. after thermal evaporation	Sputtering for 25 sec. after thermal evaporation
SEM images					
AFM images					

where the lower strain rates in the range of 10^{-6} s^{-1} to 10^{-3} s^{-1} led to lower strengths [15]. Jon-nalagadda *et al.* report the yield stress of 575 to 895 MPa for the Au films having thickness of 850 to 1760 nm, and the yield stress decreased with decreasing strain rate [16]. They concluded that the range from 10^{-5} to 10^{-4} s^{-1} of strain rate is pivotal in the inelastic mechanical response. Lee *et al.* reports the 0.2 % yield strength of 361 to 402 MPa for the Au films having 1000 to 2000 nm [17]. The texture of the film determined in the fabrication process is likely to be the origin of these differences in the reported values of yield strengths of Au thin films.

The variations of fracture and tensile strengths with decreasing strain rate also show similar trends to the yield strength-strain rate relation, as shown in **Fig. 3.9**. Besides the 0.2 % yield strength, tensile strength, fracture strength and fracture strain obtained from all the specimens are also summarized in **Table 3.4**. Although there seems to be the trend of smaller strength values with smaller strain rates, the strain-rate dependences were less clear than the 0.2 % yield strength. This is because the fracture strength and strain of the specimen are strongly affected by the presence of notch shapes that act as the source of crack. **Fig. 3.7 (b) and (c)** show the enlarged views of fracture. It can be seen that the crack propagation was initiated from the part of notched points unless this feature was generated in the course of plastic deformation itself. **Fig. 3.6** indicates the large variation in the fracture strain. This is because the notch structures are stochastically formed in the film fabrication process. In this sense, this unclear trend itself also reflects the intrinsic nature of the extremely thin films.
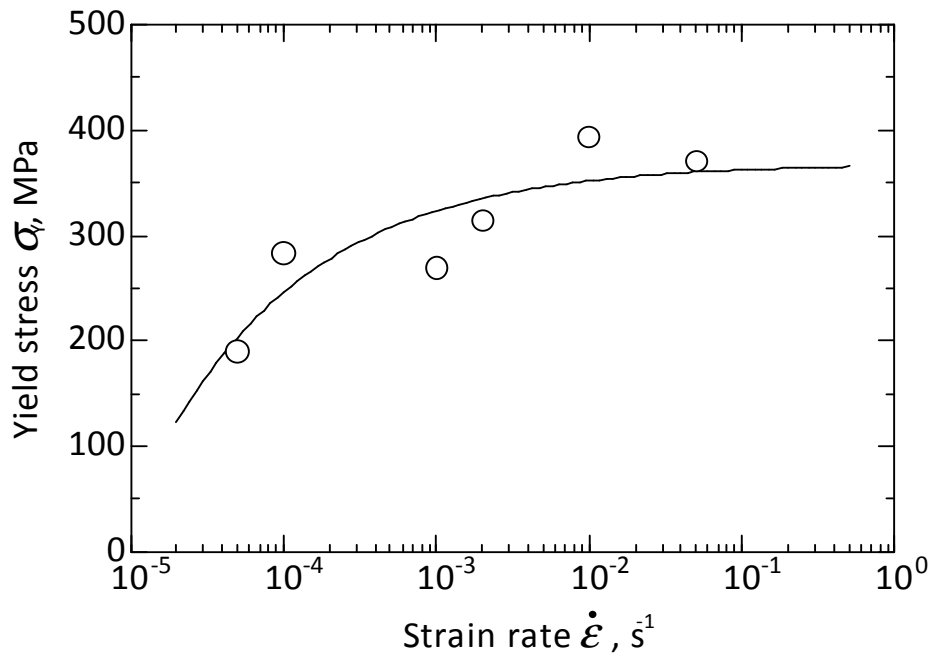
Fig. 3.8 Strain-rate dependence of the yield strength.
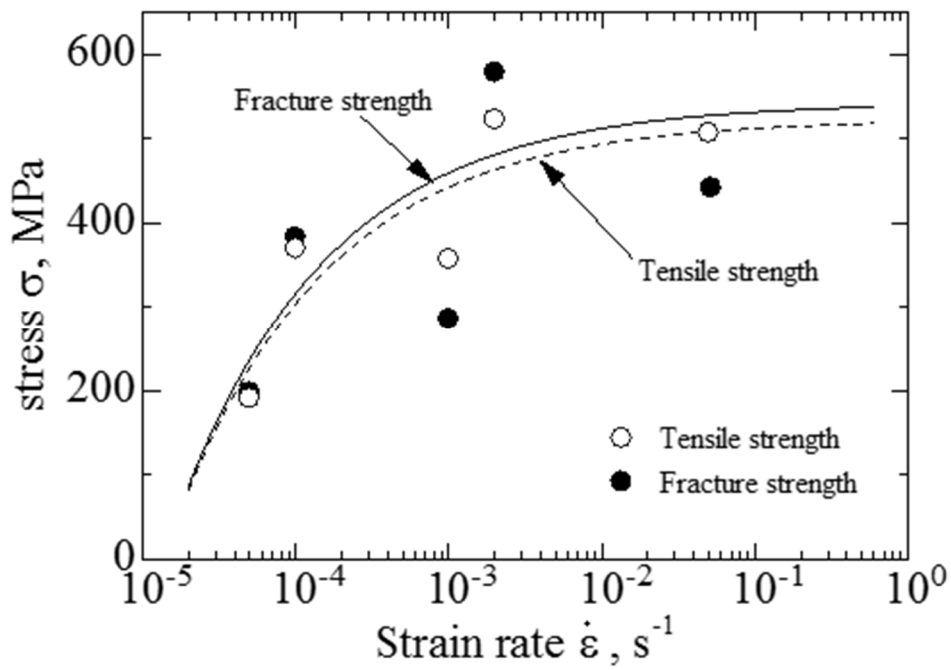
Fig. 3.9 Strain-rate dependence of the tensile and fracture strength.

Table 3.4 Mechanical properties obtained from the tensile tests. E : Young's modulus, σ_y: 0.2% yield strength, σ_T : tensile strength, σ_F : fracture strength, ε_F : fracture strain.

Specimen Label	E (GPa)	σ_y (MPa)	σ_T (MPa)	σ_F (MPa)	σ_F (%)	Thickness (nm)
A	24.3	192	198	191	1.01	80.5±8.9
B	29.3	360	383	370	2.21	100.6±19.3
C	27.0	351	357	357	1.60	93.5±24.8
D	24.8	432	579	523	4.86	94.5±13.3
E	29.5	519	586	587	3.56	84.7±19.0
F	35.0	477	507	507	1.94	75.8±37.0

3.6   Conclusions

In this study, we have developed the tensile testing device for Au thin films in the thickness regime of sub-100-nm. The obtained mechanical properties showed marked differences from those of the bulk Au. The Young's modulus was 28 ± 3 GPa, which is less than 40 % of that of the bulk Au. The 0.2 % yield strength was 192 to 519 MPa with a trend of decrease with decreasing strain rates in the range from 5×10^{-5} s^{-1} to 5×10^{-2} s^{-1}. The tensile strength was in the range from 198 to 519 MPa, and the fracture strength was 191 to 587 MPa. The small Young's modulus was attributed to the existence of voids in the material characterized by the fabrication process of vapor deposition and RF sputtering method. The consequent lumpy surface also leads to the large variation of fracture strain because the initiation points of cracks are the notched parts which are stochastically determined by the fabrication process. Thus, the direct tensile tests of extremely thin Au films revealed the strong influence of material fabrication process on the mechanical properties.

References

[1]   S. Oleksandrov, J. Lee, S. Lee, M. Lee, H. Y. Choi, C. Chung: Fabrication of Micro- and Nano-Scale Gold Patterns on Glass by Transfer Printing, *Journal of Nanoscience and Nanotechnology*, vol. 9, no. 12, pp. 7481-7484, 2009.

[2]   B. D. Gates, Q. Xu, M. Stewart, D. Ryan, C. G. Willson, G. M. Whitesides: New Approaches to Nanofabrication: Molding, Printing, and Other Techniques, *Chemical Reviews*, vol. 105, no. 4, pp. 1171-1196, 2005.

[3]   K. Ojima, Y. Otsuka, T. Matsumoto, T. Kawai: Printing electrode for top-contact molecular junction, *Applied Physics Letters*, vol. 87, 234110, 2005.

[4]   Y. Loo, D. V. Lang, J. A. Rogers, J. W. P. Hsu: Electrical Contacts to Molecular Layers by Nanotrasfer Printing, *Nano Letters*, vol. 3, no.7, pp. 913-917, 2003.

[5]   Y. Loo, R. L. Willet, K. W. Baldwin, J. A. Rogers: Additive, nanoscale patterning of metal films with a stamp and a surface chemistry mediated transfer process: Applications in plastic electronics, *Applied Physics Letters*, vol. 81, no. 3, pp. 562-564, 2002.

[6]   M. Kiuchi, S. Matsui, Y. Isono: Mechanical Characteristics of FIB Deposited Carbon Nanowires Using an Electrostatic Actuated Nano Tensile Testing Device, *Journal of Microelectromechanical Systems*, vol. 16, no. 2, pp. 191-201, 2007.

[7]   M. Kiuchi, S. Matsui, Y. Isono: The piezoresistance effect of FIB-deposited carbon nanowires under severe strain, *Journal of Micromechanics and Microengineering*, vol. 18, 065011, 2008.

[8]   C. Q. Davis, D. M. Freeman: Statistics of subpixel registration algorithms based on spatiotemporal gradients or block matching, *Optical Engineering*, vol. 37, no. 4, pp. 1290-1298, 1998.

[9]   C. Q. Davis, D. M. Freeman: Using a light microscope to measure motions with nanometer accuracy, *Optical Engineering*, vol. 37, no. 4, pp. 1299-1304, 1998.

[10]   W. A. Brantley: Calculated elastic constants for stress problems associated with semiconductor devices, *Journal of Applied Physics*, vol. 44, no. 1, pp. 534-535, 1973.

[11]   S. Lapman: ASM handbook vol.2 (ASM International,cleveland,1990)

[12]   R. D. Emery, G. L. Povirk: Tensile behavior of free-standing gold films. Part II. Fine-grained

films, *Acta Materialia*, vol. 51, pp. 2079-2087, 2003.

[13] H. D. Espinosa, B. C. Prorok: Size effects on the mechanical behavior of gold thin films, *Journal of Materials Science*, vol. 38, pp. 4125-4128, 2003.

[14] M. A. Haque, M. T. A. Saif: Deformation mechanisms in free-standing nanoscale thin films: A quantitative in situ transmission electron microscope study, *Proceeding on National Academy of Sciences*, vol. 101, no. 17, pp. 6335-6340, 2004.

[15] I. Chasiotis, C. Bateson, K. Timpano, A. S. McCarty, N. S. Barker, J. R. Stanec: Strain rate effects on the mechanical behavior of nanocrystalline Au films, *Thin Solid Films*, vol. 515, pp. 3183-3189, 2007.

[16] K. Jonnalagadda, N. Karanjgaokar, I. Chasiotis, J. Chee, D. Peroulis: Strain rate sensitivity of nanocrystalline Au films at room temperature, *Acta Materialia*, vol. 58, pp. 4674-4684, 2010.

[17] S. J. Lee, J. M. Park, S. W. Han, S. M. Hyun, J. H. Kim, H. J. Lee: Electromechanical Characterization of Au Thin Films using Micro-tensile Testing, *Experimental Mechanics*, vol. 50, pp. 543-649, 2010.

[18] J. Biener, A. Hodge, A. Hamza, L. Hsiung, J. Satcher Jr.: Nanoporous Au: A high yield strength material, *Journal of Applied Physics*, vol. 97, 024301, 2005.

[19] C. Volkert, E. Lilleodden, D. Kramer, J. Weissm̈uller: Approaching the theoretical strength in nanoporous Au, *Applied Physics Letters*, vol. 89, 061920, 2006.

[20] E. Seker, J. Gaskins, H. Barth-Smith, J. Zhu, M. Reed, G. Zangari, R. Kelly, M. Begley: The effects of post-fabrication annealing on the mechanical properties of freestanding nanoporous gold structures, *Acta Materialia*, vol. 55, pp. 4593-4602, 2007.

[21] J. Zhu, E. Seker, H. Bart-Smith, M. Begley, R. Kelly, G. Zangari, W. Lye, M. Reed: Mitigation of tensile failure in released nanoporous metal microstructures via thermal treatment, *Applied Physics Letters*, vol. 89, 133104, 2006.

[22] A. Mathur, J. Erlebacher: Size dependence of effective Young's modulus of nanoporous gold, *Applied Physics Letters*, vol. 90, 061910, 2007.

[23] D. Lee, X. Wei, X. Chen, M. Zhao, S. C. Jun, J. Hone, E. G. Herbert, W. C. Oliver, J. W. Kysar: Microfabrication and mechanical properties of nanoporous gold at the nanoscale, *Scripta Materialia*, vol. 56, pp. 437-440, 2007.

[24] E. Seker, M. L. Reed, and M. R. Begley: Review: Nanoporous Gold: Fabrication, Character-
      ization, and Applications, *Materials*, vol. 2, pp. 2188-2215, 2009

Chapter 4

Characterization of Interlayer Sliding Deformation for Individual Multi-Walled Carbon Nanotubes Using Electrostatically Actuated Nano Tensile Testing Device

4.1   Introduction

One-dimensional nanowires of carbon, silicon and compounds such as ZnO are attractive functional nano-materials for novel MEMS and NEMS devices because of specific physical properties attributable to their nanometer size and low structural dimensions. For example, silicon nanowires and single-walled carbon nanotubes are expected to be used as highly sensitive piezo-resistance elements for mechanical force sensors [1-4]. This is because one-dimensional semiconducting nanowires show a drastic change in the electronic structural features such as their band gap and effective mass under enormous mechanical strain, which can be used to determine the electron mobility [5, 6]. Quantitative evaluation of the mechanical and electrical properties of individual semiconducting nanowires under loading is very important for their application to high-sensitivity mechanical sensors.

MWCNTs are also representative nanowires that were discovered in the early 1990s [7, 8], and they have been recently used as ultralow-resistance interconnect materials for via structures in microelectronic devices [9, 10]. This technology is effective for highly reliable interconnect for the half-pitch 32 nm fabrication node and beyond because MWCNTs do not have problems associated with the electro-migration often observed in metallic interconnections. The lower electrical resistance and higher strength of MWCNTs are also excellently suitable for interconnect materials. However, via structures formed by MWCNTs have to withstand thermal stresses generated during the operation of microelectronic devices, which can lead to interlayer sliding deformation of MWCNTs resulting in changing electrical resistance. For reliable design of MWCNT interconnects, basic information is required on the mechanical and electrical characteristics of individual MWCNTs.

To characterize the mechanical and electrical properties of nanowires under uniaxial loading, several types of MEMS-based nano-scale tensile testing devices have been proposed in the

last decade [11-18]. Most include two functions at least: electrostatically or thermally driven actuators to produce a tensile force, and sensing elements for tensile displacement such as a capacitive displacement sensor or a gauge structure. The EANATs previously consisted of an electrostatically driven actuator and a cantilever beam used as a gauge to measure tensile displacement with an optical microscope. The displacement resolution was 0.29 nm with the assistance of image analysis. This device was successfully used for the investigation of stress-strain relations and the piezo-resistance effect of focused ion beam-deposited carbon nanowires with a diameter of around 100 nm, but it was still not suitable for direct observations of the deformation behavior of nanowires during tensile loading.

Other MEMS-based tensile testing devices have realized automatic measurement of tensile displacement by integrating a capacitive displacement sensor into the devices [16, 17], which is effective for observation of sample deformation during tensile testing. Most capacitive displacement sensors installed into devices have a parallel plate structure, the scale factor of which have small values of less than $1\ fF/\mathrm{nm}$ depending on the dimensions and the number of plates. These types of sensors have difficulty in measuring displacement directly at sub-nanometer resolution for their calibration. Even if SEM were to be used for the calibration, precise calibration of the displacement is not easy because of the uncertainties caused by drift and distortion of SEM images. Thus, a larger scale factor and a better structure of the capacitive displacement sensor are essential for accurate measurement of displacement as well as its precise calibration.

The present research focuses on clarifying the stress-strain relations, the interlayer sliding deformation behavior and the breaking mechanisms of individual MWCNTs using the newly designed EANAT. As a solution to the above-mentioned problems of MEMS-based tensile testing devices, this research has integrated a circular motion capacitive displacement sensor into an EANAT to realize precise calibration of the sensor. *In-situ* SEM nano-scale tensile testing using a nano-manipulation system was carried out for direct observations of the deformation behavior of samples during testing. This paper reports the design and functions of the newly developed EANAT, as well as details of the mechanical characteristics of individual MWCNTs.

4.2   DESIGN OF NANOTENSILE TESTING DEVICE

4.2.1   Experimental Methodology

The basic structure of the EANAT is the same as that of the previously proposed device [11, 12]; however a capacitive displacement sensor incorporated into the cantilever motion amplification system and thermally driven actuators used for stopping the movable frame are newly integrated into the device. **Fig. 4.1** shows a schematic of the new EANAT and its lumped mechanical model. An individual MWCNT is made to bridge the 5-μm-gap in the specimen area using the in-situ SEM nano-manipulation system. Thermally driven actuators are installed on the left- and right-sides of the movable frame in the specimen area to avoid vibrations of the frame when an individual MWCNT is implanted in the EANAT. An electrostatically driven comb actuator is separately arranged at an interval of 4 μm (= g_1) from the movable portion of the specimen area. Capacitive displacement sensors are set at an interval of 3 μm (= g_2) from the lower part of the electrostatically driven comb actuator employed for the tensile loading system. The movable portion of the specimen, the comb actuator and the displacement sensors are suspended by each supporting beam from fixed anchor parts.

In the lumped mechanical model, the force, F, generated by the comb actuator deflects the supporting beams of the comb actuator with a total stiffness of K_a at the beginning of device operation. This force is continually applied for elastic deformation of the sensor structures with a total stiffness of K_{ds}, the supporting beams of the specimen area with a total stiffness of K_s, and an individual MWCNT bridged at the specimen area. Therefore, F is expressed by the following equation [11],

$$F = K_a g_2 + (K_a + K_{ds})(g_1 - g_2) + (K_a + K_{ds} + K_s)\left[\delta_a^{before} - g_2\right] + P,$$

(4.1)

where δ_a^{before} is the displacement produced by the comb actuator before the failure of the sample, and P is the tensile force of the MWCNT. Because F before the failure of the MWCNT is equal to that after failure for the same applied voltage to the comb actuator, P is described as

$$P = (K_a + K_{ds} + K_s)(\delta_a^{after} - \delta_a^{before}) \qquad (4.2)$$

δ_a^{after} is the actuator displacement of the device without the sample after the failure. This equation indicates that the measurement resolution for the tensile force depends on the measurement resolution for the displacement and the values of K_a, K_{ds} and K_s.

The doubly-clamped beams used as the supporting beams at the actuator and the specimen areas show the nonlinearity of stiffness caused by tensile stress induced in the longitudinal direction of the beams under a large deformation. The stiffness of doubly-clamped beam having a trapezoidal cross-section with an upper width of a, a lower width of b, and a height of h, is given by

$$K = \left(\frac{\pi^4}{384}\right)\left\{\frac{Eh(a^3+a^2b+ab^2+b^3)}{l^3}\right\} + \left(\frac{\pi^4}{256}\right)\left\{\frac{Eh(a+b)}{l^3}\right\}\delta_a^2 ,$$

$$(4.3)$$

where E is the Young's modulus of the beam, l is the beam length, and δa is the actuator displacement. The stiffness calculated by Eq. (4.3) has agreed with that obtained from FEA, although it is omitted here.
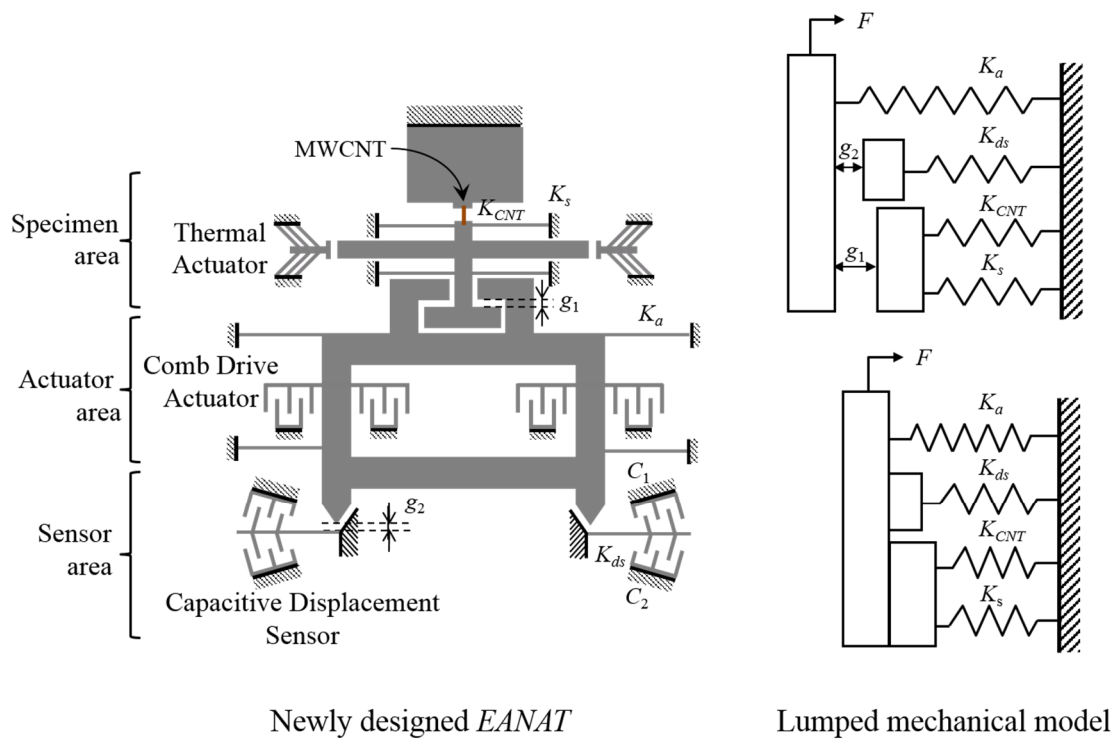
Newly designed *EANAT*   Lumped mechanical model

Fig. 4.1 Schematic of Newly designed EANAT

4.2.2   Comb Drive Actuator

The dimensions of the comb actuator were designed on the basis of the required force for the tensile test, considering the stiffness of each supporting beam and the test sample. The force, F_a, produced by the comb actuator at a displacement of δ_a from the initial position has been predicted in the design by the following equation,

$$F_a = N\varepsilon_0 h\left[\frac{1}{d_1} + \frac{w}{(d_2-\delta_a)^2}\right]V_a^2 \,, \tag{4.4}$$

where N is the number of combs, ε_0 is the dielectric constant in a vacuum, and h and w are the height and width of the comb, respectively. d_1 is the gap distance between contiguous combs, and d_2 is the distance from the tip of the comb to the opposite comb electrode in the initial state. V_a is the voltage applied to the actuator.

4.2.3 Capacitive Displacement Sensor on Cantilever Motion Amplification System

In order to realize a capacitive displacement sensor with a scale factor larger than $1\,\mathrm{fF/nm}$, we have newly developed differential capacitors with arc shaped combs incorporated into the cantilever motion amplification system [19] as shown in **Fig. 4.2**. The cantilever is bent by contact with the comb actuator part. The cantilever deflection, δ_i, at an arbitrary position between the bending point and the free end of the cantilever is given by

$$\delta_i = \delta_1 + l_i \sin\theta \, . \tag{4.5}$$

Here, δ_1 is the displacement at the bending point, θ is the angle of the deflected cantilever, and l_i is the length from the bending point to the arbitrary position on the cantilever. Since δ_1 is the actuator displacement after contact with the cantilever ($=\delta_a$-δ_2), the cantilever can mechanically amplify the actuator displacement. According to **Eq. (4.5)**, the mechanical amplification factor in the area of the capacitive displacement sensor ranges from 11.4 to 30.0, and the amplification factor at the free end of the cantilever is 32.5 in the present design. The amplification system carries the advantage of accurate calibration of the capacitive displacement sensor since the amplified displacement by the cantilever motion can be easily captured at the free end of the cantilever using an optical microscope with the assistance of image analysis **[11, 12]**. The arc shaped combs of the differential capacitors were designed on the assumption that the cantilever motion can be equivalent to circular motion around a virtual pivot on the cantilever if the angle of the cantilever deflection is small **[20]**. The radius of circular motion can be expressed as

$$r_1 = \delta_1 \times \frac{1}{\theta} = \frac{Fl_1^3}{3EI} \times \frac{2EI}{Fl_1^2} = \frac{2}{3}l_1 \, , \tag{4.6}$$

where F is the bending load, l_1 is the distance from the fixed end of the cantilever to the bending point, and I is the momentum of inertia. Therefore, the position of the virtual pivot is located at $l_1/3$ from the fixed end of the cantilever. Eq. (4.5) can then be rewritten as

$$\delta_i \cong \delta_1 + l_i \theta = \delta_1 + l_i \frac{3\delta_1}{2l_1} = \frac{2l_1 + 3l_i}{2l_1} \delta_1 . \qquad (4.7)$$

The capacitances of the differential capacitors have been estimated in the design of the EANAT. The capacitances at the upper and lower sides of the differential capacitors are represented by C_1 and C_2, and those at the initial state are defined as C_0, as shown in **Fig. 4.2**. Since C_1 decreases and C_2 increases with increasing δ_1, each capacitance during operation of the EANAT is the sum of C_0 and the respective capacitance changes, ΔC_1 and , ΔC_2, as shown in the following equations,

$$C_1 = C_0 + \Delta C_1 = C_0 + \Delta C_{\text{side}}^{\text{dec}} + \Delta C_{\text{tip}}^{\text{dec}} , \qquad (4.8)$$

and

$$C_2 = C_0 + \Delta C_2 = C_0 + \Delta C_{\text{side}}^{\text{inc}} + \Delta C_{\text{tip}}^{\text{inc}} \qquad (4.9)$$

$\Delta C_{\text{side}}^{\text{dec}}$ and $\Delta C_{\text{tip}}^{\text{dec}}$ are capacitance changes at the side- and tip-walls of the comb structure when the capacitance decreases, whereas $\Delta C_{\text{side}}^{\text{inc}}$ and $\Delta C_{\text{tip}}^{\text{inc}}$ are those when the capacitance increases, respectively. If the gap between the combs in the differential capacitors is equal to the width of the comb in the present design as shown in **Fig. 4.2**, C_0 is described by

$$C_0 = \sum_{k=1}^{n} \left\{ \frac{\varepsilon_0 h \left(r_k^{ins} + r_k^{outs} \right)(\beta_0 - \alpha_0)}{d} + 2 \frac{\varepsilon_0 h d}{D_k} \right\}$$

$$= \frac{\varepsilon_0 h n \left\{ 2l_2 - \frac{2}{3} l_1 + (3 - 4n)d \right\}(\beta_0 - \alpha_0)}{d} + \sum_{k=1}^{n} \frac{12\varepsilon_0 h d}{\{6l_2 - 2l_1 - 3d(8k-7)\}(\gamma_0 - \beta_0)} .$$

$$(4.10)$$

The first term of the equation is the total capacitance between the fixed and movable combs at their sidewalls, and the second is the capacitance at the tip walls of the combs. n is the number of arc shaped combs on the cantilever, and d is the gap between the combs (= width of the comb in the present design). r_k^{ins} and r_k^{outs} are the lengths along the cantilever from the virtual pivot to the inside- and outside-walls of the kth comb counted from the pivot, respectively. D_k is the initial distance from the tip-wall to the opposite wall of the kth movable comb.

ΔC_{side}^{dec} and ΔC_{side}^{inc} are geometrically given by

$$\Delta C_{side}^{dec} = \sum_{k=1}^{n} \left\{ \frac{-\varepsilon_0 h \delta_k^{ins}}{d} + \frac{-\varepsilon_0 h \delta_k^{outs}}{d} \right\}$$

$$= \sum_{k=1}^{n} \left\{ \frac{-\varepsilon_0 h \left(2l_1 + 3l_k^{ins}\right)}{2dl_1} \delta_1 - \frac{-\varepsilon_0 h \left(2l_1 + 3l_k^{outs}\right)}{2dl_1} \delta_1 \right\}$$

$$= -\left(\frac{\varepsilon_0 h n [3\{2l_2 - (4n-3)d\} + 4l_1]\delta_1}{2dl_1} \right), \tag{4.11}$$

and

$$\Delta C_{side}^{inc} = -\Delta C_{side}^{dec}, \tag{4.12}$$

as a function of the displacement, δ_1, at the bending point. Here, δ_k^{ins} and δ_k^{outs} are cantilever deflections at the inside- and outside-walls of the k_{th} movable comb, respectively. ΔC_{tip}^{dec} and ΔC_{tip}^{inc} are also expressed by

$$\Delta C_{tip}^{dec} = 2 \sum_{k=1}^{n} \varepsilon_0 h d \left(\frac{1}{D_k + r_k \theta} - \frac{1}{D_k} \right), \tag{4.13}$$

and

$$\Delta C_{tip}^{inc} = 2 \sum_{k=1}^{n} \varepsilon_0 h d \left(\frac{1}{D_k - r_k \theta} - \frac{1}{D_k} \right), \tag{4.14}$$

respectively. r_k is the length along the cantilever from the pivot to the center of the kth movable comb. ΔC_{tip}^{dec} and ΔC_{tip}^{inc} show nonlinear variations with increasing δ_1 as expressed above; however these variations is extremely small because the ratio of $\Delta C_{tip}^{dec\ or\ inc}$ to $\Delta C_{side}^{dec\ or\ inc}$ is less than 0.0006 % for a δ_1 of 1 µm. Consequently, we designed the differential capacitors with a scale factor of 1.26 fF/nm in this research.

A schematic diagram of the electrical circuit for the EANAT is depicted in **Fig. 4.3**. The charge amplifier circuit board manufactured by the authors has been connected to the common electrode of the differential capacitors with arc shaped combs. **Fig. 4.4** shows a schematic block diagram of the charge amplifier circuit. Modulation pulses of ± 5 V are applied at 1 MHz from the synchronous modulator to the fixed electrodes with the arc shaped comb structure opposite to the movable cantilevers. Manual adjustors for the offset voltage, the gain, and the phase are also installed in the amplifier circuit.
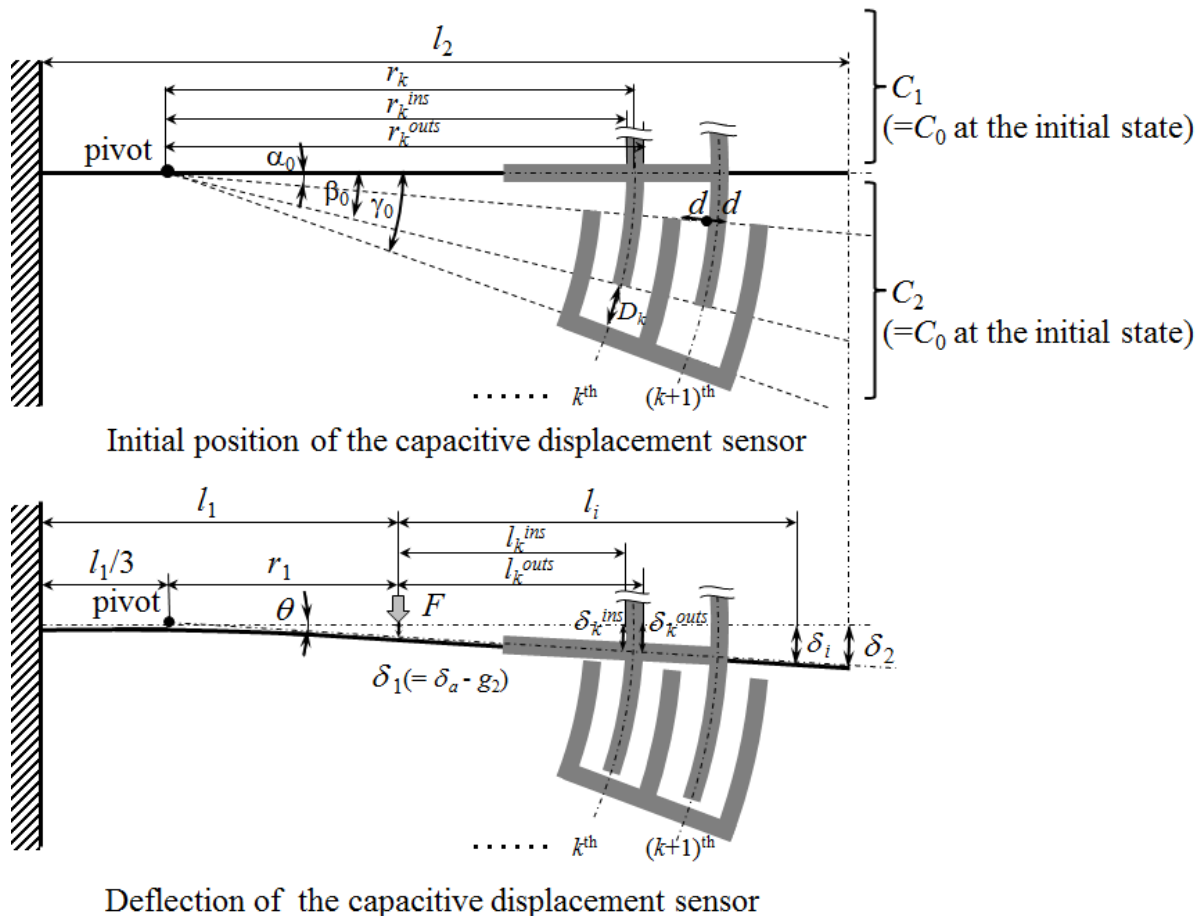

Fig. 2

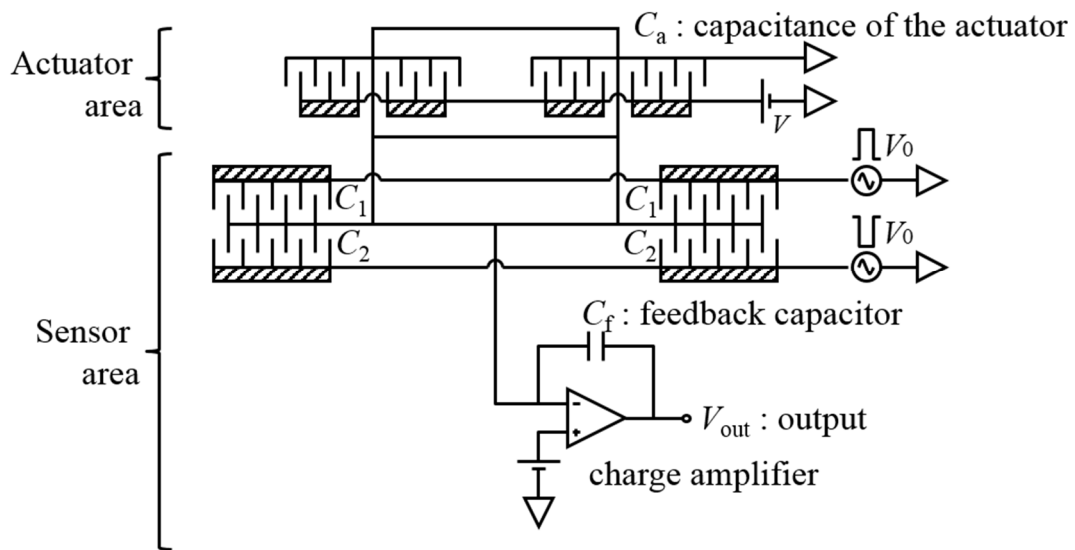**Fig. 4.2** Schematic diagram of the cantilever motion amplification system

Fig. 4.3 Schematic diagram of the electrical circuit for the EANAT
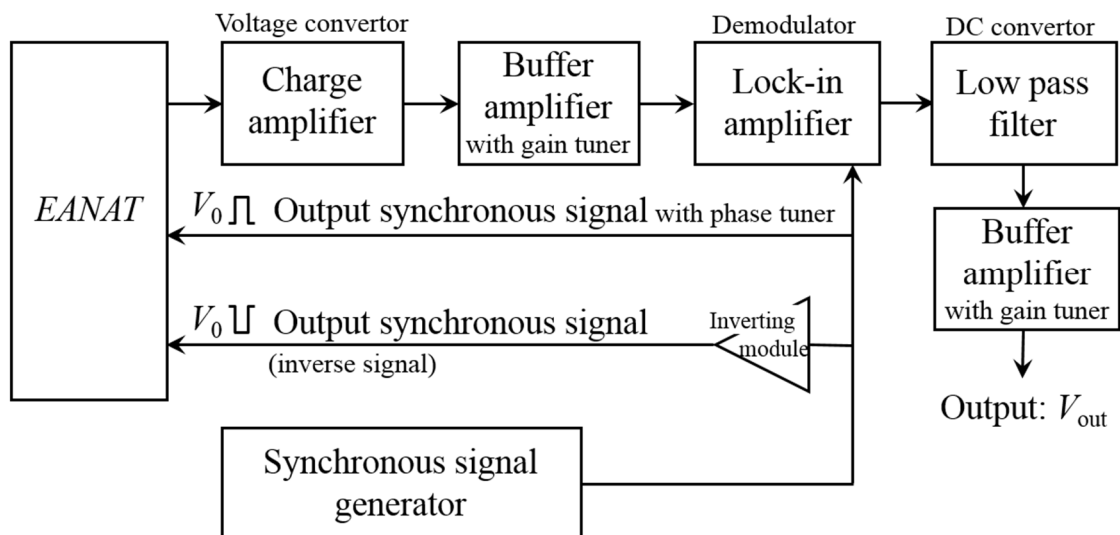
Fig. 4.4 schematic block diagram of the charge amplifier circuit.

4.2.4   Thermally Driven Actuator

The EANAT used in this work has a newly integrated thermally driven actuators used as a stopper for the movable frame of the specimen area when an individual MWCNT is implanted in the device. **Fig. 4.5** shows a schematic of the thermal actuator with the main shaft, the actuator beams and the supporting beams. The actuator beams are thermally expanded by Joule heating to apply a bias voltage between the fixed ends of the beams. The force generated by the actuator can be roughly estimated from the one-dimensional steady state heat conduction model. If the calorific value of the joule heat per unit length and the electrical resistance of the beam are described as

$$Q = \frac{i^2 R}{2L_1}, \quad R = \rho \frac{2L_1}{A},$$

(4.15)

respectively, the force is described as

$$F = \frac{MEA\alpha \sin \varphi}{4\rho\lambda} V^2$$

(4.16)

L_1 is the beam length, i is the electrical current, ρ is the resistivity, and A is the cross sectional area of the actuator beam. φ is the angle of the actuator beam from the perpendicular line to the main shaft, M is the number of actuator beams at one side, α is the thermal expansion coefficient of the beam, λ is the thermal conductivity of the beam, and V is the bias voltage applied to the actuator beams.

The stiffness of the thermal actuator is derived from simple beam theory as

$$k_{TA} = 2M \left(\frac{Ehw_1}{L_1} \sin^2 \varphi + \frac{Ehw_1{}^3}{L_1{}^3} \cos^2 \varphi \right) + 2m \frac{Ehw_2^3}{L_2{}^3},$$

(4.17)

where w_1 and w_2 are the widths of the actuator and supporting beams, respectively. m is the number of supporting beams on one side, and L_2 is the length of the supporting beam. The first term of the equation represents the stiffness of the actuator beams and the second term is for the supporting beams.
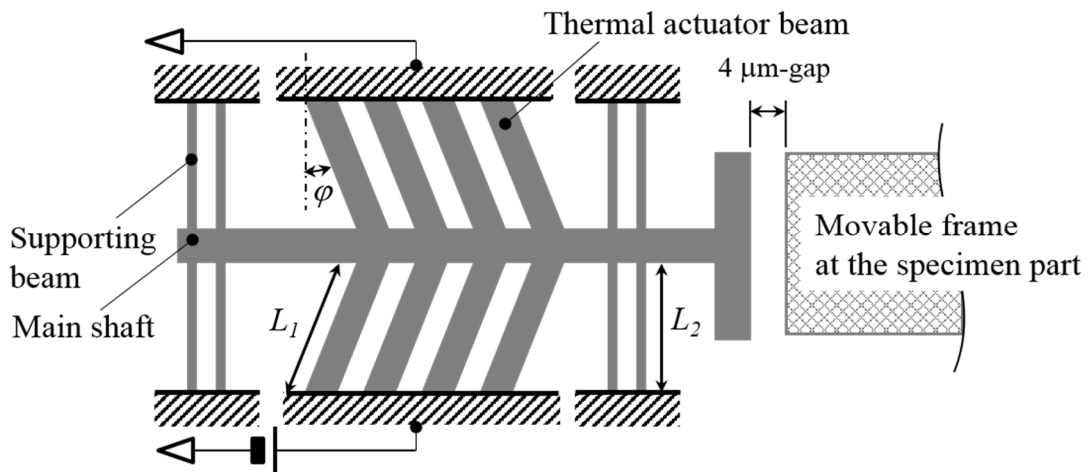

Fig. 4.5 Schematic of the thermal actuator

4.3 Fabrication

Fig. 4.6 (a) - (f) show the fabrication process of the EANAT. The starting substrate was a silicon (Si)-on-insulator wafer with a 35-μm-thick single crystal Si device layer and a 3-μm-thick buried oxide layer on a 400-μm-thick single crystal Si substrate, which was covered by a 400-nm-thick SiO_2 layer on the top and the backside (see **Fig. 4.6 (a)**). First, the areas of the electro-statically driven comb actuator, the thermal actuator and the capacitive displacement sensor were doped by a diffusion process using boron as the dopant (see **Fig. 4.6 (b)**). The device structure was patterned on the device layer side after Cr film deposition. The back-side patterning was also performed in a similar manner (see **Fig. 4.6 (d)**). The substrate layer was etched by deep-reactive ion etching (D-RIE), followed by etching of the device layer (see **Fig. 4.6 (e)**). A vaporized hydrofluoric solution removed the buried oxide layer to release the movable parts of the device (see **Fig. 4.6 (f)**). Gold electrodes were prepared in the device by a stencil mask technique. The device was finally set on the printed circuit board with wire bonding between the board and the device, and an MWCNT was fixed in the specimen area by the nano-manipulation system in SEM.

Two kinds of design dimensions for the EANAT were employed as Design *A* and *B* according to the above-mentioned design rules, and three devices (Device No. 1, No. 2 and No. 3) were fabricated. **Table 4.1** gives the design and measured values of the dimensions and stiffness for each beam used in the EANATs after fabrication. The cross-sectional geometries of the beams were measured at 10 different points for all of the EANAT from the top and the back sides to estimate the stiffness [12]. The lengths and diameters of MWCNTs tested in this work are also listed in the table. **Figs. 4.7 (a)-(e)** show SEM images of a typical fabricated EANAT. Each functional element was successfully fabricated on the device according to the design.

Si   SiO$_2$ P-doped Si   Cr
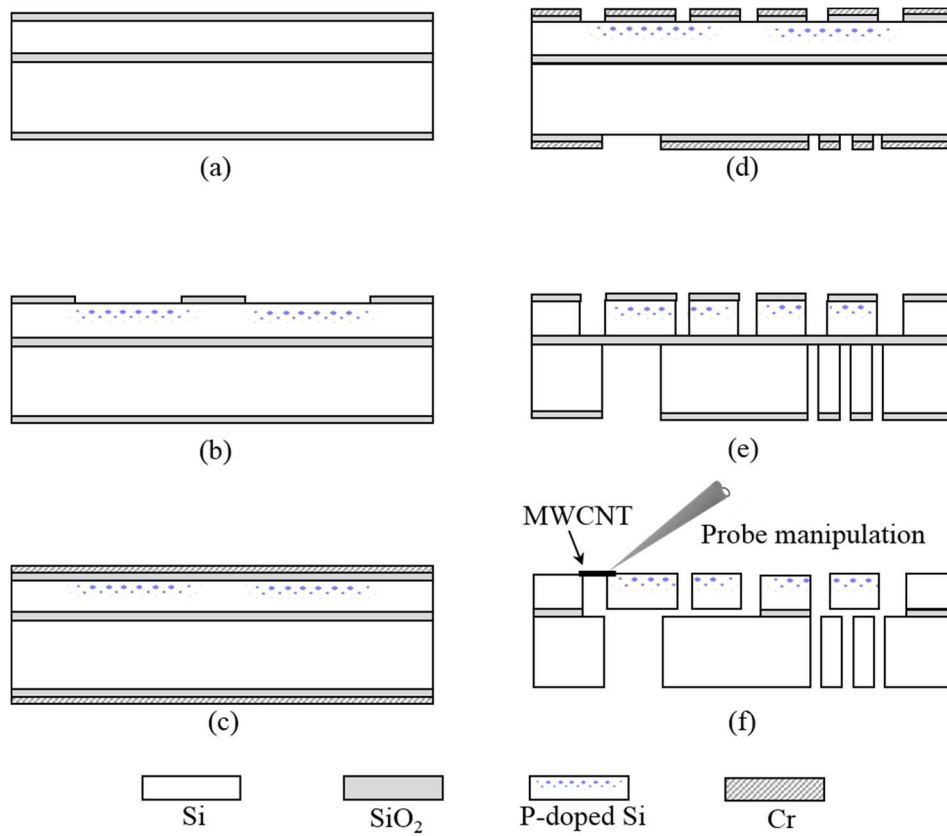
Fig. 4.6 Fabrication process of the EANAT.
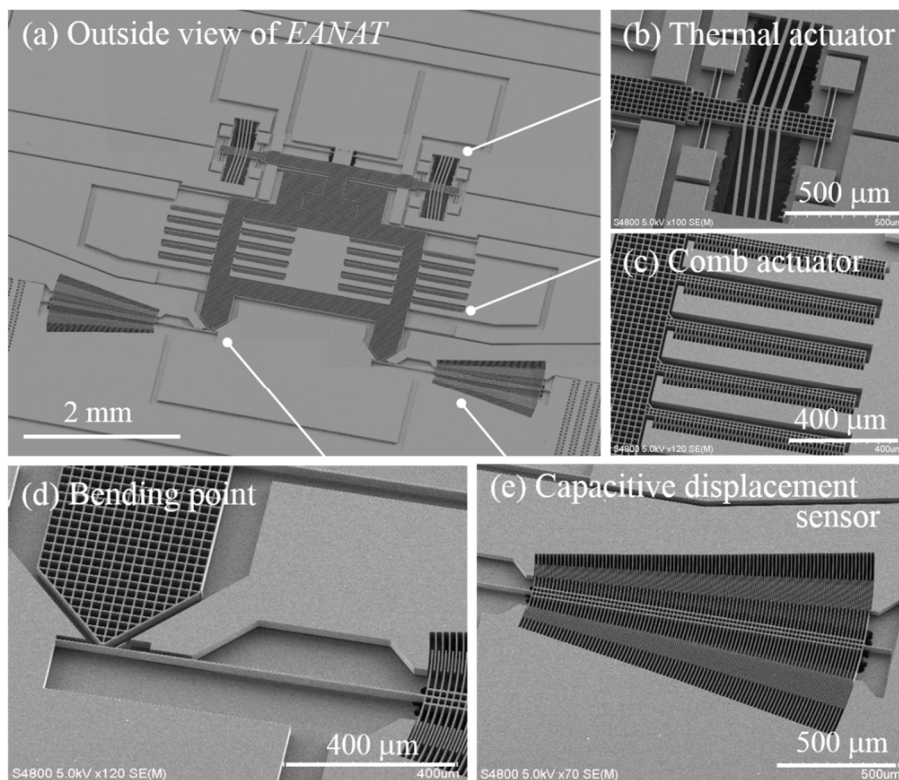
Fig. 4.7 SEM images of a typical fabricated EANAT.

Table 4.1 The dimensions and stiffness for each beam used in the EANATs.

| Beams	Dimensions (unit)	Device No. 1 Design A	Device No. 1 Measured (average)	Device No. 2 Design B	Device No. 2 Measured (average)	Device No. 3 Design B	Device No. 3 Measured (average)
	Height (μm)	35	35	35	35	35	35
Supporting Beams of Comb Drive Actuator	Length (μm)	700	719.2	700	696.1	700	683.2
	Upper Width (μm)	5	4.39	6	5.46	6	5.36
	Lower Width (μm)	—	3.99	—	4.97	—	4.99
	Number of Beams	4	↓	4	↓	4	↓
	Total Stiffness, K_a (N/m)	Eq. (3)	↓	Eq. (3)	↓	Eq. (3)	↓
Cantilever of Capacitive Displacement Sensor	Length, l_2 (μm)	110	113	110	110	110	108
	Upper Width (μm)	3	2.46	4	3.47	4	3.26
	Lower Width (μm)	—	1.82	—	2.81	—	2.76
	Number of Cantilevers	2	↓	2	↓	2	↓
	Total Stiffness, K_{ds} (N/m)	60	19.1	157.4	76.5	157.4	72.1
	Scale Factor (fF/nm)	1.26	—	1.26	—	1.26	—
Supporting Beams at Specimen Area	Length (μm)	700	719	700	696	700	683
	Upper Width (μm)	5	4.48	6	5.54	6	5.38
	Lower Width (μm)	—	4.02	—	5	—	4.95
	Number of Beams	4	↓	4	↓	4	↓
	Total Stiffness, K_s (N/m)	8.62	4.89	16.49	11.36	16.49	11.47
Actuator Beams of Thermal Actuator	Number of Beams at One Side	4	↓	4	↓	4	↓
	Length, L_1 (μm)	450	470.2	450	446.8	450	445.6
	Upper Width (μm)	15	13.35	15	14.42	15	14.44
	Angle, φ (degree)	5	5	5	5	5	5
	Total Stiffness (N/m)	13720.9	11279.6	13720.9	13185.9	13720.9	13242.6
	Specific Resistance (mΩ) [15]	3.40E-05	↓	3.40E-05	↓	3.40E-05	↓
Supporting Beams of Thermal Actuator	Number of Beams at One Side	4	↓	4	↓	4	↓
	Length, L_2 [μm]	150	161	150	149.8	150	149.6
	Upper width [μm]	5	3.43	5	4.44	5	4.43
	Total Stiffness (N/m)	1753	463.75	1753	1232.1	1753	1237.9
Sample	Length (μm) / Diameter (nm)	Sample No. 1	17.1 / 51.5	Sample No. 2	5.52 / 30	Sample No. 4	7.09 / 35.9
	Length (μm) / Diameter (nm)	—		Sample No. 3	5.1 / 31.3	Sample No. 5	5.91 / 32.3
	Length (μm) / Diameter (nm)	—		—		Sample No. 6	4.64 / 33.5

4.4 Device Characterization

4.4.1 Comb Drive Actuator

The travel distance of the comb drive actuator was easily and precisely measured as the cantilever position at the free end of the capacitive displacement sensor using a CCD camera system mounted on an optical microscope [11], because the cantilever motion amplified the actuator distance by as much as 32.5 times. **Fig. 4.8** shows variations in the displacement at the free end of the cantilever with an increase in the applied voltage to the actuator for Device No. 1 listed in **Table 4.1**. The displacement was not only measured in air but also in a SEM system (Hitachi S4800) in a vacuum of less than 1×10^{-3} Pa for *in-situ* SEM nano-tensile testing. For the calculation curves in **Fig. 4.8**, we took account of the nonlinearity of stiffness for K_a at the actuator area in **Eqs. (4.1)** and **(4.2)** owing to a larger deformation, and the linear stiffness for K_s at the specimen area because of a small displacement less than 1 $\mu\mathrm{m}$ in the present design.

There are no clear distinctions between the measured data in air and in a vacuum. The voltages when the cantilever displacement begins to increase in both environments are larger than the estimated voltage in the design. This is caused by fabrication variations which have led to widening the gap distance between the comb actuator and the displacement sensors. The increasing trend of displacement calculated using the deign dimensions of the supporting beams is totally different from the measured data, even if the nonlinearity of stiffness at the actuator area has been considered. The increasing rate of displacement calculated using the measured dimensions to the voltage is entirely consistent with the measured data, although the gap distances in the design have been employed in the calculation. If the calculation curve is simply shifted to the experimental curve as shown in the small graph attached to **Fig. 4.8**, the maximum error of the calculation from the experiment is 5.0 % at 50 V. Thus, the stiffness based on the measured dimensions of the beams has been estimated well in this research.
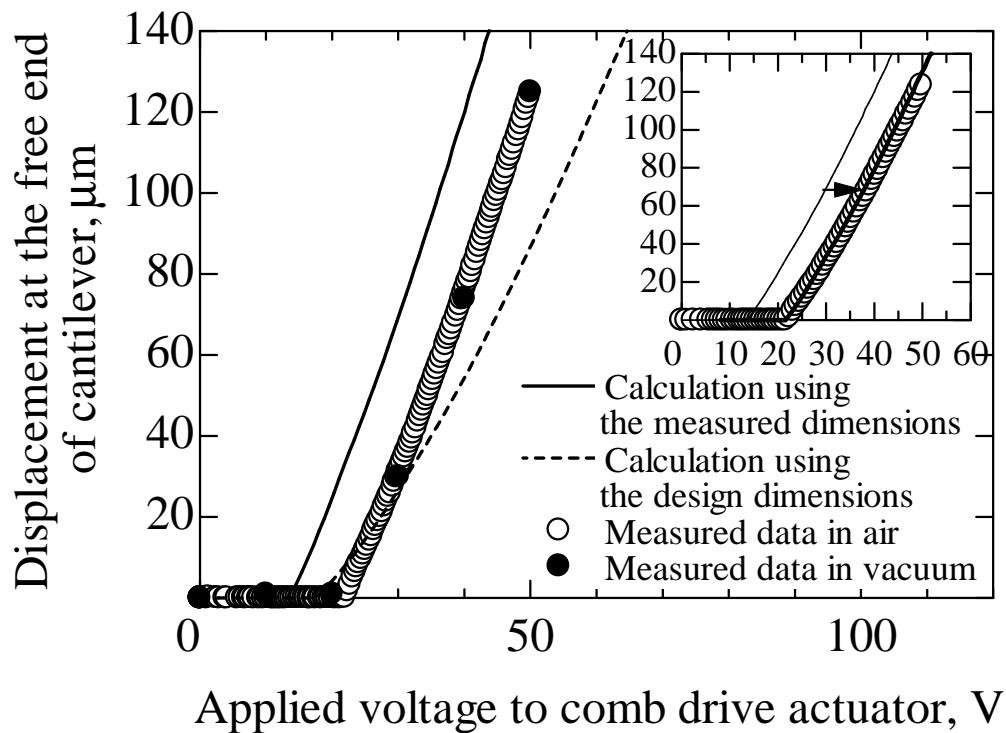
Fig. 4.8 Displacement of the cantilever edge of lever-motion amplification system as a function of the applied voltage in a tensile test.

4.4.2 Capacitive Displacement Sensor

The trajectory of the edge of the movable comb capacitor built in the cantilever at the left side of the EANAT was observed by the CCD camera system as shown in **Fig. 4.9**. The moving positions of the edge are consistent with the trajectory of the circular motion of the cantilever assuming the pivot as the circle origin, within an error of 0.16 μm; thus, the arc shaped comb can maintain the gap distance between the movable and fixed combs during operation.

Fig. 4.10 shows the typical sensitivity of the charge amplifier circuit connected to the capacitive displacement sensor, which was employed for Sample No. 6 on Device No. 1. The actuator displacement was converted from the deflection of the free end of the cantilever obtained from the CCD camera system that can capture images of about 5 frames for 1 second in the average. The bias voltage was applied to the actuator at 0.1 V for 0.1 second. These condi-

tions have led to the practical resolution in displacement of about 10 nm. The linear relation-ship between the output voltage and the actuator displacement is recognized as a function of $V_{out} = 2.139\, d_a$ in the figure. The output voltage increased smoothly and linearly from the initial stage of the increase of the actuator displacement. This result suggests that there is no remark-able difference in the gap distance at the contact point between both sides produced by fabri-cation variations. The output signals were recorded in the memory with a 14 bit-AD convertor working in the range of ± 5 V at a period of 10 msec. Consequently, the theoretical resolution of the displacement was 0.28 nm in this case.

The measurement resolution of the force was 27 nN, which was derived from the total stiffness of the supporting beams in the displacement range less than 1 μm. The practical meas-urement resolution of the force depends not only on the measurement resolution of the dis-placement and the stiffness, but also on the increment of the applied bias voltage to the comb actuator. In this research, the bias was applied from a DC supply unit to the actuators with a step rate of 0.1 V per 0.125 sec. Twelve or thirteen data ($\cong$ 0.125/0.01) points from the charge amplifier were approximately stored in memory for each voltage step. Thus, we employed a thirteen point moving average for a smoothing of experimental data [22].

The offset voltage, the gain and the phase tuners in the charge amplifier circuit were regu-lated in each experiment. Table 4.2 lists the measurement resolutions for the displacement and force after tuning the charge amplifier circuit for each sample.
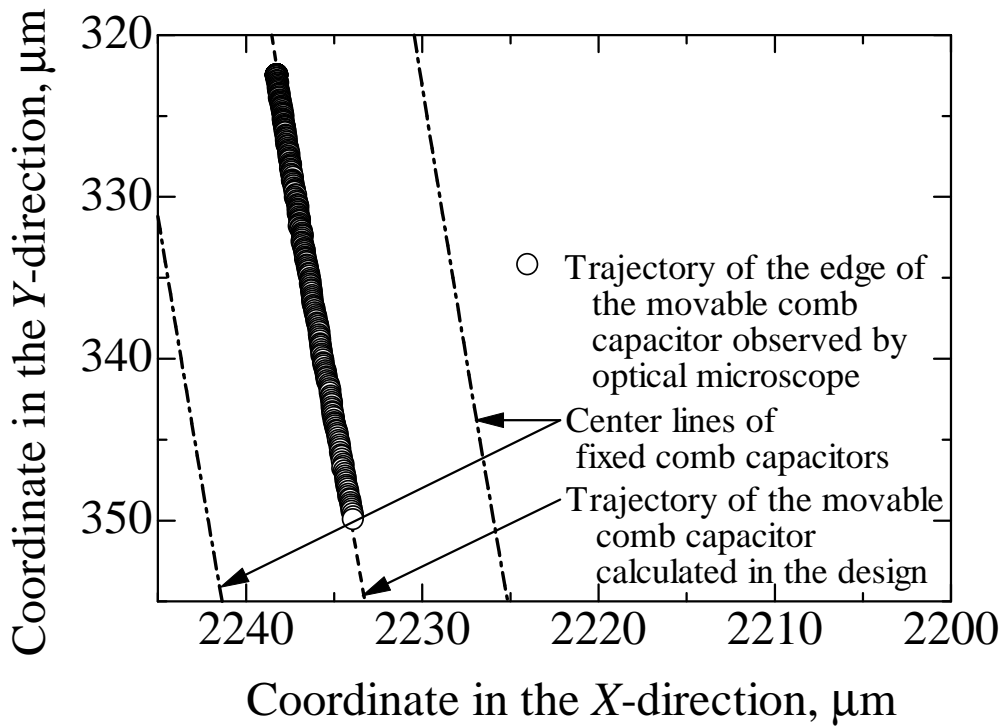
Fig. 4.9 Trajectory of the edge of the movable comb capacitor

$$V_{out} = 2.139\,\delta_a$$
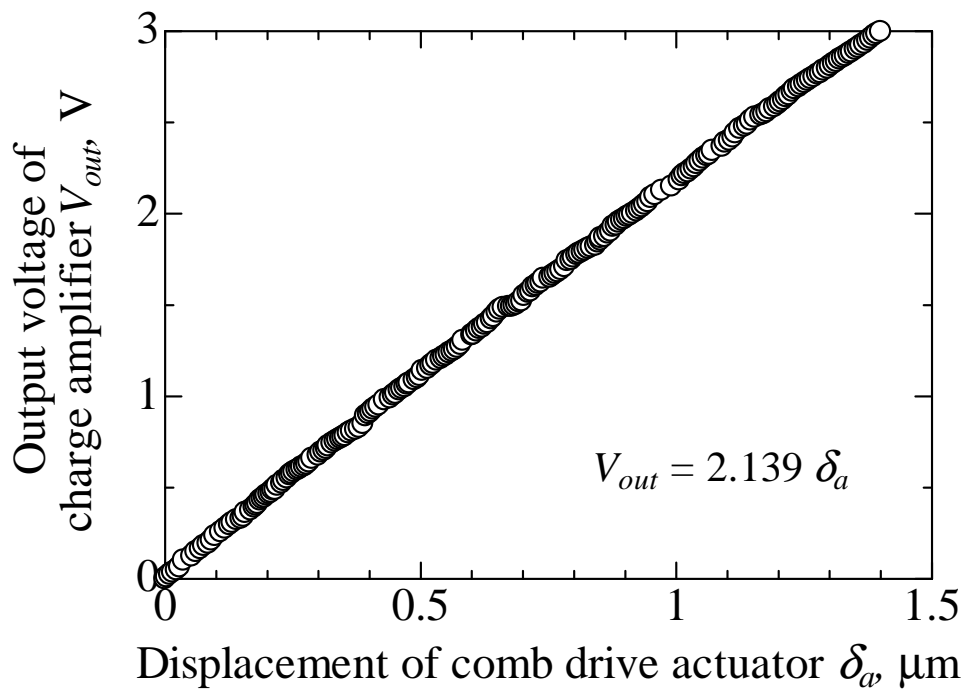
Fig. 4.10 Typical sensitivity of the charge amplifier circuit

Table 4.2 Measurement resolutions for the displacement and force.

Device	No. 1	No. 2		No. 3		
Sample	No. 1	No. 2	No. 3	No. 4	No. 5	No. 6
Sensitivity of Charge Amp. (V/μm)	0.66	1.58	1.55	1.22	1.86	2.14
Resolution of Displacement (nm)	0.93	0.39	0.39	0.50	0.33	0.28
Resolution of Load (nN)	42.0	38.2	38.7	47.5	31.1	27.0

4.4.3 Thermally Driven Actuator

Fig. **4.11** shows the relationship between the displacement of the thermally driven actuator observed by the optical microscope and its applied voltage. Optical microscopy images of the actuator before and after this operation are also shown in the figure. The solid line indicates the calculation data for Design *A* using the measured dimensions listed in **Table 4.1**. The measured displacement is saturated at 4.4 µm because of the contact between the actuator and the movable frame of the specimen area; thus, the actuator can play the role of a gripper to prevent the movable frame from vibrating. However, the measured displacement is approximately 44 % smaller than the calculation at each applied voltage: *i.e.,* the generated force in the experiment is 56 % of the force estimated in the design. The electric current necessary for heating would have been short in the actuator since the Au wire was bonded to a point the slightly remote from the actuator beam. Furthermore, heat generated at the actuator beam would be spread through the main shaft and the supporting beams **[17]**.
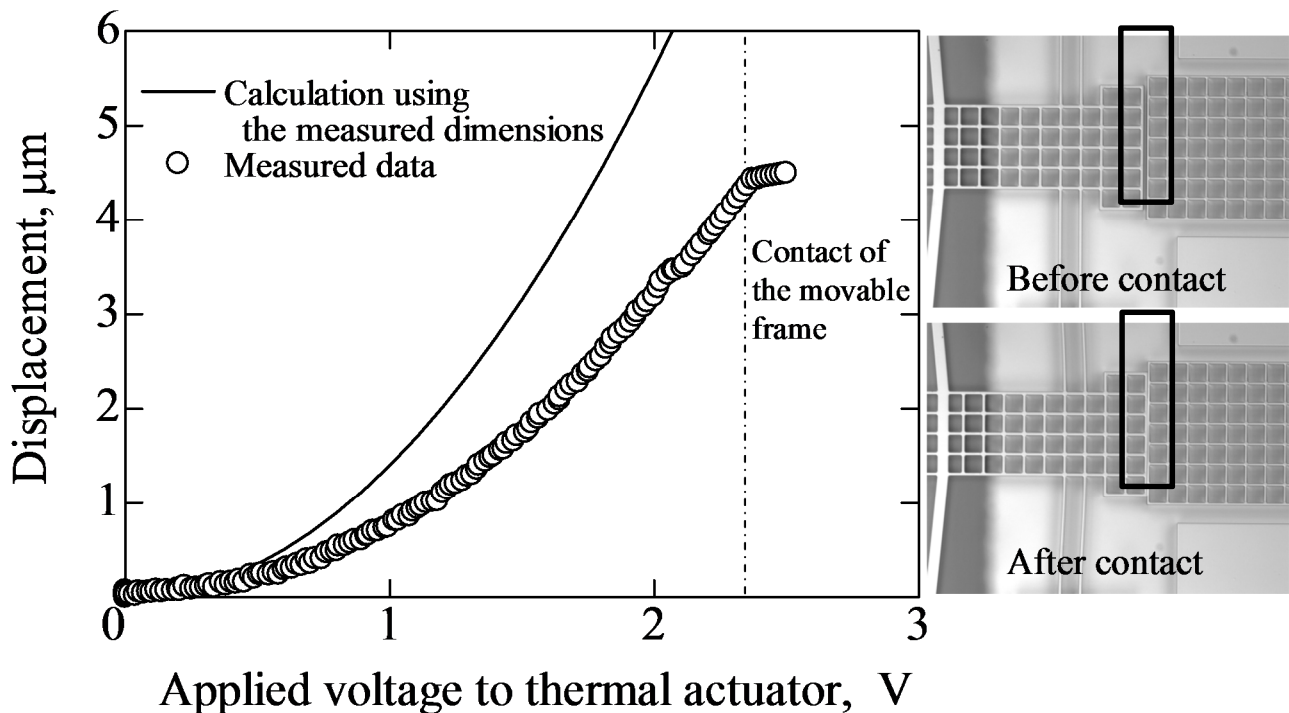

Fig. 4.11 Relationship between the displacements of the thermally driven actuator.

4.5 Nano-manipulation of Individual MWCNT

We have developed an *in-situ* SEM nano-manipulation system to pick up an individual MWCNT from a substrate and to fix it to an EANAT. The MWCNTs were synthesized by atmospheric-pressure chemical vapor deposition (APCVD) using acetylene and hydrogen gases under 200 Pa at 973 K. We employed titanium-binding-peptide ferritin molecules including 7 nm-diameter iron compound nanoparticles as catalysts for the MWCNTs growth; the synthesis details are reported in reference [23].

Fig. 4.12 shows photographs of the nano-manipulation system including two probe stages and one sample stage. Each of the probe stages has 3 degrees of freedom (DOF) and the sample stage has 2 DOF. A PZT actuator installed in each stage for fine displacement control allows for a positioning resolution of 0.1 nm, and the successive stepping motion of the PZT for long stroke movement uses a working space of the probe stages of 10 mm ($\pm$ 5 mm) in one direction. The charge amplifier circuit board for the differential capacitors of EANATs is also set on the system on the side of the sample stage in order to reduce electrical noise as much as possible.

The manipulation technique for an individual MWCNT has been established as shown in **Figs. 4.13 (a) - (d)**. First, we search for a straight MWCNT on the substrate, and the probe is then placed below the free end of the MWCNT. The MWCNT is fixed on the probe by electron beam induced contamination in the SEM with a higher emission current, i.e. the deposition of carbonaceous material over the sample surface (see **Figs. 4.13 (a)**). The vicinity of the fixed end of the MWCNT is cut by a focused electron beam with relatively low emission current and low accelerating voltage in high magnification mode (see **Figs. 4.13 (b)**). The MWCNT is moved to the test position previously marked by photolithography on the specimen area of the EANAT and is attached to the device by the electron beam induced carbon-based-contamination (see **Figs. 4.13 (c), (d)**). In this research, individual MWCNTs were completely covered in the diametrical direction by the contamination accumulated to a depth of 70 nm at least.

Any perceptible vibrations of the device during the probe manipulation were not observed in the SEM, and we have successfully implanted individual MWCNTs on the device once without breaking the samples and the supporting beams at the specimen area because of the thermal actuator. Any distinct distortions of the MWCNTs and the test position at the specimen area

were not also observed during the operation of the thermal actuator, although the temperature around the position was not measured. Since the test position is far from the thermal actuator at a distance of 1.01 mm in the present design, the temperature change at the position caused by the heat conduction would be small so as to be negligible.
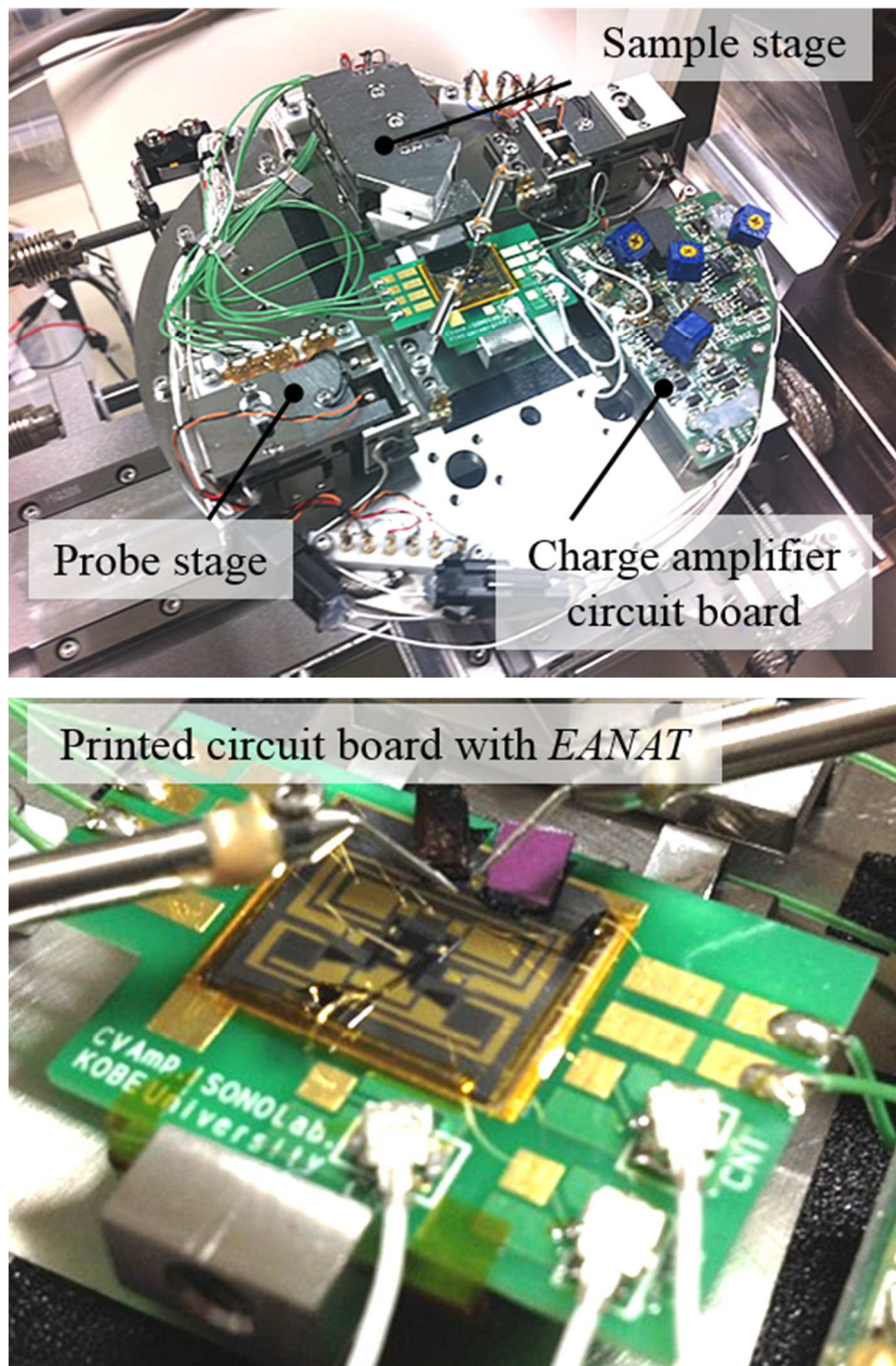
Fig. 4.12 Photographs of the nano-manipulation system.
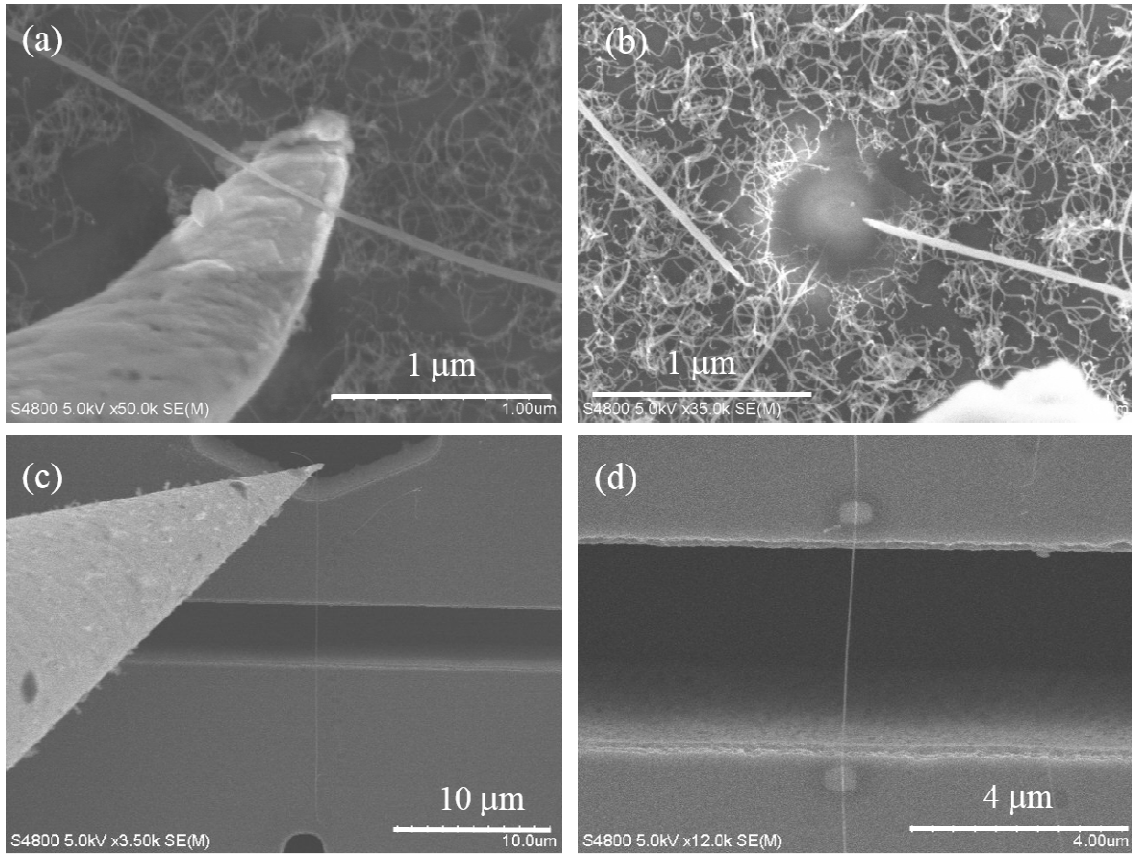
Fig. 4.13 SEM images of the specimen after the tensile test

4.6 Results

4.6.1 Tensile Testing Results

The EANATs were successfully used for tensile testing of six samples of the APCVD-synthesized individual MWCNTs listed in **Table 4.1**. Although the outer diameters were measured by the SEM, the mean-innermost diameter of MWCNTs was estimated at about 7 **nm** from transmission electron microscope (TEM) observations in the previous report **[23]**. This was consistent with the mean size of iron compound nanoparticles in ferritin molecules used as catalysts for the APCVD. This research, therefore, calculated the stress from the outer and the mean-innermost diameters as nominal dimensions.

Fig. 4.14 shows the typical relationship between the displacement converted from the output voltage of the capacitive displacement sensor and the voltage applied to the comb actuator for Sample No. 1. The sample had an average external diameter of 51.5 **nm**. The displacement increases above the applied voltage of 23 **V** because of the gaps between the comb actuator and the sensor cantilever. In the voltage range from 27.5 to 30.7 **V**, there is a distinct difference in the displacement before and after failure of the sample. This difference corresponds to the tensile force used only for deformation of the sample. The abrupt increase in the displacement at 30.7 **V** suggests initiation of fracture of the sample since the exact agreement of the displacements before and after the failure is observed again beyond 31 **V**. From the difference in the displacement, we can obtain the tensile load-displacement curve of the sample.

Fig. 4.15 shows tensile load-displacement curves for all MWCNTs tested in this work. Nonlinear deformation behaviors followed by a linear decrease in load with a gentle slope after breaking were observed for all samples. Although the tensile load increases with an increase in tensile displacement, regions of saturation and decrease exist in the curves before failure of the samples. **Fig. 4.16** shows the stress-strain curves estimated from the geometric properties of the samples. The stress drop regions after breaking are omitted for an easy understanding of the figure. Linear increases in stress are observed at the initial tensile deformation stage for all samples owing to their elastic deformation. In the case of Samples No. 3 and No. 4, the stress fluctuates slightly and reduces above $\varepsilon = 0.003$ with an increase in strain, respectively, and they linearly increase again with the same slope as the initial deformation regions. Sample No. 3 again shows a decrease in stress followed by a third linear increase. For the other samples,

saturated stresses are observed in the curves regardless of the increase in strain at higher stress levels. Some samples also show an increase in stress again with the similar ratio of stress to strain to that in the initial deformation. This trend in the load-displacement curve has already been reported by M-F. Yu *et al.* [24]. They clarified that individual MWCNTs showed interlayer sliding deformation behavior with stick-slip events between interlayers when the stress saturated or reduced during tensile loading.

From the slopes of the regions of linearly increasing of stress, Young's modulus was estimated to be in the range from 338 to 623 **GPa**; these results are close to or lower than the previously reported values **[24-26]**. The tensile strength of the MWCNTs also showed lower values of 2.22 to 3.25 **GPa**. The varied mechanical properties obtained are expected to be affected by various topological defects in the MWCNTs such as vacancies, Stone-Wales defects and adatoms, which are inevitably introduced during their synthesis **[27-29]**. **Table 4.3** summarizes the mechanical properties of the MWCNTs tested in this research. Fracture strains of the MWCNTs varied widely from 0.01 to 0.033 depending on the deformation behavior of the samples, and they were also lower than previously reported values **[24, 25]**.
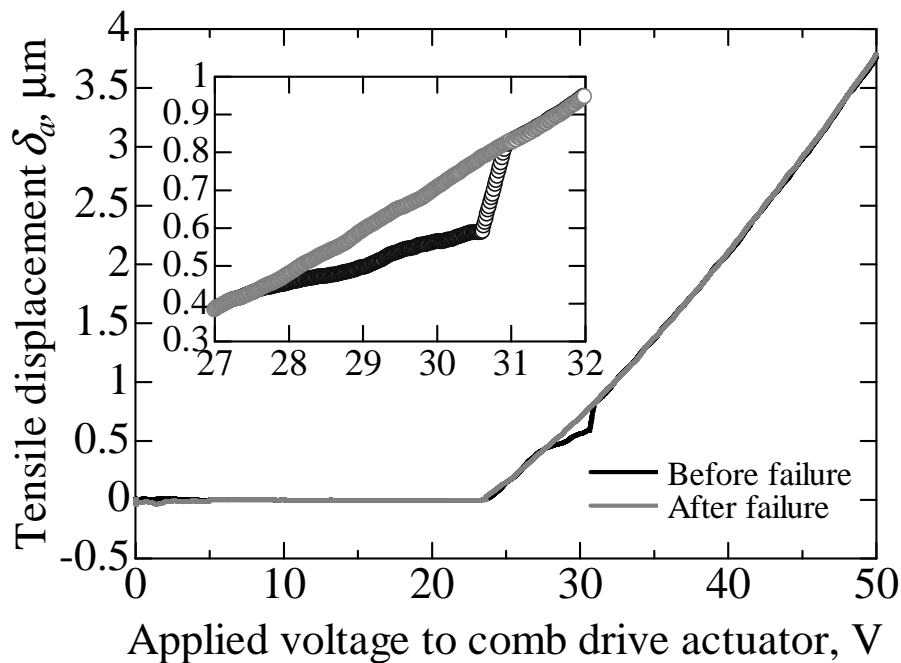
Fig. 4.14 Typical relationship between the displacements converted from the output voltage of the capacitive displacement sensor and the voltage

124
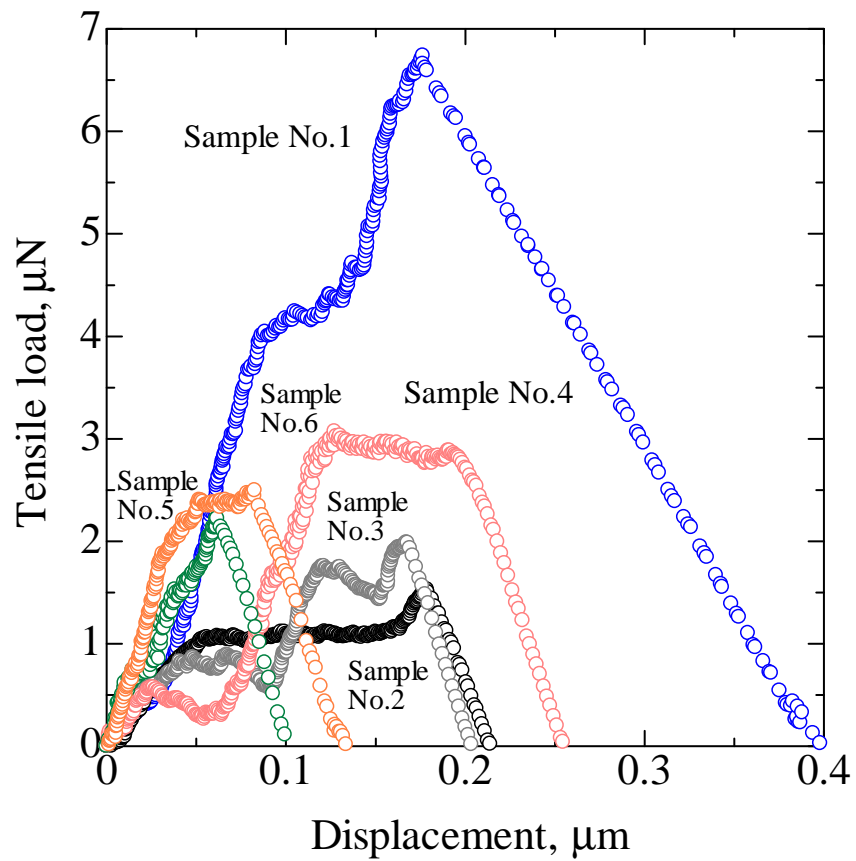
Fig. 4.15 Tensile load-displacement curves for all MWCNTs
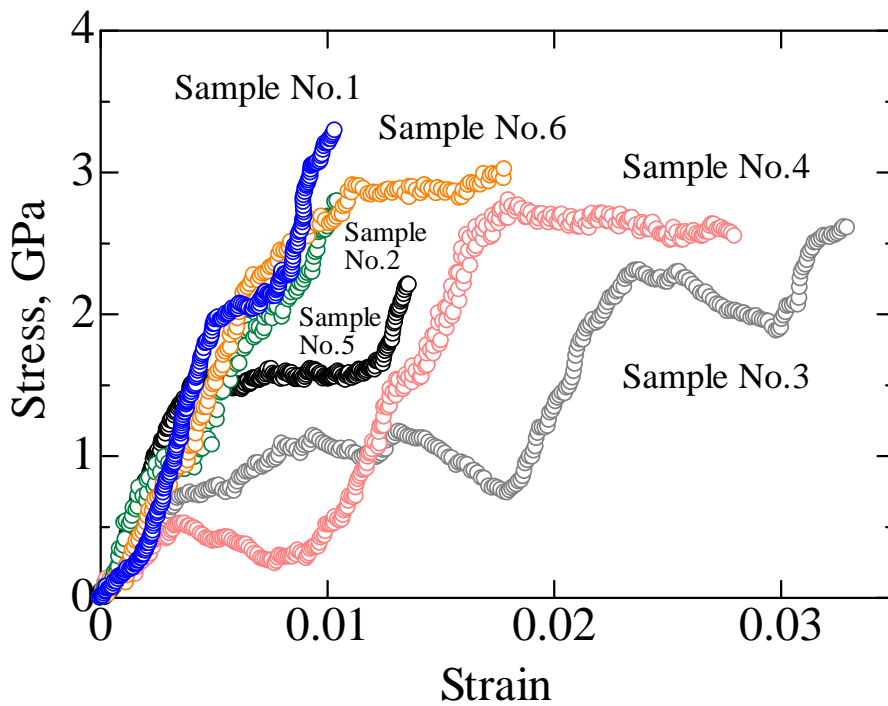
Fig. 4.16 Stress-strain curves estimated from the geometric properties of the samples.

Table 4.3 Mechanical properties of the MWCNTs.

Sample	No.1	No.2	No.3	No.4	No.5	No.6
Young's Modulus (GPa)						
the 1st increment	609	557	338	379	492	418
the 2nd increment	623	486	340	510	431	-
the 3rd increment	-	-	379	-	453	-
Tensile strength (GPa)	3.25	2.22	2.61	2.65	2.81	3.02
Fracture strain (%)	1.02	1.36	3.29	2.80	1.05	1.78
Elongation (μm)	0.174	0.179	0.168	0.198	0.062	0.083

4.6.2. Interlayer Sliding and Fracture Mechanisms of MWCNTs

In order to examine the fracture mechanism of the MWCNTs, all samples were subjected to observations after failure. SEM images of a typical fractured sample (Sample No. 4) are exhibited in **Figs. 4.17**. The sample broke in the vicinity of its fixed point in the specimen area. The inner layers seemed to be pulled up from the cylindrical MWCNT in the image in **Figs. 4.17 (a)**. The fractured edge of the outer layers shows a cleavage surface without remarkable plastic deformation as shown in **Figs. 4.17 (b)**, and the sample after failure maintained a straight external form. These observations suggest that the outer layers fractured in a brittle manner. The two-tier appearance of the inner-layer fractures are also shown in **Figs. 4.17 (a) and (c)**. These images indicate that at least three layers in the sample broke separately.

Considering the stress-strain curve for Sample No. 4, the stick-slip event between the layers could have occurred twice followed by the final fracture event. The number of times the stick-slip event occurred agrees with the number of fracture points in the SEM images. At the stick-slip events in the stress reduction regions of the curve, interlayer sliding like telescopic motion would have been produced after breaking one or more layers. After these events, the sample again deformed elastically due to hard sticking based on the interaction force between the sliding layers **[30]**, since a linear increase in stress was induced with the similar gradient to the initial stress increment in the curve. A small number of breaking layers would have led to a negligible change in the gradient of stress increment after the events.

The interaction force of dangling bonds on the fractured edge of the outer layer with the inner layer surface might also induce the hard sticking, which acted as an "edge effect" **[31]**. Repeating the stick-slip and hard sticking events after partial breaking of layers in the MWCNTs resulted in fracture.
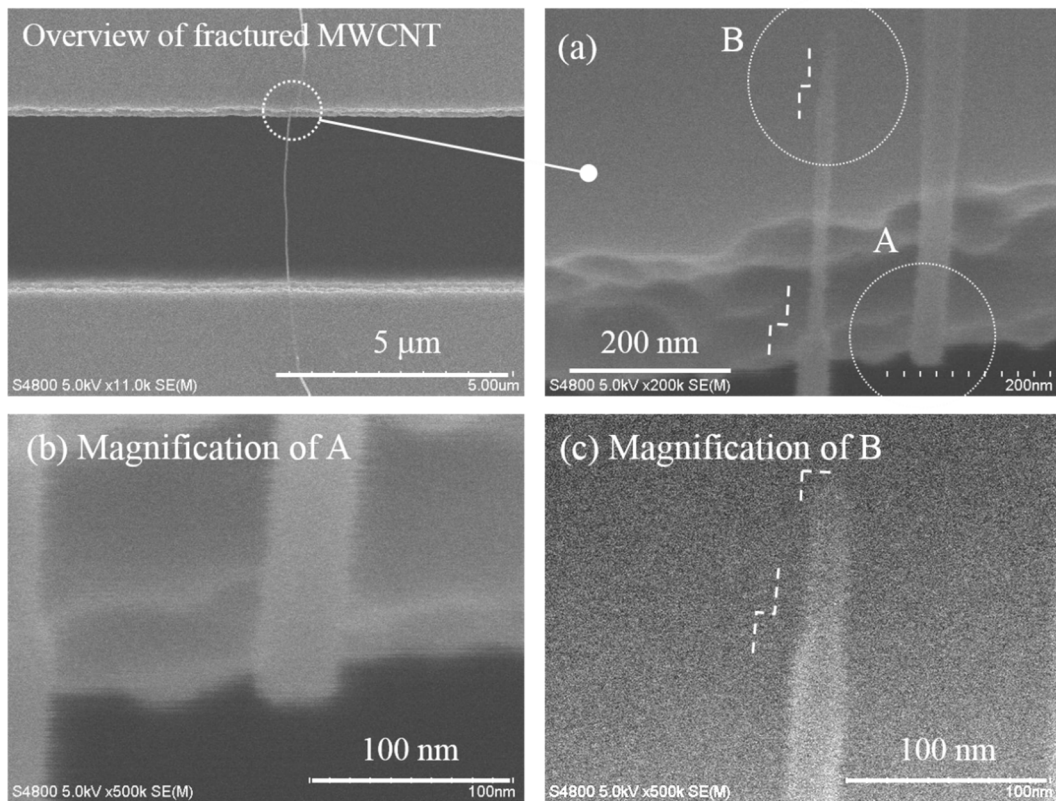
Fig. 4.17 SEM images of a typical fractured sample.

4.6.3. Interlayer Shear Strength

Interlayer sliding models of individual MWCNTs under tensile loading have been proposed for evaluating the interlayer shear strength, τ_s, from the interlayer force for an ultra-small stick-slip event. A. Kis *et al*. expressed the force expected during ultralow interlayer sliding between neighboring MWCNT layers to be the sum of the shear interlayer force and the cohesive force, based on cyclic loading tests [31]. M-F. Yu *et al*. also proposed a single-shot extraction model to determine the shear interlayer force experimentally from simple tensile tests on MWCNTs [30]. These models impose the test condition of displacement control loading with an ultra-low strain rate to estimate the interlayer force; however, in the current work, we performed tensile tests with a high loading rate without displacement control. Then, the present research focused only on obvious stick-slip events in the load-displacement curves, and roughly estimated the interlayer shear strength in the events on the basis of the single-shot extraction model.

Under the assumption that the saturated or reduced stress region in the load-displacement curves is caused by pulling out the inner layers from the outer layers of an individual MWCNT,

that is the stick-slip event, the tensile force during the event can be expressed as the sum of the shear interaction force between layers, F_s, and the interface force, F_i, which is given by

$$F = F_s + F_i = \pi D \tau_s L(x) + F_i \,.$$ (4.18)

D is the diameter of the inner layers shell and $L(x)$ is the sliding distance between the layers. The shear interaction force attributed to friction can be derived from the slope ($=\pi D \tau_s$) of the linear fit to the data points at the stick-slip event. The interface force consists of the capillary interface force and the cohesion force at the fractured edge of the outer layers to the inner layer surface; these two cannot be distinguished from each other experimentally [30].

We estimated the interlayer shear strength from the load-displacement curves for Samples No. 3 and No. 4 in **Fig. 4.18** because of their obvious stick-slip events. Compared with the sliding distance of Sample No. 4 observed in **Fig. 4.17**, the sliding distance at each stick-slip event in **Fig. 4.18** is about 65 % of the SEM observations. A stretch of the inner layers in the longitudinal direction might be produced by the impact of breaking; however, the positive cause of the difference is unclear until further observations of the fractured samples are carried out using a high-resolution TEM. For the present, the sliding distance was employed as the displacement at the stick-slip events in **Fig. 4.18** in the shear strength estimation.

The shear interaction forces at the first and second events for Sample No. 3 were estimated as 5.10 and 6.70 nN/μm, respectively, using geometrical properties of the fractured MWCNTs observed by SEM; thus, the average interlayer shear strength was 82.5 **MPa**. The average interlayer shear strength for Sample No. 4 was also 72.7 **MPa** estimated from the shear interaction force of 5.78 and 2.20 nN/μm. These values are significant larger than the shear strength of high-quality crystalline graphite of 0.25-0.75 **MPa** [32] and the previous reported values for MWCNTs [30, 31]. The larger shear strength might be caused by the hard sticking between layers. The hard sticking is possibly due to the edge effect of the outer layers that would also have led to larger shear strength. Therefore, the fracture of MWCNTs synthesized by APCVD was frequently accompanied by interlayer sliding deformation with hard sticking between layers, and such deformation behavior may cause an electrical resistance change of the MWCNTs. However, to clarify the quasi-static friction properties of single-shot extraction of individual MWCNTs in detail, cyclic loading tests need to be performed at an ultra-low rate of oscillation.
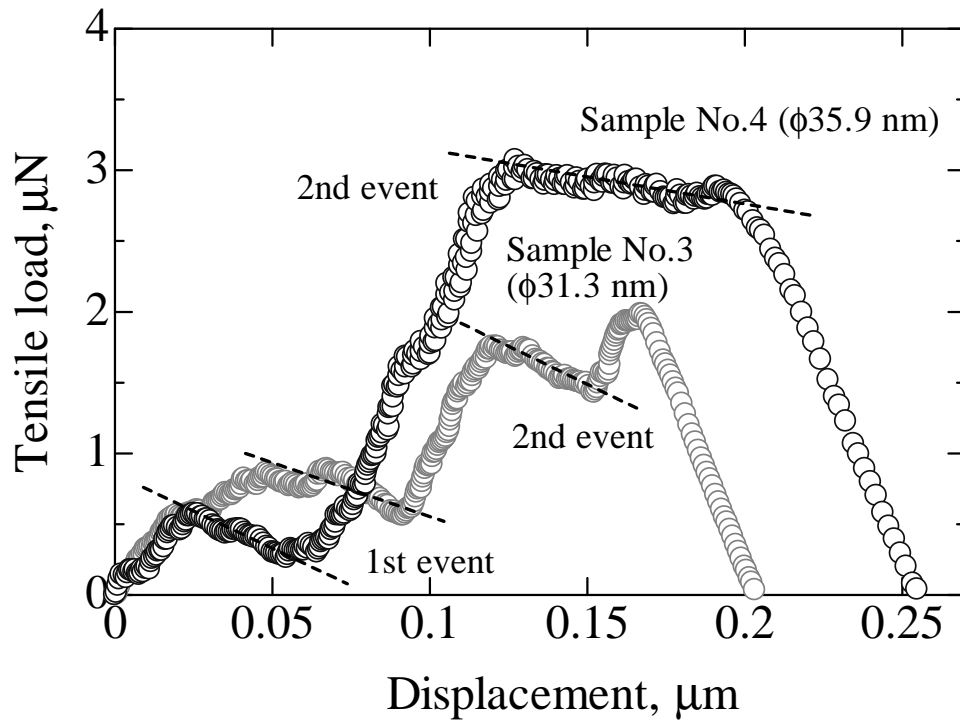
Fig. 4.18 Load-displacement curves of the interlayer shear strength.

4.7 Conclusions

Newly developed electrostatically actuated nano-tensile testing devices have successfully clarified the mechanical properties and fracture mechanisms of individual MWCNTs synthesized by APCVD. A capacitive displacement sensor with a scale factor of 1.26 **fF/nm** was designed using an arc shaped comb structure incorporated into a cantilever motion amplification system, which achieved a minimum resolution of 0.28 **nm**. We confirmed that the characteristics of the electrically and thermally driven actuators fabricated in the EANATs were according to their design. A tensile testing methodology for individual MWCNTs was established on the *in-situ* SEM nano-manipulation system. The Young's modulus of individual MWCNTs ranged from 338 to 623 **GPa**, and their tensile strength was in the range from 2.22 to 3.25 **GPa**. The fracture of individual MWCNTs was accompanied by repeated stick-slip and hard sticking events. SEM observations demonstrated that interlayer sliding, like telescopic motion, would have been produced after breaking one or more layers. The interlayer shear strength during the sliding was estimated to have large values of 82.5 and 72.7 **MPa** from obvious stick-slip events in the load-displacement curves, which might be caused by the hard sticking between layers.

We thus successfully obtained accurate load-displacement curves including stick-slip events for individual MWCNTs using the nano-tensile testing devices. However, for estimating the interlayer shear strength based on quasi-static friction of single-shot extraction of MWCNTs, further investigation of cyclic tensile loading testing with an ultra-low strain rate oscillation and small displacement need to be carried out.

References

[1]   Lugstein, M. Steinmair, A. Steiger, H. Kosina, and E. Bertagnolli: Anomalous Piezoresistance Effect in Ultra strained Silicon Nanowires, *Nanoletter*, vol. 10, issue 8, pp. 3204-3208, 2010.

[2]   Rongrui He, and Peidong Yang: Giant piezoresistance effect in silicon nanowires, *Nature Nanotech.*, vol. 1, pp. 42-46, 2006.

[3]   J. S. Milne, A. C. Rowe, S. Arscott, and Ch. Renner: Giant Piezoresistance Effects in Silicon Nanowires and Microwires, *Physical Review Letters*, vol. 105, issue 22, 226802 (4 pages), 2010.

[4]   T. Toriyama, and S. Sugiyama: Single crystal silicon piezoresistive nano-wire bridge, *Sensor and actuatos, A*, vol. 108, Issues 1-3, pp. 244–249, 2003.

[5]   K. Nakamura, Y. Isono, and T. Toriyama: First-Principles Study on Piezoresistance Effect in Silicon Nanowires, *Japan Journal of Applied Physics*, vol. 47, pp. 5132-5138, 2008.

[6]   K. Nakamura, Y. Isono, T. Toriyama, and S. Sugiyama: First-Principles Simulation on Orientation Dependence of Piezoresistance Properties in Silicon Nanowires, *Japan Journal of Applied Physics*, vol. 48, 06FG09-5 (5 pages), 2009.

[7]   S. Iijima: Helical microtubeles of graphitic carbon, *Nature*, vol. 354, pp. 56-58, 1991.

[8]   S. Iijima, and T. Ichihashi: Single-shell carbon nanotubes of 1-nm diameter, *Nature*, vol. 363, pp. 603-605, 1993.

[9]   F. Kreupl, A. P. Graham, G. S. Duesberg, W. Steinhögl, M. Liebau, E. Unger, and W. Hönlein: Carbon nanotubes in interconnect applications, *Microelectronic Engineering*, vol. 64, issues 1-4, pp. 399-408, 2002.

[10]   Jun Li, Qi Ye, A. Cassell, Hou Tee Ng, R. Stevens, J. Han, and M. Meyyappan: Bottom-up approach for carbon nanotube interconnects, *Applied Physics Letters*, vol. 82, no. 15, pp. 2491-2493, 2003.

[11]   M. Kiuchi, S. Matsui, and Y. Isono: Mechanical Characteristics of FIB Deposited Carbon Nanowires Using an Electrostatic Actuated Nano Tensile Testing Device, *Journal of Microelectromechanical System, IEEE/ASME*, vol. 16, no. 2, pp. 191-201, 2007.

[12]   M. Kiuchi, S. Matsui, and Y. Isono: The piezoresistance effect of FIB-deposited carbon nanowires under severe strain, *Journal of Micromechanics and.Microengineering*, vol. 18, 065011, 2008.

[13] Y. Zhang, C. Ru, Y. L. Zhang, L. Dong, and Y. Sun: Piezoresistivity Characterization of Synthetic Silicon Nanowires Using a MEMS Device, *Journal of Microelectromechanical Systems, IEEE/ASME*, vol. 20, no. 4, pp. 959-967, 2010.

[14] T. Tsuchiya, Y. Ura, K. Sugano, and O. Tabata: Electrostatic Tensile Testing Device With Nanonewton and Nanometer Resolution and Its Application to C60 Nanowire Testing, *Journal of Microelectromechanical System, IEEE/ASME*, vol. 21, No. 3, pp. 523-529, 2012.

[15] M. A. Haque, and M. T. A. Saif: In-situ tensile testing of nano-scale specimens in SEM and TEM, *Experimental Mechanics*, vol. 42, no. 1, pp. 123-128, 2002.

[16] D. Zhang, J.-M. Breguet, R. Clavel, V. Sivakov, S. Christiansen, and J. Michler: In Situ Electron Microscopy Mechanical Testing of Silicon Nanowires Using Electrostatically Actuated Tensile Stages, *Journal of Microelectromechanical System, IEEE/ASME*, vol. 19, no. 3, pp. 663-674, 2010.

[17] H. D. Espinosa, Y. Zhu, and N. Moldovan: Design and Operation of a MEMS-Based Material Testing System for Nanomechanical Characterization, *Journal of Microelectromechanical System, IEEE/ASME*, vol. 16, no. 5, pp. 1219-1231, 2007.

[18] T. Ishida, T. Sato, S. Nabeya, K. Kakushima, and H. Fujita: Highly Stable Spatio-Temporal Mechanical Characterization of Nanocontact between Sharp Tips Using Electrostatic Microactuator inside Transmission Electron Microscope, *Japan Journal of Applied Physics*, vol. 50, issue 7, pp. 077201-077201-5, 2011.

[19] H. Omori, M. Sadakata, I. Tsubokura, I. Hanasaki, and Y. Isono: Development of In-Situ SEM Nano manipulation & MEMS-Based Testing System with Ultra-Precision Displacement Sensors for Nanomechnics of MWCNTs, *IEEE, Tech. Digest of The 25th Inter. Conf. on MEMS, 2012 MEMS 2012*, pp. 412-415, 2012.

[20] X. M. Zhang, A. Q. Liu, C. Lu, and D. Y. Tang: A Real Pivot Structure for MEMS Tunable Lasers, *Journal of Microelectromechanical System*, IEEE/ASME, vol. 16, no. 2, pp. 269-278, 2007.

[21] S. W. Smith: Digital Signal Processing: A Practical Guide for Engineers and Scientists, ISBN: 9780750674447, Newnes, 2002.

[22] I. Hanasaki, T. Tanaka, Y. Isono, B. Zheng, Y. Uraoka, and I. Yamashita: Location and density control of carbon nanotubes synthesized using ferritin molecules, *Japan Journal of Applied Physics*, vol. 50, issue 7, pp. 075102-075102-6, 2011.

[23] M-F. Yu, O. Lourie, M. J. Dyer, K. Moloni, T. F. Kelly, and R. S. Ruoff: Strength and Breaking Mechanism of Multiwalled Carbon Nanotubes Under Tensile Load, *Science,* vol. 287, pp. 637-640, 2000.

[24] B. Peng, M. Locascio, P. Zapol, S. Li, S. L. Mielke, G. C. Schatz, and H. D. Espinosa: Measurements of near-ultimate strength for multiwalled carbon nanotubes and irradiation-induced crosslinking improvements, *Nature Nanotech.*, vol. 3, pp. 626-631, 2008.

[25] B. G. Demczyk, Y. M. Wang, J. Cumings, M. Hetman, W. Han, A. Zettl, and R. O. Ritchie: Direct mechanical measurement of the tensile strength and elastic modulus of multi-walled carbon nanotubes, *Materials Science and Engineering A,* vol. 334, pp. 173-178, 2002.

[26] L. G. Zhou and San-Qiang Shi: Formation Energy of Stone–Wales Defects in Carbon Nanotubes, *Applied Physics Letters*, vol. 83, no. 6, pp. 1222-1224, 2003.

[27] P. G. Collins: Defects and Disorder in Carbon Nanotubes, Oxford Handbook of Nanoscience and Technology, Volume: Materials (A. V. Narlikar, & Y. Y. Fu, Eds.), ISBN: 9780199533053, Oxford Univ. Press, 2010.

[28] G. Yamamoto, J. W. Suk, J. An, R. D. Piner, T. Hashida, T. Takagi, and R. S. Ruoff: The influence of nanoscale defects on the fracture of multi-walled carbon nanotubes under tensile loading, *Diamond & Related Materials*, vol. 19, pp. 748-751, 2010.

[29] M-F. Yu, B. I. Yakobson, and R. S. Ruoff: Controlled Sliding and Pullout of Nested Shells in Individual Multiwalled Carbon Nanotubes, *Journal of Physics Chemistry B*, vol. 104, no. 37, pp 8764-8767, 2000.

[30] A. Kis, K. Jensen, S. Aloni, W. Mickelson, and A. Zettl: Interlayer Forces and Ultralow Sliding Friction in Multiwalled Carbon Nanotubes, *Physical Review Letters*, vol. 97, no. 2, pp. 025501-022501-4, 2006.

[31] D. E. Soule, and C. W. Nezbeda: Direct Basal-Plane Shear in Single-Crystal Graphite, *Journal of Applied Physics*, vol. 39, issue 11, pp. 5122-5139, 1968.

Chapter 5

Conclusions

This thesis investigates the mechanical properties of representative MEMS materials on the micro- and nano-scale. The study results are published based on the tests from various materials and conditions by many researchers. In this study of mine, I have also tried to get the result from various materials and conditions, there were a few of difficulties: (a) The time limit to prepare for manufacturing a specimen, (b) difficulty of specimen development, (c) long time to complete the overall specimen process, (d) material restrictions due to semi-conductor process, i.e., silicon nitride film etched by vapor HF, (f) quality of process room, (g) self-development of micro- and nano-scale tensile testing system and so on. However, these results from chapter 2, 3, and 4 only can help someone design MEMS devices or IC circuits with these materials. The conclusion of each chapter is summarized as below.

In chapter 2, submicron PE-CVD SiNx films were characterized using the handmade uniaxial tensile tester built in AFM, in order to examine the influence of the gas flow ratio of NH_3 to SiH_4 on the elastic properties. The nano-indentation tests were also carried out for the estimation of Poisson's ratio for the SiNx films. The AFM tensile tester accurately measured effective elastic modulus of SiNx/SCS specimens, and we have succeeded in separating Young's modulus for only PE-CVD SiNx films. Young's modulus ranged from 99.5 to 149.3 **GPa**, which were lower than that of LP-CVD SiNx films due to low process temperature. Poisson's ratio of the films was also estimated as 0.13 to 0.37 from reduced modulus. The elastic properties of PE-CVD SiNx films were greatly influenced by the gas flow ratio of NH_3 to SiH_4, regardless with film thickness. Fracture strength of the SiNx/SCS specimens had in the range of 0.31 to 0.72 **GPa**, which is decreased with increasing film thickness. Auger spectroscopy was employed to reveal the film composition of the PE-CVD SiNx films. Nitrogen and silicon atoms were dominant, contained more than 90 % in the films. Young's modulus and Poisson's ratio of the SiNx films correlated with the atomic content ratio rather than the gas flow ratio. The SiNx films with an atomic content ratio being close to that in crystalline Si_3N_4 yielded higher elastic constants.

In chapter 3, we have developed the tensile testing device for Au thin films in the thickness regime of sub-100-**nm**. The size of the device is 10 **mm** by 10 **mm**, and it contains the specimen,

actuator, measurement part. EANAT act as electrostatic force between opposite comb drive area. The obtained mechanical properties showed marked differences from those of the bulk Au. The Young's modulus was 28 ± 3 **GPa**, which is less than 40 % of that of the bulk Au. The 0.2 % yield strength was 192 to 519 **MPa** with a trend of decrease with decreasing strain rates in the range from 5×10^{-5} s^{-1} to 5×10^{-2} s^{-1}. The tensile strength was in the range from 198 to 519 **MPa**, and the fracture strength was 191 to 587 **MPa**. The small Young's modulus was attributed to the existence of voids in the material characterized by the fabrication process of vapor deposition. The consequent lumpy surface also leads to the large variation of fracture strain because the initiation points of cracks are the notched parts which are stochastically determined by the fabrication process. Thus, the direct tensile tests of extremely thin Au films revealed the strong influence of material fabrication process on the mechanical properties.

In Chapter 4, newly developed electrostatically actuated nano- tensile testing devices have successfully clarified the mechanical properties and fracture mechanisms of individual MWCNTs synthesized by APCVD. A capacitive displacement sensor with a scale factor of 1.26 **fF/nm** was designed using an arc shaped comb structure incorporated into a cantilever motion amplification system, which achieved a minimum resolution of 0.28 **nm**. We confirmed that the characteristics of the electrically and thermally driven actuators fabricated in the EANATs were according to their design. A tensile testing methodology for individual MWCNTs was established on the *in-situ* SEM nano-manipulation system. The Young's modulus of individual MWCNTs ranged from 338 to 623 **GPa**, and their tensile strength was in the range from 2.22 to 3.25 **GPa**. The fracture of individual MWCNTs was accompanied by repeated stick-slip and hard sticking events. SEM observations demonstrated that interlayer sliding, like telescopic motion, would have been produced after breaking one or more layers. The interlayer shear strength during the sliding was estimated to have large values of 82.5 and 72.7 **MPa** from obvious stick-slip events in the load-displacement curves, which might be caused by the hard sticking between layers. We thus successfully obtained accurate load-displacement curves including stick-slip events for individual MWCNTs using the nano-tensile testing devices. However, for estimating the interlayer shear strength based on quasi-static friction of single-shot extraction of MWCNTs, further investigation of cyclic tensile loading testing with an ultra-low strain rate oscillation and small displacement need to be carried out.

Acknowledgements

This thesis is the final results for a decade at Kobe and Ritsumeikan University.
This work could never have been possible if it was not the helps of many people due to experimentally difficulties.

First, I am very grateful to Prof. Isono for allowing me to research at his laboratory, and for his devoted guidance and fully support during my studying in Japan. He always cheer me up whenever a tough moment comes up.

I would like to acknowledge Prof. Namazu for sharing with me this work, which evaluated the mechanical properties of the silicon nitride film in chapter 2 of this thesis.

I would like to acknowledge Prof. Hanasaki, Mr. Kawase, and Mr, Yamauchi for working with me this work, which evaluated the mechanical properties of gold thin film depending on the strain rate in chapter 3 of this thesis.

I also thank to Mr. Omori and Mr. Tsubokura for sharing with me this work, which resulted in the characterization of mechanical properties of MWCNTs in chapter 4 of this thesis.

Thanks to all laboratory members to help and support my works dedicatedly.

Finally, I dedicate this thesis to my family, especially my wife, MK Kang. Thank you for believing in me.